DIRECT COMPUTATION OF ASYMPTOTIC STATES FOR RATCHETING PREVENTION IN ELASTOPLASTICITY

Rafael Sant'Anna do Nascimento

Tese de Doutorado apresentada ao Programa de Pós-graduação em Engenharia Mecânica, COPPE, da Universidade Federal do Rio de Janeiro, como parte dos requisitos necessários à obtenção do título de Doutor em Engenharia Mecânica.

Orientador: Nestor Alberto Zouain Pereira

Rio de Janeiro
Dezembro de 2018

DIRECT COMPUTATION OF ASYMPTOTIC STATES FOR RATCHETING PREVENTION IN ELASTOPLASTICITY

Rafael Sant'Anna do Nascimento

TESE SUBMETIDA AO CORPO DOCENTE DO INSTITUTO ALBERTO LUIZ COIMBRA DE PÓS-GRADUAÇÃO E PESQUISA DE ENGENHARIA (COPPE) DA UNIVERSIDADE FEDERAL DO RIO DE JANEIRO COMO PARTE DOS REQUISITOS NECESSÁRIOS PARA A OBTENÇÃO DO GRAU DE DOUTOR EM CIÊNCIAS EM ENGENHARIA MECÂNICA.

Examinada por:

Prof. Nestor Alberto Zouain Pereira, D.Sc.

Prof. Edgar Nobuo Mamiya, D.Sc.

Prof. Fernando Pereira Duda, D.Sc.

Prof. José Luis Lopes da Silveira, D.Sc.

Prof. Heraldo Silva da Costa Mattos, D.Sc.

RIO DE JANEIRO, RJ – BRASIL
DEZEMBRO DE 2018

Nascimento, Rafael Sant'Anna do

Direct Computation of asymptotic states for ratcheting prevention in elastoplasticity/Rafael Sant'Anna do Nascimento. – Rio de Janeiro: UFRJ/COPPE, 2018.

X, 144 p. 29, 7cm.

Orientador: Nestor Alberto Zouain Pereira

Tese (doutorado) – UFRJ/COPPE/Programa de Engenharia Mecânica, 2018.

Referências Bibliográficas: p. 101 – 110.

1. Elastoplasticidade. 2. Ratcheting. 3. Métodos Diretos. I. Zouain Pereira, Nestor Alberto. II. Universidade Federal do Rio de Janeiro, COPPE, Programa de Engenharia Mecânica. III. Título.

To my wife, mother and father.
They support me in every
choices I make.

Acknowledgments

My mother Lucia and father Odilon fully dedicated themselves to raise my brother and me. For sure, filling their eyes with tears of pride was the main reason that motivated us to pursue our D.Sc. degrees.

Nathalia, my beloved wife, makes me a better person and I do not know how to live without her. Besides, she helped me to build the ratchet search algorithm. Yes, we are engineers and we bring that to our home.

Professor Nestor Zouain, my advisor, dedicated an unbelievable amount of time helping me. I would have to write a book to turn this into a fair acknowledgement. I am sincerely grateful. His constant example of dedication and his intelligence is worthy of admiration. It is an honor to work along with him during these years.

In the family side, my grandmother Marli started everything. Her willpower, good humor, and kindness are awesome. My older brother Leonardo is also a great father. He pushes me with his attitudes and I always followed his steps. Same schools, same university, similar courses and similar jobs. This is no coincidence.

In name of a long list of fellow friends and family, I thank to my grandmother Maria, Marta and Marcio Sant'Anna, Danielle Nascimento, Marcio Faria, Carlos Campos, André Pelliccione, Fernando Villas-Bôas, André Quelhas, Paulo Camargo, Thiago Handerson, Elisabeth Molina, Clóvis Ribeiro, Márcio Humberto, Wallace Carmona, Germano de Pádua, André Ribeiro, Antônio Flutt, Ana Paula, Patrícia and Tadeu Aquino, Vinícius Japiassú, Luiz André, Rafael Costa and Frederico Cruz.

Thanks to Professor Stenio, for being an amazing human that treated me like a son inside Petrobras. Thanks to Humberto Matrangolo, Filipe Leandro, Felipe Barin and Petrobras University for allowing me to develop this thesis while working at this amazing company. I do recognize the hard dedication of all my professors at Federal University of Rio de Janeiro, the institution that changed my life.

I also thank to my beloved godsons Guilherme and Marina. Finishing my list, I dedicate the last gratitude to my daughter Rafaela that is playing comfortably inside my wife's belly.

Resumo da Tese apresentada à COPPE/UFRJ como parte dos requisitos necessários para a obtenção do grau de Doutor em Ciências (D.Sc.)

DETERMINAÇÃO DIRETA DE ESTADOS ASSINTÓTICOS PARA PREVENÇÃO AO RATCHETING EM ELASTOPLASTICIDADE

Rafael Sant'Anna do Nascimento

Dezembro/2018

Orientador: Nestor Alberto Zouain Pereira

Programa: Engenharia Mecânica

Esta tese descreve três contribuições relacioadas a estruturas elastoplasticas sob carregamento cíclico. (i) O desenvolvimento de um método direto para determinação de resposta assintótica em elastoplasticidade ideal. Exemplos de validação demonstram que o método é rápido e preciso. O incremento de desempenho registrado foi de uma a duas ordens de grandeza superior à integração incremental. (ii) O desempenho permitiu o desenvolvimento de uma estratégia direta para identificação do limite de ratcheting estrutural. O procedimento é aplicável para cargas cíclicas e não possui limitação no número de cargas aplicadas. (iii) A extensão do método de resposta assintótica contemplando encruamento não linear que é requerido para modelagem do efeito Baushinger e ratcheting material. De conhecimento do autor, este é o primeiro método direto com tal capacidade. A comparação com análise incremental demonstra um aumento de desempenho de ao menos uma ordem de grandeza.

Abstract of Thesis presented to COPPE/UFRJ as a partial fulfillment of the requirements for the degree of Doctor of Science (D.Sc.)

DIRECT COMPUTATION OF ASYMPTOTIC STATES FOR RATCHETING PREVENTION IN ELASTOPLASTICITY

Rafael Sant'Anna do Nascimento

December/2018

Advisor: Nestor Alberto Zouain Pereira

Department: Mechanical Engineering

This thesis summarizes three contributions to improve design accounting elastoplasticity under cyclic loads. (i) The development of a direct method to compute the asymptotic steady-state solution in ideal elastoplasticity. Validation examples show that the method is fast and accurate. The performance ranges from one to two orders of magnitude higher than incremental analysis. (ii) The performance allowed the development of a direct strategy to identify the structural ratchet-limit. The procedure applies to periodical loads and has no limitations on the number of applied loads. (iii) The upgrade of the asymptotic solution method with nonlinear kinematic hardening, which is required to model the Baushinger effect and material ratcheting. To the author knowledge, this is the first direct method for steady-state solution with this capability. Comparison with step-by-step solutions shows a increase in performance of one order of magnitude, at least.

Contents

Chapter 1

Introduction

The use of metallic structures developing inelastic strains is a requirement of the modern society. Plastic strains are often desired to manufacture industrial equipment parts. Moreover, when put in service, structural components are prone to develop additional inelastic strains at stress concentration regions or at geometrical discontinuities. This happens even for structures designed to constrain its principal components into elastic regime.

Unfortunately, accidents caused by unaccounted plastic strains are present in industrial history. High impact cases are the Chernobyl nuclear accident, Columbus space ship and aircraft failures in a recent past (Varvani-Farahani and Nayebi, 2018). Instantaneous plastic collapse, incremental collapse and low-cycle fatigue are the main failure modes involving plasticity.

The prevention of plastic collapse has less uncertainty than the avoidance of other types of failures with plastic action caused by variable loads. The assurance that the maximum expected load is below a pre-defined level, based in limit analysis, is a sufficient condition to avoid the instantaneous plastic failure. On the other hand, avoiding low-cycle fatigue and ratcheting requires load and displacement controlled stress levels inside shakedown limits. The probability of success decreases due to: (i) the uncertainty of displacement induced stresses (thermal stresses, for instance) and (ii) the requirement of constraining stress levels below shakedown limits even at stress concentration regions.

The development of methods to evaluate protection against failures in elasto-plastic structures motivates the scientific community for decades. Efforts include the development of computational methods to deal with cyclical elastoplasticity, as well as, the identification of constitutive models capable of reproducing experimental results with higher precision.

This thesis summarizes three contributions to improve design accounting elastoplasticity under cyclic loads.

(i) The development of a direct method to compute the asymptotic steady-state solution in ideal elastoplasticity. Validation examples show that the method is fast and accurate. The performance ranges from one to two orders of magnitude higher than incremental analysis.

(ii) The performance allowed the development of a direct strategy to identify the structural ratchet-limit. The procedure applies to periodical loads and has no limitations on the number of applied loads.

(iii) The upgrade of the asymptotic solution method with nonlinear kinematic hardening, which is required to model the Baushinger effect and material ratcheting. To the author knowledge, this is the first direct method for steady-state solution with this capability. Comparison with step-by-step solutions shows a increase in performance of one order of magnitude, at least.

The text has seven chapters. Following introduction chapter, a literature review appears in chapter 2. The review comprises the three topics listed above. Chapter 3 reviews the theoretical background related to the research. Chapter 4 describes the direct method to compute asymptotic solution. Chapter 5 presents the ratchet-limit algorithm, object of the qualified proposal for the thesis. Chapter 6 includes the upgrade of the direct method to nonlinear kinematic hardening. In chapter 7 the conclusions of the thesis are summarized.

The procedure outlined in chapter 5, designed and implemented by the author under Prof. Zouain orientation, accomplishes the objective of the qualified thesis proposal. However, the procedure is a layer above the direct method developed by the Professor, with author contributions.Thus, aiming self-containment, chapter 4 details the direct method to compute the asymptotic response, its implementation and validation. Moreover, chapter 6 describes an upgrade of the asymptotic response method (chapter 4), again developed by Professor Zouain, that also accounted with contributions by the author.

Chapters 4, 5 and 6 follows Zouain and SantAnna (2017), SantAnna and Zouain (2018) and Zouain and SantAnna (2018), respectively.

Chapter 2

Literature Review

This chapter reviews the literature related to the research project development. It includes (i) the asymptotic steady-state response of elastic-ideally plastic solids under cyclic loads, (ii) the structural ratchet limit identification and (iii) the computation of the asymptotic solution with nonlinear kinematic hardening.

2.1 On the asymptotic response

The literature review of the present section follows Zouain and SantAnna (2017).

Experimental observation shows that many structures submitted to cyclic loadings reach a stabilized response. Such stabilization is theoretically proven for some models of inelastic behavior, like the generalized standard materials (GSM), (Polizzotto, 2003). It was so recognized (Frederick and Armstrong, 1966; Polizzotto, 1994a,b) that the asymptotic stresses in such structures variate cyclically and with the same period as the applied loading.

Here, "steady state" refers to a solution where the stresses and strain rates are periodical. It means the long term solution, after the stabilization phase, which is denoted by "transient". This definition is different from the classical thermodynamic steady state, in which the state variables become time independent. Morover, it is remarked that the elastoplastic problem treated here is time dependent, but rate independent. That means that the sequence of loading affect results, whereas the loading rate does not.

Frederick and Armstrong (1966) endorse the direct determination of the steady-state solution to avoid history computation, if the long-term solution is of interest. They proved a theorem assuring convergence to an unique solution of two identical structures submitted to the same variable loads, but with different initial stress states. The main hypothesis are: small strains and stable material (Drucker postulate holds true). Thus, a remarkable characteristic of the stabilized solution is

the independence of initial conditions (Frederick and Armstrong, 1966; Polizzotto, 2003).

This thesis focuses on direct methods for computing the asymptotic response under cyclic loads (Ponter and Chen, 2001; Spiliopoulos and Panagiotou, 2012; Tereshin and Cherniavsky, 2015), as opposed to incremental integration procedures that reproduce the complete time solution, including the transient deformation process. Direct methods aim to obtain the desired steady state in much less processing time than step-by-step analysis (Rohart et al., 2015).

Gokhfeld and Charniavsky (1980) addressed the determination of the steady state, formulated as a linear programming problem, with simplifications based on the concept of fictitious yield surface. The same theoretical unified approach is adopted in Tereshin and Cherniavsky (2015), where a nonlinear optimization problem is solved for a small finite element mesh. Ponter and Chen (2001) presented a generalization of the upper bound theorem of shakedown in the form of a minimum theorem for a general cyclic history. Then, they applied this theory in a method for identifying the ratchet limit for a class of loading histories. Several improvements and extensions of that contribution were presented by these authors, making use of the Linear Matching Method as main computational approach; see (Lytwyn et al., 2015a,b) and references therein.

Maitournam et al. (2002) proposed the Direct Cyclic Method for inelastic response, based on decomposition in Fourier series, already implemented in a commercial code. In the case of ratcheting, the method does not converge.

Polizzotto (2003) proposed variational formulations for the steady state response in the context of generalized standard materials. Solution methods emerging from those theoretical achievements were then specialized to the determination of the ratchet limit.

Spiliopoulos and Panagiotou (2012) (see also Panagiotou and Spiliopoulos (2016)) proposed the Residual Stress Decomposition Method, based on decomposing the residual stress in Fourier series. The stress rates are found satisfying equilibrium and compatibility. Then, plastic straining is accounted for by adding the elastic and residual stress and estimating the plastic strain rate from the stress in excess of the yield surface.

Peigney and Stolz (2003) presented a control approach to cyclic analysis. The asymptotic cycle is found minimizing a functional of arbitrary fields of plastic strains and internal variables. This functional is always positive and zero for any minimizer. The approach is applicable to other nonlinearities than plasticity.

Chapter 4 of this thesis describes an algorithm to compute the stabilized solution, based on a computational formulation of the set of conditions characterizing the asymptotic response. The method was proposed and implemented by Professor

Zouain with author contributions (Zouain and SantAnna, 2017). This computational formulation consists of the identification of a set of equations for the problem, comprising a reduced number of primary unknowns and equations, and obtained mainly by the formal use of the linear map associating a residual stress field to any plastic strain field. The algorithm proceeds by successive substitutions on this formulation. It strongly relies on a special trial and projection operation for the local update of the plastic strain increments. The complete procedure adopts the backward Euler approximation of the plastic flow law and standard finite element assumptions. That is, it does not introduce any additional approximation compared to the traditional integration of elastoplastic equations.

2.2 On the identification of the ratchet limit

Considering cyclic loads, the asymptotic response is an elastic cycle for loadings below the shakedown limit (Lubliner, 2008; Zouain, 2018). Plastic collapse (impending unbounded deformation) occurs for a loading program reaching a limit load at some instant. Otherwise, the asymptotic plastic strain rates are nonzero and periodic, with the same period. The accumulated plastic strains either: (i) exhibit zero net increment per cycle, in the case named alternating plasticity (ii) undergo constant per-cycle increment in the case of a process of incremental collapse, leading to gross distortion.

In summary, elastoplastic steady-state responses to cyclic loadings necessarily belong to one of the following classes: purely elastic cycling, alternating plasticity, incremental collapse or plastic collapse.

Failure analysis of structures and machines submitted to variable loadings often requires the identification of the expected behavior in terms of the above classification. Furthermore, the quantification of plastic deformation and residual stresses is also of interest, for instance, when a subsequent analysis assess safety against fatigue.

Melan (1938) and Koiter (1956) theorems define the necessary and sufficient conditions for shakedown (SD). Any arbitrary load path contained inside SD domain is safe against alternating plasticity, ratcheting or plastic collapse (König, 1987; Zouain, 2018).

During a SD analysis, a traditional stress classification becomes convenient. Load controlled stresses are defined as primary, due to its capability of instantaneous collapse development. In turn, displacement controlled stresses are classified as secondary, because such type of stresses are incapable of developing instantaneous collapse.

For instance, the shakedown boundary solution for the Bree problem with a

rectangular reference loading program (OABC) appears in figure 2.1 (Bradford, 2017). According to SD theorems, arbitrary cyclic loading programs shake down to elastic response if they are encapsulated by an μ amplified rectangle (OA'B'C'), where μ is the shakedown factor.

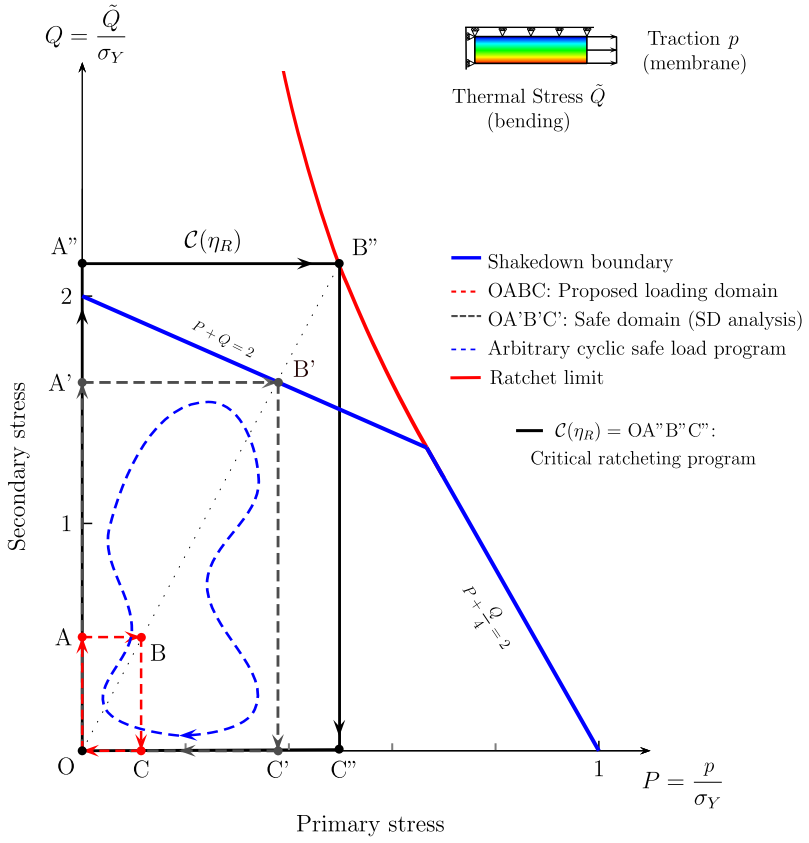

Figure 2.1: Shakedown analysis, definition of the broad safe domain.

Similar amplified programs, with different ratios of primary (load controlled) P and secondary (displacement controlled) stresses Q, build the SD boundary. That is, rectangles with different aspect ratios generate the shakedown limits when amplified through SD analysis. Figure 2.1 includes the mechanical model adopted for this example.

Unfortunately, structural components often have stress concentration regions which reduce shakedown probability. In such positions, stress levels are typically higher than SD limits. In pressure vessels, shell to nozzle transitions or shell to support attachments are some examples. Depending on the stress levels, the risk of alternating plasticity or structural ratcheting rises.

Shakedown analysis and the determination of a ratchet boundary are distinct analyses, although related in many ways. A main difference is that the ratchet-limit factor η_{R} applies to a single cyclic loading $\mathcal{C}$ (for instance, OA"B"C" in Figure 2.1) while the shakedown safety factor μ refers to arbitrary loadings contained in

a prescribed load domain Δ (Ponter and Chen, 2001, Sec. 2.1, p. 540). Even if one compares the ratchet critical factor for a cycle $\mathcal{C}$ to the shakedown factor with respect to the same cycle $\mathcal{C}$ (or its enclosing convex hull) different results occur, whenever the critical shakedown mechanism is alternating plasticity. The latter is the case of principal interest in searching for the ratchet boundary since alternating plasticity is sometimes admissible.

Concerning structural integrity, ratcheting is critical. The plastic strain accumulation has the potential to cause incremental collapse or turning the structure unserviceable. Moreover, when low cycle fatigue and ratcheting interact, uncertainties arise turning difficult to predict material damage evolution (Rahman et al., 2008; Varvani-Farahani and Nayebi, 2018).

Thus, ratcheting prevention develops itself into a design requirement (Kalnins and Rudolph, 2011; Polizzotto, 1993a,b; Reinhardt, 2003; Rudolph et al., 2011).

This section focus on structural ratcheting, rather than material ratcheting, as defined in Hubel (1996). The lack of material models capable of representing multi-axial material ratcheting in detail (Chaboche, 2008; Hassan et al., 2008; Khutia et al., 2015; Krishna et al., 2009; Rahman et al., 2008) justifies such scope limitation.

Despite of the progress of the non-linear kinematic hardening rules, focusing to reproduce experimental ratcheting (see Bari and Hassan (2002); Chaboche (1991); Jiang and Sehitoglu (1996); Ohno and Wang (1993) and many others), multi-axial stress histories still represent a challenge. Moreover, those rules are modified versions of the Armstrong and Frederick (1966) model, thus sharing its lack of mathematical proof on the existence and uniqueness of cyclic steady-state solutions (Zouain and SantAnna, 2018).

The ideal plasticity model still appears as the middle ground choice to evaluate structural ratcheting (Chaboche, 2008, p. 1675; Kalnins and Rudolph, 2011, p. 4), regardless of its known limitation to reproduce material ratcheting even under uniaxial condition with controlled loads.

Pressure vessel design codes and fitness for service standards contain criteria targeting ratcheting prevention. The simplified versions include determination of unlimited elastic stresses, categorization and comparison with limits based on the analytic solution determined by Bree (1967).

Conversely, stresses acting in pressure vessels, for example, are frequently multi-axial and not limited to a constant primary membrane and cyclic secondary bending stresses. Those differences modify shakedown and ratcheting boundary positions when compared to the classical Bree solution. But in practice, the application of general simplified criteria minimizes the risk of failure, when conservative assumptions hold true.

However, as a consequence of mechanical model differences, particular cases may

turn simplified criteria non-conservative, as pointed by Reinhardt (2003, p. 6–7), Carter (2005a, p. 16) and Zheng et al. (2017, p. 8).

During the last decades, the identification of ratchet boundaries became an active area of research. König (1987, Sec. 4.5) includes a general criterion against incremental collapse. Polizzotto (1993a,b) addresses equations governing steady-state solutions, basic properties, a minimum principle and theorems concerning the ratchet limit direct solution. Ponter and Chen (2001) also established a minimum principle and an analogous theorem for the location of a ratchet boundary.

The referred principles and theorems consider as premise a loading system composed by a sustained load acting with a cyclic loading program. The limit identification occurs when the amplified permanent load, superposed to the cyclic program, renders an imminent state of ratcheting. With such strategy, the intent is to measure the increment of permanent load that causes an incremental collapse in a cyclically loaded structure. Thus, the presence of a sustained load is not only necessary but also constitutes a metric for the distance to the failure.

Direct methods to identify the boundary emerged, following those principles, theorems and the proposed loading system. Examples are the linear matching method (Chen and Ponter, 2001, 2010; Ure et al., 2011), non-cyclic elastic modulus adjustment procedure (Adibi-Asl and Reinhardt, 2011a,b; Reinhardt, 2008a), hybrid procedures (Jappy et al., 2013a,b; Martin and Rice, 2009) and yield surface modification method (Abou-Hanna and McGreevy, 2011). Recently an algorithm capable of treating proportional loading cases appeared (Lytwyn et al., 2015a,b).

Adopting a different path, Martin (2008) applies direct cyclic analysis (DCA) driven by a bisection procedure to identify the ratcheting limit for general loading conditions. DCA assumes a truncated Fourier series as the periodic solution for the stable cycle. The method adjusts the series coefficients with a minimization procedure.

Analytical solutions, including more general loading conditions, are still unfolding for problems in which it is feasible (Bradford, 2012, 2015, 2017; Bree, 1989; Ng and Moreton, 1986; Reinhardt, 2008b; Shen et al., 2018; Zheng et al., 2017, 2015; Zouain, 2018). New solutions contribute as references for comparison with numerical results and to analyze sensitivity to more general loading conditions.

The incremental elastoplastic time history integration is an alternative to build bounds. Using the same procedure for boundary determination by trial and error constitutes an option, but it is computationally expensive when the problem requires a refined mesh. Unfortunately, two nested trial and error procedures are necessary. The first to achieve steady cycle and the second to search for the ratchet limit position.

In contrast with the Bree problem, in which stabilization occurs after the second

cycle, more general problems tend to stabilize with a higher number of cycles (not known in advance), as noted by Reinhardt (2003) and Martin (2008).

This behavior turns the history integration procedure costly, once a structure has to be cycled until stabilization when searching for the ratchet boundary. Moreover, when dealing with ratchet limit determination using step-by-step incremental procedure, Carter (2005b, p. 30) arguments with precision: "*Unless there is an ability to calculate the plastic cyclic solution directly, the distinction between reverse plasticity and ratcheting is often unclear in all but the simplest of structures*".

Chapter 5 describes a novel direct method to identify the ratchet boundary for an elastoplastic structure submitted to a cyclic loading program (SantAnna and Zouain, 2018).

2.3 On nonlinear kinematic hardening and material ratcheting

The contents of the present section follows the literature review from Zouain and SantAnna (2018).

Using nonlinear kinematic hardening allows representing the material ratcheting phenomenon, experimentally observed for homogeneous non-symmetric stress cycles (Armstrong and Frederick (1966),Jirásek and Bazant (2002, p.327)).

In contrast, ideal plasticity or (some) isotropic hardening may represent structural ratcheting (Hubel, 1996) and these approximations are acceptable in many situations.

Indeed, König and Maier (1981, Sec.12 p. 92–93) argument: "*Theoretical and experimental results on SD loads and, when available, on incremental collapse mechanisms, appear to be in fairly good agreement...*". Furthermore: "*For ductile steel structures the fact that experimental SD loads are normally slightly higher than experimental values can be probably justified by the influence of hardening neglected in the numerical analysis...*". Besides: "*Stabilization observed in experiments occurs after a number of cycles which is often larger than that predicted theoretically (say 5-20 instead of 1-2) . This discrepancy can be probably due to the fact that the actual generalized stress-strain relation varies from cycle to cycle and stabilizes only after several cycles.*". In addition, the referred data is directly related with ratcheting, once most of the experiments measure "*the increment of displacement at two subsequent unloaded situations*".

Therefore, when the case under analysis calls for a more reliable model, the expectation is that nonlinear kinematic hardening models can give more realistic progressive strain accumulation in structures under variable loadings. See Chaboche

(2008, p. 1675) and Abdel-Karim (2005) for discussions about these issues.

Accordingly, the inclusion of Armstrong Frederick (AF) nonlinear kinematic hardening in the computational formulation for the cyclic response of structures aims to improve the capability of the method in accurately predict the material ratcheting phenomenon.

It is worth to mention that the AF nonlinear kinematic hardening is non-associated and this has significant theoretical and computational consequences on the determination of the asymptotic response.

Elastoplastic solids, with associated models, under periodic loadings undergo long-term states of stress, plastic strain rates and internal variables, which are cyclic and with the same period of the load. The time derivatives of plastic strains and internal variables in the stabilized response are unique in the sense that are independent of initial conditions. Furthermore, in regions of the body where the plastic strain rate is nonzero the uniqueness (meaning indifference to initial conditions) is assured for stresses, plastic strains and internal variables. In the complementary region, the asymptotic fields of plastic strains and internal variables are independent of time but dependent on initial conditions.

Frederick and Armstrong (1966) and Polizzotto (1994a,b) proved these facts, but assuming associativity of both the plastic flow and the hardening evolution.

The direct approach to the computation of steady state cyclic responses, for materials obeying associative plastic flow laws, has been addressed by several researchers, notably Gokhfeld and Charniavsky (1980); Maitournam et al. (2002); Peigney and Stolz (2003); Ponter and Chen (2001); Spiliopoulos and Panagiotou (2012).

To the best of the author knowledge, there is no direct procedure for cyclic responses able to include nonlinear kinematic hardening; besides the one in Zouain and SantAnna (2017), where the inclusion appears in Zouain and SantAnna (2018).

Despite computational evidences that the Armstrong-Frederick model behaves asymptotically cyclic under repeated loads, there is no theoretical proof that an elastoplastic solid obeying the AF model always stabilize cyclically for periodic loads.

Moreover, there is no proof of existence of a cyclic solution under repeated loads with AF hardening. This is in contrast with the case of Generalized Standard Materials (GSM) thoroughly considered by Polizzotto (1994a).

In view of this, this section explains the sense of the problem of computation of steady-state solution with AF kinematic hardening.

First, theoretical issues concerning: (i) uniqueness of solution in incremental analysis, (ii) conditions assuring elastic shakedown and (iii) asymptotic response under cyclic loads, are related and often treated using the same key equations or mathematical properties. Here, a crucial monotonicity property of the evolution

relation between thermodynamic forces and generalized plastic flows is identified, valid for some GSM-materials (with an additional assumption on convexity), given by the inequality (65) of Halphen and Nguyen (1975).

In short, it states that, considering two arbitrary pairs of generalized plastic strain rates and stresses, with each pair associated by the evolution relation, the scalar product of the respective differences is always nonnegative.

Indeed, the monotonicity property (65) of Halphen and Nguyen (1975) is used, in that paper, to prove uniqueness of the stress field and internal parameters in incremental analysis.

Afterwards, Polizzotto (1994b), addressing GSM-solids under repeated loads, used the same inequality (labeled (5) in Polizzotto (1994b)) to prove convergence of any incremental solution to an asymptotic cyclic response. It is remarkable that Frederick and Armstrong (1966) used a similar equation labeled (20) in that paper to prove the existence and uniqueness of the steady state for elastoplastic solids absent of hardening and obeying Drucker postulate.

Chelminski (2003) identifies lack of monotonicity as the main difficulty in the mathematical analysis of the AF model. Moreover, all attempts to assess well-posedness of this model, for instance those by Dettmer and Reese (2004), Francfort and Stefanelli (2013) and Chełmiński et al. (2015), involve modifications of the original equations.

de Saxcé et al. (2000), Bodovillé and de Saxcé (2001) and Bouby et al. (2015) addressed shakedown analysis with nonlinear kinematic hardening from the viewpoint of non-smooth mechanics and using the concept of bipotentials.

Quoting from de Saxcé et al. (2000, p.170): *"Unfortunately, no generalisation of Melans theorem to material admitting a bipotential has been rigorously proved up to now."* In the same paper, the authors propose two coupled optimization problems aimed to give upper and lower bounds to the shakedown load factor of structures admitting bipotential representation. To the author knowledge, there is no published stability assertion, similar to the statical shakedown theorem of Bleich and Melan, and valid for AF nonlinear kinematic hardening.

Also in other problems of inelastic solids, lack of monotonicity complicates the analysis of uniqueness of incremental solutions and shakedown conditions. This happens in the incremental problem for elastic perfectly plastic structures with temperature dependent elastic coefficients. Nevertheless, Halphen (2005) and Peigney (2014) established theoretical results for the asymptotic behavior and uniqueness of solutions to this problem. In a similar example of lack of monotonicity, Ahn et al. (2008) addressed the shakedown analysis of coupled two-dimensional discrete frictional systems. Both Ahn et al. (2008) and Peigney (2014) identified systems where some loading results in an elastic steady state for certain initial condition while the

same loading combined with some other initial conditions leads to cyclic plasticity (slip).

Similarly, Polizzotto and Borino (1996) developed an extension of classical shakedown theory to large displacements, where the authors point out that, under the assumptions of their formulation, *"ratchetting as a steady-state response to periodic loads has been found to be impossible"*.

As in the previous references, this calls for caution in the generalization of numerical results for cyclic loading on non-standard structures, in both the conventional incremental approach and the direct asymptotic analysis.

Bearing in mind the studies referenced above, the aim of chapter 6 is: to describe an efficient procedure to compute directly a strictly cyclic steady state for a solid with AF nonlinear kinematic hardening.

Alternatively, this response could be obtained using conventional incremental analysis by taking any state in the directly computed cycle as initial condition (Polizzotto, 2003, p. 2679).

The computational method is assessed, in the examples of section 6.7, by comparing the direct numerical solutions with a conventional step-by-step integration corresponding to trivial initial conditions; in all cases, they closely match. This suggests that the cyclic solution is unique; but obviously, this is not a proof.

However, the devised direct method is a tool to investigate, numerically, the asymptotic behavior of these systems. Besides, according to uniqueness properties proven for GSM materials, direct approaches cannot guarantee to match stresses and plastic strains in the elastic parts of the structure, where they depend on initial conditions.

Chapter 3

Theory Review

3.1 Elastic-ideally plastic model

3.1.1 Kinematics

A structural body occupies a region $\mathcal{B}$ with a boundary Γ. The boundary Γ has two complementary parts, Γ_u and Γ_τ, where displacements and surface forces act, respectively.

The equation (3.1) defines tangent deformation operator

$$\mathcal{D}\boldsymbol{v} = \frac{1}{2}\left(\nabla\boldsymbol{v} + (\nabla\boldsymbol{v})^T\right), \tag{3.1}$$

where $\nabla\boldsymbol{v}$ denotes the gradient of the vector $\boldsymbol{v}$.

The operator $\boldsymbol{\mathcal{D}}$ maps the velocity fields $\boldsymbol{v}$ into *compatible* strain rate tensors $\boldsymbol{d}$. Under small deformations hypothesis, the same operator $\boldsymbol{\mathcal{D}}$ maps displacement fields $\boldsymbol{u}$ into *compatible* strain tensors $\boldsymbol{\varepsilon}$.

$$\boldsymbol{\mathcal{D}u} = \boldsymbol{\varepsilon} \qquad \boldsymbol{\mathcal{D}v} = \boldsymbol{d} \tag{3.2}$$

Consequently, the displacement fields $\boldsymbol{u}$ and the compatible strains $\boldsymbol{\varepsilon}$ are directly related by $\mathcal{D}$ mapping, as well as, compatible strain rates $\boldsymbol{d}$ and velocity fields $\boldsymbol{v}$.

3.1.2 Equilibrium

The equilibrium operator $\boldsymbol{\mathcal{D}'}$ maps stress tensors $\boldsymbol{\sigma}$ into applied external forces $\boldsymbol{F}$.

$$\mathcal{D}'\boldsymbol{\sigma} = \boldsymbol{F} \tag{3.3}$$

3.1.3 Virtual power principle

A power of external forces $\dot{W}_e$, considering *any* virtual velocities field $\boldsymbol{v}^*$, *compatible* with the applied constraints, is

$$\dot{W}_e = \int_{\mathcal{B}} \boldsymbol{b} \cdot \boldsymbol{v}^* \, d\mathbf{x} + \int_{\Gamma_\tau} \boldsymbol{\tau} \cdot \boldsymbol{v}^* \, d\Gamma. \tag{3.4}$$

Where $\boldsymbol{b}$ and $\boldsymbol{\tau}$ are the body and surface load densities, defining $\boldsymbol{F}$; and $\mathbf{x}$ is a material point.

An internal virtual power $\dot{W}_i$, for a virtual strain rate field $\boldsymbol{d}^*$ is

$$\dot{W}_i = \int_{\mathcal{B}} \boldsymbol{\sigma} \cdot \boldsymbol{d}^* \, d\mathbf{x}. \tag{3.5}$$

A virtual strain rate tensor $\boldsymbol{d}^*$ results from computing the deformation operator $\boldsymbol{\mathcal{D}}$ on proposed virtual velocities field $\boldsymbol{v}^*$, using equation (3.2).

The virtual power principle states that internal power $\dot{W}_i$ equals external power $\dot{W}_e$. That is, the internal power due to body straining is identical to the power of external forces. This principle is equivalent to body forces equilibrium.

$$\int_{\mathcal{B}} \boldsymbol{\sigma} \cdot \boldsymbol{d}^* \, d\mathcal{B} = \int_{\mathcal{B}} \boldsymbol{b} \cdot \boldsymbol{v}^* \, d\mathbf{x} + \int_{\Gamma_\tau} \boldsymbol{\tau} \cdot \boldsymbol{v}^* \, d\Gamma \tag{3.6}$$

3.1.4 Yielding criterion and yielding surface

Most of the applications of this thesis adopt elastic-ideally plastic material model that obeys Von-Mises yield criterion. Consequently, equation (3.7) defines the convex yielding function $f(\boldsymbol{\sigma})$, where σ_Y is the yielding stress. Equation (3.8) defines the deviatoric stress tensor $\boldsymbol{S}$, where $\boldsymbol{1}$ is the identity tensor and $\mathrm{tr}\,(\cdot)$ is the trace operator.

$$f(\boldsymbol{\sigma}) = \sqrt{\frac{3}{2}} \|\boldsymbol{S}\| - \sigma_Y \tag{3.7}$$

$$\boldsymbol{S} = \boldsymbol{\sigma} - \frac{1}{3} \, \mathrm{tr}\,(\boldsymbol{\sigma}) \boldsymbol{1} \tag{3.8}$$

where $\|\boldsymbol{S}\| = (\boldsymbol{S} \cdot \boldsymbol{S})^{1/2}$.

The plastic admissibility condition, equation (3.9), assures that stress fields $\boldsymbol{\sigma}$ are constrained inside the set $\mathcal{P}$ formed by admissible stress fields through equation (3.10).

$$f(\boldsymbol{\sigma}) \leq 0 \tag{3.9}$$

$$\mathcal{P} = \{\boldsymbol{\sigma} \mid \ f(\boldsymbol{\sigma}) \leq 0\} \tag{3.10}$$

3.1.5 Constitutive equations

Elastic $\boldsymbol{\varepsilon}^e$, plastic $\boldsymbol{\varepsilon}^p$ and prescribed $\boldsymbol{\varepsilon}^\Theta$ additive decomposition of strains follows equation (3.11)

$$\boldsymbol{\varepsilon} = \boldsymbol{\varepsilon}^e + \boldsymbol{\varepsilon}^p + \boldsymbol{\varepsilon}^\Theta. \tag{3.11}$$

Using equation (3.12), elastic operator $\mathbb{E}$ maps elastic strain $\boldsymbol{\varepsilon}^e$ in stresses $\boldsymbol{\sigma}$. Such operator is symmetric and positive definite, consequently invertible.

$$\boldsymbol{\sigma} = \mathbb{E}\ \boldsymbol{\varepsilon}^e \tag{3.12}$$

$$\boldsymbol{\varepsilon}^e = \mathbb{E}^{-1}\ \boldsymbol{\sigma} \tag{3.13}$$

The elastic behavior is linear and isotropic. Coefficients using the elastic modulus E and Poison ratio ν define the components of the fourth order tensor $\mathbb{E}$.

Prescribed thermal strain $\boldsymbol{\varepsilon}^\Theta$ follows equation (3.14). Where $c_{\boldsymbol{\varepsilon}}$ is the secant coefficient of thermal expansion and $\Delta\Theta(\mathbf{x})$ is the difference between the applied temperature Θ and the reference temperature Θ_{ref} at the material point $\mathbf{x}$.

$$\boldsymbol{\varepsilon}^\Theta = c_{\boldsymbol{\varepsilon}}\Delta\Theta(\mathbf{x})\boldsymbol{1} \tag{3.14}$$

Furthermore, $\boldsymbol{\varepsilon}^\Theta$ can embrace other types of prescribed strains, adding the prescribed strain in the right side of (3.14).

The plastic component $\boldsymbol{\varepsilon}^p$ of the equation (3.11) is a consequence of flow law time integration. The flow law has to describe the non-linear relation between imposed stresses $\boldsymbol{\sigma}$ and the developed plastic strain $\boldsymbol{\varepsilon}^p$.

For a material point $\mathbf{x}$ loaded in the plastic regime a saturation behavior in the developed stress $\boldsymbol{\sigma}$ occurs in experiments. Moreover, if an unloading condition applies, the plastic strain $\boldsymbol{\varepsilon}^p$ stays unchanged. The unloading path is elastic, with a linear change in the developed stress $\boldsymbol{\sigma}$. Furthermore, experiments show negligible volume changes during plastic straining.

The referred set of experimental evidence demands a non-linear rule relating stress and strain increments including thresholds. The thresholds activate the stress saturation and the elastic unloading.

Equation (3.15) express the volume invariance of the plastic strain.

$$\operatorname{tr}(\boldsymbol{\varepsilon}^p) = 0 \tag{3.15}$$

That is, $\boldsymbol{\varepsilon}^p$ is a deviatoric tensor, as well as, the plastic strain rate $\boldsymbol{d}^p = \dot{\boldsymbol{\varepsilon}}^p$.

Interpretation of experimental data shows evidences of proportionality between the plastic strain rate $\boldsymbol{d}^p$ and the deviatoric stress tensor $\boldsymbol{S}$.

The normal stress unity tensor is

$$\boldsymbol{n} = \frac{1}{\|\boldsymbol{S}\|}\boldsymbol{S}, \tag{3.16}$$

where $\|\boldsymbol{S}\| = (\boldsymbol{S} \cdot \boldsymbol{S})^{1/2}$ is the euclidean norm of the tensor $\boldsymbol{S}$. The proportionality between deviatoric stresses $\boldsymbol{S}$ and plastic strain rate $\boldsymbol{d}^p$ follows

$$\boldsymbol{d}^p = \sqrt{\frac{3}{2}}\dot{\lambda}\boldsymbol{n}. \tag{3.17}$$

Taking Euclidean norms at both sides of equation (3.17), the definition of the plastic strain rate multiplier becomes evident. It is a Von Mises equivalent of plastic strain rate.

$$\dot{\lambda} = \sqrt{\frac{2}{3}}\|\boldsymbol{d}^p\| = d^p_{eq} \tag{3.18}$$

The above definition imposes constrains to the plastic strain rate multiplier $\dot{\lambda}$. (i) It is non-negative $\dot{\lambda} \geq 0$, once it is an euclidean norm. (ii) Elastic action occurs when the stress $\boldsymbol{\sigma}$ is inside the yield surface, thus, if $f(\boldsymbol{\sigma}) < 0$ (elastic action), then $\dot{\lambda} = 0$. (iii) Else, when the stress $\boldsymbol{\sigma}$ reaches yield surface, that is $f(\boldsymbol{\sigma}) = 0$, plastic action may occur $\dot{\lambda} \geq 0$, depending on the loading condition. Conditions (ii) and (iii) obey the condensed equation $\dot{\lambda} f(\boldsymbol{\sigma}) = 0$.

Those constrains, summarized in (3.19), are the complementary equations of the flow rule in ideal plasticity. In summary,

$$\dot{\lambda} f(\boldsymbol{\sigma}) = 0 \qquad \dot{\lambda} \geq 0 \qquad f(\boldsymbol{\sigma}) \leq 0. \tag{3.19}$$

Equation (3.19) additionally includes the plastic admissibility of the stresses, that is $f(\boldsymbol{\sigma}) \leq 0$.

Recalling that the gradient operation ∇ applied in a surface gives a normal to the surface, the set of equations (3.20) summarizes normality rule and its complementary equations.

$$\boldsymbol{d}^p = \dot{\lambda}\nabla f(\boldsymbol{\sigma}) \qquad \dot{\lambda}\ f(\boldsymbol{\sigma}) = 0 \qquad \dot{\lambda} \geq 0 \qquad f(\boldsymbol{\sigma}) \leq 0 \tag{3.20}$$

Equation (3.21) alternatively evokes the same rule, but using convex analysis definitions, as presented in Maugin (1992).

$$\boldsymbol{d}^p \ \in \ \mathcal{N}_{\mathcal{P}} \tag{3.21}$$

It means that plastic strain rates $\boldsymbol{d}^p$ shall be in the set formed by *cone of normals* $\mathcal{N}_p$ to the plastic surface $f(\boldsymbol{\sigma})$.

The plastic dissipation rate function $\mathrm{d}_{\mathrm{int}}(\boldsymbol{d}^p)$ is the supremum of the contraction product between admissible stresses $\boldsymbol{\sigma}$ and plastic strain rate $\boldsymbol{d}^p$, following equation (3.22).

$$\mathrm{d}_{\mathrm{int}}(\boldsymbol{d}^p) = \sup_{\boldsymbol{\sigma}\in\mathcal{P}}(\boldsymbol{\sigma}\cdot\boldsymbol{d}^p) \tag{3.22}$$

An important highlight is the dissipation rate function $\mathrm{d}_{\mathrm{int}}(\boldsymbol{d}^p)$ independence of stress tensor $\boldsymbol{\sigma}$. The supremum function together with the bounded characteristic of stresses, imposed by plastic admissibility, result in the independence of the stress tensor $\boldsymbol{\sigma}$.

Along with $f(\boldsymbol{\sigma})$ convexity, the definition of the dissipation rate function $\mathrm{d}_{\mathrm{int}}(\boldsymbol{d}^p)$ is equivalent to Drucker stability postulate, reproduced in equation (3.23).

$$(\boldsymbol{\sigma}-\boldsymbol{\sigma}^*)\cdot\boldsymbol{d}^p \geq 0 \tag{3.23}$$

In the referred postulate, $\boldsymbol{\sigma}^*$ is an arbitrary plastically admissible stress, that is $\boldsymbol{\sigma}^* \in \mathcal{P}$.

The set of constitutive equations applies for an elastic-ideally plastic material model. The model forms the basic constitutive field where classical limit load and shakedown theorems apply.

The incremental form of plasticity constitutive equations results in the requirement of time integration if one wants to determine the plastic strain tensor $\boldsymbol{\varepsilon}^p$, which thus, depends on the local stress history (path dependence).

3.2 Limit analysis

3.2.1 Definitions

Before recalling limit load theorems, this section reviews some key definitions.

A velocity field $\boldsymbol{v}$ is compatible, if $\boldsymbol{v}$ fulfills the prescribed velocity boundary conditions at Γ_u and the required regularity conditions.

A strain rate field $\boldsymbol{d}$ is compatible, if $\boldsymbol{d}$ is obtained by applying deformation operator $\mathcal{D}$ into a compatible velocity field $\boldsymbol{v}$.

A stress state $\boldsymbol{\sigma}$ is static admissible if $\boldsymbol{\sigma}$ satisfies equilibrium with the applied set of external forces.

A stress state $\boldsymbol{\sigma}$ is plastic admissible if $\boldsymbol{\sigma}$ is interior to plastic surface $f(\boldsymbol{\sigma}) \leq 0$. In other words, if $\boldsymbol{\sigma} \in \mathcal{P}$.

3.2.2 Limit load statical theorem

The plastic admissibility $f(\boldsymbol{\sigma}) \leq 0$ and the equilibrium $\mathcal{D}'\boldsymbol{\sigma} = \boldsymbol{F}$ enforce a limit on the level of external load $\boldsymbol{F}$ that a structure can support.

Any stress field $\boldsymbol{\sigma}$ that satisfies plastic admissibility and equilibrium all over the body constitutes a lower bound to the refereed limit.

The limit load problem consists in the identification of the maximum amplified imposed load $\alpha\boldsymbol{F}$ that equilibrates with a plastic admissible stress field $\boldsymbol{\sigma}$, that is $f(\boldsymbol{\sigma}) \leq 0$. In this sense, the statical limit load theorem states that the limit load $\alpha\boldsymbol{F}$ is obtained solving the following maximization problem.

$$\alpha = \sup(\alpha^*) \tag{3.24}$$

such that

$$\mathcal{D}'\boldsymbol{\sigma} = \alpha^*\boldsymbol{F} \qquad f(\boldsymbol{\sigma}) \leq 0. \tag{3.25}$$

Such theorem is commonly named the *lower bound* for the limit load (Kachanov, 2004; Lubliner, 2008).

3.2.3 Limit load kinematical theorem

Using optimization duality on statical theorem, it is possible to demonstrate the kinematic limit load theorem (Krabbenhøft et al., 2007a).

During plastic collapse, the extinction of the body capacity of elastically respond to external power occurs. Consequently, external power turns into plastic dissipation rate.

Hence, considering a proposed virtual compatible velocity field $\boldsymbol{v}^*$ during collapse (namely, a collapse mechanism), one can determinate the corresponding applied load $\alpha^*\boldsymbol{F}$, which is capable of causing the instantaneous failure, equaling the total plastic dissipation rate $\int_{\mathcal{B}} \mathrm{d}_{\mathrm{int}}(\boldsymbol{d}^{p*})\ d\mathbf{x}$ to external power $\alpha^*\dot{W}_e$. This procedure produces an upper bound for the limit load.

The arising question is why the amplification factor found is an upper bound and not the collapse amplification factor itself? The answer lies in the fact that proposed collapse mechanism (virtual velocity field $\boldsymbol{v}^*$) is not necessarily the most incipient one. If one proposes the most incipient mechanism, he reaches exactly the collapse amplification factor α.

Consequently, the procedure to reach the limit load is finding the minimum amplification factor α^*, and correspondent collapse mechanism $\boldsymbol{v}^*$.

$$\alpha = \inf(\alpha^*) \tag{3.26}$$

such that

$$\alpha^* = \frac{\int_{\mathcal{B}} \mathrm{d}_{\mathrm{int}}(\boldsymbol{d}^{p*})\ d\mathbf{x}}{\dot{W}_e} \qquad \boldsymbol{d}^{p*} = \mathcal{D}\boldsymbol{v}^*. \tag{3.27}$$

A highlight in limit load theorems is the independence of stresses developed due to the imposed strain $\boldsymbol{\varepsilon}^{\Theta}$. Only the stresses equilibrating the external force $\boldsymbol{F}$ are important to the plastic collapse load determination.

3.3 Shakedown analysis

3.3.1 Introduction

Considering cyclic loads applied in structures, the response (including the transient phase) belongs to one of the following classes.

Purely Elastic: yield surface is not reached in any point of the structure. In consequence no plastic dissipation occurs. The response is a steady-state with no transient phase.

Shakedown: the structure has plastic strains active just in a finite number of cycles, during a transient phase. After that, the response to the loading program is elastic all over the body. Consequently, the plastic dissipation is bounded.

Alternating Plasticity: in each steady-state cycle, plastic strains occur, but they oppose each other resulting in zero net plastic strain at the end of the cycle. As a result, the plastic dissipation is unbounded.

Incremental Collapse: the plastic strains occurring at each steady-state cycle accumulate causing collapse after a finite number of cycles. The cumulative plastic strain also results in unbounded plastic dissipation.

Plastic Collapse: the primary loads range is higher than the structure limit load. As a consequence, the structure collapses at the instant when the primary load reaches the limit load. Plastic dissipation is unbounded.

The above responses arrangement obeys a decreasing order of safety. Under a different perspective, considering structures such pressure vessels, some responses can be re-ordered by hardness of achievement. At stress concentration regions, the elastic response is rarely achieved. Shakedown may occur in some cases, while in others it is necessary to accept alternating plasticity. Depending on the amount of cycles, care shall be taken to prevent low cycle fatigue.

In consequence of design criteria, the occurrence of incremental collapse (ratcheting) or instantaneus plastic collapse are unusual, in general causing accidents.

3.3.2 Load domain definition

Assuming an unlimited elastic body, the following system of equations relates stresses $\boldsymbol{\sigma}^E(t)$, applied forces $\boldsymbol{F}(t)$ and imposed strains $\boldsymbol{\varepsilon}^\Theta(t)$.

$$\boldsymbol{\mathcal{D}}\boldsymbol{u}^E(t) = \boldsymbol{\varepsilon}(t) \tag{3.28}$$

$$\mathcal{D}'\boldsymbol{\sigma}^E(t) = \boldsymbol{F}(t) \tag{3.29}$$

$$\boldsymbol{\varepsilon}(t) = \boldsymbol{\varepsilon}^E(t) + \boldsymbol{\varepsilon}^\Theta(t) \tag{3.30}$$

$$\boldsymbol{\sigma}^E(t) = \mathbb{E}\ \boldsymbol{\varepsilon}^E(t) \tag{3.31}$$

In the above system, $\boldsymbol{u}^E(t)$ is the displacement solution due to applied external loads $\boldsymbol{F}(t)$ and imposed strains $\boldsymbol{\varepsilon}^\Theta(t)$.

The definition of the stiffness operator

$$\boldsymbol{\mathcal{K}} := \boldsymbol{\mathcal{D}}'\mathbb{E}\boldsymbol{\mathcal{D}}, \tag{3.32}$$

allows describing the displacement solution by

$$\boldsymbol{u}^E(t) = \boldsymbol{\mathcal{K}}^{-1}\left(\boldsymbol{F}(t) + \boldsymbol{\mathcal{D}}'\mathbb{E}\boldsymbol{\varepsilon}^\Theta(t)\right), \tag{3.33}$$

when $\boldsymbol{\varepsilon}(t)$, $\boldsymbol{\sigma}^E(t)$ and $\boldsymbol{\varepsilon}^E(t)$ are eliminated from the system.

Further substitutions and the definition of the residual operator

$$\boldsymbol{\mathcal{Z}} := \mathbb{E}\boldsymbol{\mathcal{D}}\boldsymbol{\mathcal{K}}^{-1}\boldsymbol{\mathcal{D}}'\mathbb{E} - \mathbb{E}, \tag{3.34}$$

directly correlate the applied load $\boldsymbol{F}(t)$ and the imposed strains $\boldsymbol{\varepsilon}^\Theta(t)$ with the unlimited elastic stresses $\boldsymbol{\sigma}^E(t)$, through equation (3.35).

$$\boldsymbol{\sigma}^E(t) = \mathbb{E}\boldsymbol{\mathcal{D}}\boldsymbol{\mathcal{K}}^{-1}\boldsymbol{F}(t) + \boldsymbol{\mathcal{Z}}\boldsymbol{\varepsilon}^\Theta(t) \tag{3.35}$$

In shakedown analysis, it becomes convenient to work with the elastic unlimited stresses $\boldsymbol{\sigma}^E(t)$ to represent the applied loadings $\boldsymbol{F}(t)$ and imposed strains $\boldsymbol{\varepsilon}^\Theta(t)$.

It is assumed that the applied loads can be decomposed by

$$\boldsymbol{F}(t) = \sum_{i=1}^{n} \phi_i(t)\boldsymbol{F}_i \qquad \boldsymbol{\varepsilon}^\Theta(t) = \sum_{i=1}^{n} \phi_i(t)\boldsymbol{\varepsilon}_i^\Theta, \tag{3.36}$$

as described in König and Maier (1981), where $\phi_i(t)$ are temporal functions that

scale fixed loads $\boldsymbol{F}_i$ and fixed imposed strains $\boldsymbol{\varepsilon}_i^{\Theta}$.

$$\boldsymbol{\sigma}^E(t) = \sum_{i=1}^{n} \phi_i(t)\boldsymbol{\sigma}_i^E \qquad \boldsymbol{\sigma}_i^E = \mathbb{E}\boldsymbol{\mathcal{D}}\boldsymbol{\mathcal{K}}^{-1}\boldsymbol{F}_i + \boldsymbol{\mathcal{Z}}\boldsymbol{\varepsilon}_i^{\Theta}. \tag{3.37}$$

Thus, $\{\boldsymbol{\sigma}_i^E \mid i = 1..n\}$ forms a set of load vertexes. The convex hull of this set

$$\Delta := \mathrm{Conv}\left(\{\boldsymbol{\sigma}_i^E \mid i = 1..n\}\right) \tag{3.38}$$

defines a load domain encompassing $\boldsymbol{\sigma}^E(t)$.

3.3.3 Shakedown: statical formulation

As the steady-state response of a structure which progressed to shakedown is elastic, the plastic dissipation is bounded.

That is,

$$\int_0^t \int_{\mathcal{B}} \mathrm{d}_{\mathrm{int}}(\boldsymbol{d}^p)\ d\mathbf{x}\ dt^* \ = c \quad \forall\ t \geq \bar{t}, \tag{3.39}$$

where c is a arbitrary constant and $\bar{t}$ is the time to reach the steady-state.

Melan (1938) proved that a sufficient condition for shakedown in a body with applied loads scaled by the factor μ^*, represented through unlimited elastic stresses $\mu^*\boldsymbol{\sigma}^E(t)$, is the existence of a *time independent* residual stress field $\boldsymbol{\sigma}^r$ that when superposed to the *time dependent* elastic stresses $\mu^*\boldsymbol{\sigma}^E(t)$ results a plastic admissible stress field $\boldsymbol{\sigma}(t)$ for all time. That means

$$\boldsymbol{\sigma}(t) = \mu^*\boldsymbol{\sigma}^E(t) + \boldsymbol{\sigma}^r \tag{3.40}$$

$$\mathcal{D}'\boldsymbol{\sigma}(t) = \mu^*\boldsymbol{F}(t) \tag{3.41}$$

$$f(\boldsymbol{\sigma}(t)) \leq 0. \tag{3.42}$$

Similar to limit load analysis, the shakedown factor μ may be reached searching for the maximum amplifying factor μ^* and correspondent residual stresses $\boldsymbol{\sigma}^r$, which satisfy the above set of equations. As the shakedown factor μ is a maximum, μ^* configures a lower bound.

With aid of set theory and above load domain definitions, the shakedown equations (3.40), (3.41) and (3.42) may be reduced to equation (3.43).

$$\mu^*\Delta + \boldsymbol{\sigma}^r \ \subset\ \mathcal{P} \tag{3.43}$$

3.3.4 Shakedown: kinematical formulation

Koiter (1956) proposed another theorem for the same problem, based in the un-

bounded plastic dissipation. *"Shakedown is impossible if no time-independent distribution of residual stresses can be found with the property that the sum of residual stresses and elastic stresses is an allowable state of stress (possibly attaining the yield surface) at every point of the body and for all possible load combinations."* The cited statement is represented by the non-shakedown equation (3.44) (Zouain, 2018).

$$\mu^* \Delta + \boldsymbol{\sigma}_r \not\subset \mathcal{P} \tag{3.44}$$

If equation (3.44) holds true, μ^* is an upper bound for the shakedown factor μ. With optimization theory duality assistance, it is possible to prove Koiter's kinematic theorem from Melan's static theorem.

Appendix A has shows that the residual operator $\boldsymbol{\mathcal{Z}}$ definition aids in the shakedown theorems interpretation by establishing the linear relation between $\boldsymbol{\varepsilon}^p$ and $\boldsymbol{\sigma}^r$. Once the latter becomes fixed in time, the former becomes time independent.

Chapter 4

Direct Computation of Steady States

The present chapter partially follows Zouain and SantAnna (2017). The aim is to devise a method for direct computation of asymptotic response for an elastic-ideally plastic structure submitted to cyclic loads.

4.1 General equations

In summary, the relations governing the incremental elastoplastic problem are: the kinematical eq.(3.2); the equilibrium eq.(3.3); the state equations (3.11) and (3.12) (strains decomposition and elastic mapping); and the plastic strain evolution equation (3.21) (alternatively (3.20)), together with suitable prescribed initial conditions. The referred equations are reviewed in sequel.

$$\boldsymbol{\mathcal{D}u} = \boldsymbol{\varepsilon} \qquad \boldsymbol{\mathcal{D}v} = \boldsymbol{d} \tag{3.2}$$

$$\mathcal{D}'\boldsymbol{\sigma} = \boldsymbol{F} \tag{3.3}$$

$$\boldsymbol{\varepsilon} = \boldsymbol{\varepsilon}^e + \boldsymbol{\varepsilon}^p + \boldsymbol{\varepsilon}^\Theta \tag{3.11}$$

$$\boldsymbol{\sigma} = \mathbb{E}\ \boldsymbol{\varepsilon}^e \tag{3.12}$$

$$\boldsymbol{d}^p \ \in\ \mathcal{N}_{\mathcal{P}}(\boldsymbol{\sigma}) \tag{3.21}$$

$$\boldsymbol{d}^p = \dot{\lambda}\nabla f(\boldsymbol{\sigma}) \qquad \dot{\lambda}\ f(\boldsymbol{\sigma}) = 0 \qquad \dot{\lambda} \geq 0 \qquad f(\boldsymbol{\sigma}) \leq 0 \tag{3.20}$$

The combination of equations (3.2), (3.3), (3.11) and (3.12) generates the solution equations (4.1) and (4.2).

$$\boldsymbol{u} = \boldsymbol{\mathcal{K}}^{-1}[\boldsymbol{F} + \boldsymbol{\mathcal{D}}'\mathbb{E}(\boldsymbol{\varepsilon}^p + \boldsymbol{\varepsilon}^\Theta)] \tag{4.1}$$

$$\boldsymbol{\sigma} = \mathbb{E}\boldsymbol{\mathcal{D}}\boldsymbol{\mathcal{K}}^{-1}\boldsymbol{F} + \boldsymbol{\mathcal{Z}}\left(\boldsymbol{\varepsilon}^p + \boldsymbol{\varepsilon}^\Theta\right) \tag{4.2}$$

Where the equations (4.3) recall the positive definite stiffness mapping $\boldsymbol{\mathcal{K}}$ and

the strains to residual stress mapping $\boldsymbol{\mathcal{Z}}$.

$$\boldsymbol{\mathcal{K}} = \boldsymbol{\mathcal{D}}'\mathbb{E}\boldsymbol{\mathcal{D}} \qquad \boldsymbol{\mathcal{Z}} = \mathbb{E}\boldsymbol{\mathcal{D}}\boldsymbol{\mathcal{K}}^{-1}\boldsymbol{\mathcal{D}}'\mathbb{E} - \mathbb{E} \tag{4.3}$$

The operator $\boldsymbol{\mathcal{Z}}$ gives the residual stress field associated with some assumed strain field and has the following properties:

(i) It is symmetric and negative semi-definite. The latter means that the residual stress projection at the increment of plastic strain opposes this increment. Indeed, recalling that the increment of plastic strain is normal to the yield surface and that the residual stress brings an inadmissible elastic stress back to the yield surface, the negative semi-definiteness becomes clear;

(ii) Its range $\mathcal{R}(\boldsymbol{\mathcal{Z}})$ coincides with the linear space of residual stresses (the null space of the equilibrium operator $\mathcal{D}'$). Strictly, stresses computed through the residual operator application are self-equilibrated;

(iii) Its null space $\mathcal{N}(\boldsymbol{\mathcal{Z}})$ coincides with the linear space of compatible strain fields (the range of the compatibility operator $\mathcal{D}$). It means that any compatible strain $\boldsymbol{\varepsilon} = \mathcal{D}\boldsymbol{u}$, with $\boldsymbol{u}$ compatible, gives null residual stresses through $\boldsymbol{\mathcal{Z}}$ mapping;

(iv) it holds $\boldsymbol{\mathcal{Z}}\mathbb{E}^{-1}\boldsymbol{\sigma}^r = -\boldsymbol{\sigma}^r$ for any $\boldsymbol{\sigma}^r$ (in the null space of $\mathcal{D}'$).

The proof of the properties, which play an important role in the presented approach, is in Appendix A of Zouain and SantAnna (2017). The influence operator $\boldsymbol{\mathcal{Z}}$ was first defined by G. Maier (Comi et al., 1992; Maier, 1970).

The pair present in equations set (4.4)

$$\boldsymbol{u}^E = \boldsymbol{\mathcal{K}}^{-1}\left(\boldsymbol{F} + \boldsymbol{\mathcal{D}}'\mathbb{E}\boldsymbol{\varepsilon}^\Theta\right) \qquad \boldsymbol{\sigma}^E = \mathbb{E}\boldsymbol{\mathcal{D}}\boldsymbol{\mathcal{K}}^{-1}\boldsymbol{F} + \boldsymbol{\mathcal{Z}}\boldsymbol{\varepsilon}^\Theta \tag{4.4}$$

denote the solutions of a similar problem, using unlimited elastic material model (see section 3.3.2).

For convenience, the residual (or self-equilibrated) stress field $\boldsymbol{\sigma}^r = \boldsymbol{\sigma} - \boldsymbol{\sigma}^E$ becomes a primary variable, rewriting equations (4.1) and (4.2), using (4.4) and (4.5).

$$\boldsymbol{u} = \boldsymbol{u}^E + \boldsymbol{\mathcal{K}}^{-1}\boldsymbol{\mathcal{D}}'\mathbb{E}\boldsymbol{\varepsilon}^p \qquad \boldsymbol{\sigma} = \boldsymbol{\sigma}^E + \boldsymbol{\sigma}^r \qquad \boldsymbol{\sigma}^r = \boldsymbol{\mathcal{Z}}\boldsymbol{\varepsilon}^p \tag{4.5}$$

4.2 The equations of the asymptotic response (I)

Only cyclic loadings act in the structure. Without loss of generality, the period of the cycle equals 1. Thus, periodic loads verify $\boldsymbol{F}(\hat{t}) = \boldsymbol{F}(\hat{t}+1)$ for all $\hat{t}$. This is also valid for the imposed thermal loadings (prescribed strains $\boldsymbol{\varepsilon}^\Theta$). Furthermore, time in each period m is denoted by $t = \hat{t} - (m-1) \in (0,1)$.

Given a cyclic unlimited elastic stress field $\boldsymbol{\sigma}^E(t)$, which represents the loading

program, the system of equations (4.6) to (4.10) govern the state-state problem.

$$\boldsymbol{\sigma}^E = \mathbb{E}\boldsymbol{\mathcal{D}}\boldsymbol{\mathcal{K}}^{-1}\boldsymbol{F} + \boldsymbol{\mathcal{Z}}\boldsymbol{\varepsilon}^{\Theta} \tag{4.6}$$

$$\boldsymbol{\sigma}^r = \boldsymbol{\mathcal{Z}}\boldsymbol{\varepsilon}^p \tag{4.7}$$

$$\boldsymbol{\sigma} = \boldsymbol{\sigma}^E + \boldsymbol{\sigma}^r \tag{4.8}$$

$$\boldsymbol{d}^p \in \mathcal{N}_{\mathcal{P}}(\boldsymbol{\sigma}) \tag{4.9}$$

$$\boldsymbol{\sigma}(1) = \boldsymbol{\sigma}(0) \tag{4.10}$$

The solution gives $\boldsymbol{\sigma}^r(t)$, $\boldsymbol{\varepsilon}^p(t)$, $\boldsymbol{d}^p(t)$, for $t \in [0,1]$. Where $t = 0$ defines the initial time for a steady-state and $t = 1$ the period of the cycle.

Polizzotto (1993a, p. 319) proposed the same governing equations, with different notation. The equations are analogous to those given in Polizzotto (2003, p. 2679) in the framework of generalized standard materials, thus, with amplified generality.

In the above formulation, the self-equilibrium condition $\boldsymbol{\mathcal{D}}'\boldsymbol{\sigma}^r = \mathbf{0}$ is a consequence of (4.7) because $\mathcal{R}(\boldsymbol{\mathcal{Z}}) = \mathcal{N}(\boldsymbol{\mathcal{D}}')$. Further, the plastic admissibility of $\boldsymbol{\sigma} = \boldsymbol{\sigma}^E + \boldsymbol{\sigma}^r$ is enforced by (4.9) and the periodicity of stress is due to (4.10).

An important consequence of the asymptotic response equations (4.6-4.10) is that the increment of plastic strain accumulated in each cycle, $\Delta\boldsymbol{\varepsilon}$, is compatible. That is, there exists a displacement field $\Delta\boldsymbol{u}$, giving the increment of deformation produced in any cycle, such that

$$\boldsymbol{\mathcal{D}}\Delta\boldsymbol{u} = \Delta\boldsymbol{\varepsilon} \qquad \text{with} \qquad \Delta\boldsymbol{\varepsilon} := \int_0^1 \boldsymbol{d}^p \, dt \tag{4.11}$$

where $\boldsymbol{d}^p$ solves (4.6-4.10).

Indeed, time derivation of (4.7) generates $\dot{\boldsymbol{\sigma}}^r = \boldsymbol{\mathcal{Z}}\boldsymbol{d}^p$ and by integration $\boldsymbol{\sigma}^r(1) - \boldsymbol{\sigma}^r(0) = \boldsymbol{\mathcal{Z}} \int_0^1 \boldsymbol{d}^p \, dt$. Then, using (4.8) and (4.10), $\boldsymbol{\mathcal{Z}} \int_0^1 \boldsymbol{d}^p \, dt = \mathbf{0}$ holds true. But this implies that $\int_0^1 \boldsymbol{d}^p \, dt$ is kinematically admissible, since $\mathcal{N}(\boldsymbol{\mathcal{Z}}) = \mathcal{R}(\boldsymbol{\mathcal{D}})$. This proves (4.11).

It becomes convenient to eliminate from the unknowns of the system (4.6-4.10) the plastic strain field $\boldsymbol{\varepsilon}^p$, which is not cyclic in general. To this end, the following equations are adopted, which equivalently ensure $\boldsymbol{\sigma}^r = \boldsymbol{\mathcal{Z}}\boldsymbol{\varepsilon}^p$.

4.3 The equations of the asymptotic response (II)

Given $\boldsymbol{\sigma}^E(t)$, find $\boldsymbol{\sigma}^r(t)$ and $\boldsymbol{d}^p(t)$ such that

$$\boldsymbol{d}^p \in N_P(\boldsymbol{\sigma}^E + \boldsymbol{\sigma}^r) \tag{4.12}$$

$$\dot{\boldsymbol{\sigma}}^r = \boldsymbol{\mathcal{Z}}\boldsymbol{d}^p \tag{4.13}$$

$$\boldsymbol{\sigma}^r(1) = \boldsymbol{\sigma}^r(0) \tag{4.14}$$

$$\boldsymbol{\mathcal{D}}'\boldsymbol{\sigma}^r(1) = \mathbf{0} \tag{4.15}$$

Note that the constraint

$$\boldsymbol{\mathcal{D}}'\boldsymbol{\sigma}^r(t) = \mathbf{0} \qquad \forall\, t \in (0,1) \tag{4.16}$$

is fulfilled because

$$\boldsymbol{\mathcal{D}}'\boldsymbol{\sigma}^r(t) = \boldsymbol{\mathcal{D}}'\left(\boldsymbol{\sigma}^r(0) + \int_0^t \dot{\boldsymbol{\sigma}}^r(\tau)d\tau\right) = \boldsymbol{\mathcal{D}}'\boldsymbol{\mathcal{Z}}\int_0^t \boldsymbol{d}^p(\tau)d\tau = \mathbf{0} \tag{4.17}$$

according to the properties of the residual operator $\boldsymbol{Z}$ and taking account of (4.13), (4.15) and (4.11).

The system of equations (4.12) to (4.15) is used in the following as the characterization of the asymptotic response to cyclic loadings.

In this formulation, (4.11) constitutes a subsidiary relation determining the increment of displacement per cycle $\Delta\boldsymbol{u}$. The subsidiary problem $\boldsymbol{\mathcal{D}}\Delta\boldsymbol{u} = \Delta\boldsymbol{\varepsilon}$ is consistent and has a unique solution, because $\Delta\boldsymbol{\varepsilon}$ is kinematically compatible and $\boldsymbol{\mathcal{D}}$ is always assumed non-singular ($\mathcal{N}(\boldsymbol{\mathcal{D}})$ is trivial). However, $\Delta\boldsymbol{\varepsilon}$ is only approximately compatible when obtained in the computational solution of the main problem (4.12-4.15) and so the subsidiary problem may become inconsistent. In view of this, $\Delta\boldsymbol{u}$ is computed by solving the linear system

$$\boldsymbol{\mathcal{K}}\Delta\boldsymbol{u} = \boldsymbol{\mathcal{D}}'\mathbb{E}\Delta\boldsymbol{\varepsilon} \tag{4.18}$$

which is equivalent to $\boldsymbol{\mathcal{D}}\Delta\boldsymbol{u} = \Delta\boldsymbol{\varepsilon}$, whenever $\Delta\boldsymbol{\varepsilon}$ is exactly compatible, and always has a unique solution (even for an incompatible $\Delta\boldsymbol{\varepsilon}$). In addition, the matrix of the system (4.18) is already available in decomposed form and the right-hand side is easily computed.

4.4 Steady-state solution categories

Two non-negative scalar measures of plastic action characterize a steady-state cycle.

$$P_a := \int_0^1 \int_{\mathcal{B}} \|\boldsymbol{d}^p\|\, d\mathbf{x}\, dt \tag{4.19}$$

$$P_b := \int_{\mathcal{B}} \| \left(\int_0^1 \boldsymbol{d}^p dt\right) \| d\mathbf{x} = \int_{\mathcal{B}} \|\Delta\boldsymbol{\varepsilon}\| d\mathbf{x} \tag{4.20}$$

Indeed:

1. P_a measures *plastic activity* for the steady-state cycle. This indicator assumes

null value for cycles where shakedown occurs. It is strictly positive in case of alternating plasticity or ratcheting.

2. P_b measures *plastic balance* for each steady cycle. It assumes non-zero value for ratcheting, since this term applies to cycles with non-null strain deformation per cycle, $\Delta\boldsymbol{\varepsilon}$.

If the solid is homogeneous and obeys the Mises model, the total dissipation equals $\sqrt{2/3}P_a\sigma_Y$, with σ_Y denoting the yield stress.

In view of (4.11), it always holds

$$P_a \geqslant P_b \tag{4.21}$$

The contribution of alternating plasticity is measured, using the per-cycle accumulated plastic strain, by the parameter defined as

$$p_{AP} := \frac{P_a - P_b}{P_a} \tag{4.22}$$

if $P_a > 0$, and 0 otherwise.

Table 4.1 summarizes the possible ranges for plastic activity and plastic balance and the corresponding stable cycle.

Table 4.1: Stable cycle characterization

Plastic activity	Plastic balance	Description
$P_a = 0$	$P_b = 0$	Shakedown
$P_a > 0$	$P_b = 0$	Alternating plasticity
$P_a > 0$	$P_b > 0$	Ratcheting

Ratcheting stabilized responses belong to two different sub-classes, explained in the following.

The first class is characterized by *simple ratcheting*, where the structure undergoes, at each point being not elastic during the entire steady cycle, a monotonous plastic strain increment in each steady cycle.

The second class is the *combination of simple ratcheting and alternating plasticity.*

These two modes of ratcheting are considered in Zouain (2018), where simple ratcheting is denoted *simple mechanism of incremental collapse (SMIC)* and the superposition of simple ratcheting and alternating plasticity is denoted *combined mechanism of incremental collapse (CMIC).*

Table 4.2 precisely classifies sub-modes of ratcheting in terms of relations between plastic action and plastic balance.

Table 4.2: Sub-classes of ratcheting

Plastic activity and balance	Description
$P_a > P_b > 0$	Mixed ratcheting and alternating plasticity
$P_a = P_b > 0$	Simple ratcheting

Concerning structural integrity, both classes of ratcheting may result in different types of macroscopic failures. When mixed with alternating plasticity, ratcheting has the potential to reduce the fatigue life, and/or accelerating crack nucleation and abbreviating propagation stages. Some pertinent remarks on this subject can be found in Hassan et al. (2008).

Figure 4.1 applies the above classification with some examples of steady-state responses. The figure considers a body composed by a material point submitted to four stress-strain regimes. The figure schematically shows only one of the components of the stress and strain, for each steady-state cycle.

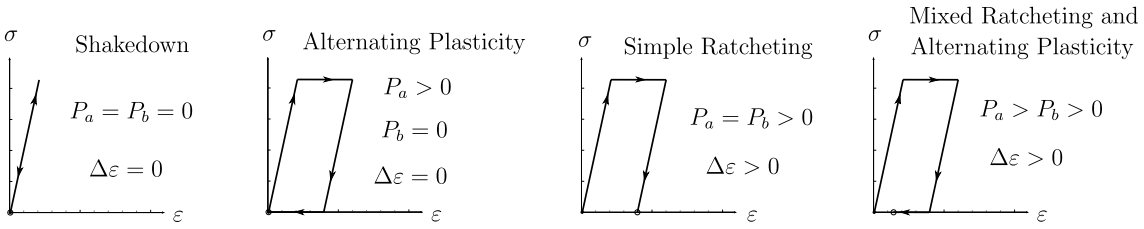

Figure 4.1: Steady-state classification for a material point under different regimes: (a) shakedown, (b) alternating plasticity, (c) simple ratcheting and (d) mixed ratcheting and alternating plasticity

4.5 The discretized equations of the steady state

A grid in the time interval $[0, 1]$ generates the discrete counterparts of the proposed continuum equations. The discretization of stress and displacement fields uses finite element interpolation. Here, the implementation adopts mixed finite elements presented by Zouain et al. (2014).

The discretization adopts the backward Euler approximation of the plastic flow law. Thus, the results of the direct approach exactly match a conventional incremental solution, when sufficiently stabilized.

The notation is explained in the following.

4.5.1 Spatial interpolation

The index (α, i) refers to a stress control point α in the i-th finite element. To simplify notation, the same symbols $\boldsymbol{u}$, $\boldsymbol{\sigma}$, $\boldsymbol{\varepsilon}$ and $\boldsymbol{d}$ denote also the usual FEM

column vectors. For instance, the approximation of plastic power is

$$\int_{\mathcal{B}} \boldsymbol{\sigma}(\mathbf{x}) \cdot \boldsymbol{d}^p(\mathbf{x})\, d\mathbf{x} \approx \boldsymbol{\sigma} \cdot \boldsymbol{d}^p = \sum_{\alpha,i} \boldsymbol{\sigma}^{\alpha,i} \cdot \boldsymbol{d}^{p,\alpha,i}. \tag{4.23}$$

The components of the finite dimensional vector $\boldsymbol{\sigma}$ are the values, at control points, of the approximated stress tensor. The discrete vectors $\boldsymbol{\varepsilon}$ and $\boldsymbol{d}^p$ are its energy-duals, which thus depend on the element area.

In the framework of a mixed stress-displacement method (Zouain et al., 2014), the interpolation is given, at each element $\mathcal{B}^i$, by the functions

$$\boldsymbol{u}(\mathbf{x})\big|_{\mathcal{B}^i} = \sum_{\beta} \boldsymbol{N}_u^{\beta}(\mathbf{x}) \boldsymbol{u}^{\beta,i} \qquad \boldsymbol{\sigma}(\mathbf{x})\big|_{\mathcal{B}^i} = \sum_{\alpha} \boldsymbol{N}_\sigma^{\alpha}(\mathbf{x}) \boldsymbol{\sigma}^{\alpha,i}, \tag{4.24}$$

where $\boldsymbol{u}^{\beta,i}$ and $\boldsymbol{\sigma}^{\alpha,i}$ are vectors of the interpolation parameters and $\boldsymbol{N}_{\boldsymbol{v}}^{\beta}$ and $\boldsymbol{N}_{\boldsymbol{\sigma}}^{\alpha}$ are the matrices of interpolation functions. The summation indexes α and β enumerate the basis functions for displacement and stress, respectively.

Substitution of (4.24) in the principle of virtual power leads to the following expression for the matrix of strain-displacemnt relation for element i

$$\boldsymbol{B}^{\alpha,i} := \sum_{\beta} \int_{\mathcal{B}} (\boldsymbol{N}_{\boldsymbol{\sigma}}^{\alpha})^T \boldsymbol{\mathcal{D}} \boldsymbol{N}_{\boldsymbol{v}}^{\beta}\, d\mathbf{x}. \tag{4.25}$$

Specific expressions for the mixed finite elements appear in Zouain et al. (2014).

The matrix $\boldsymbol{B}$ denotes the global discrete counterpart of the deformation operator $\boldsymbol{\mathcal{D}}$, as usual. Assembling the contribution of each element, given by (4.25), builds $\boldsymbol{B}$.

Consistent with the assumption that the deformation operator $\boldsymbol{\mathcal{D}}$ is non-singular, $\boldsymbol{B}$ is a full column rank matrix.

Then, the discrete kinematical compatibility and equilibrium relations reads

$$\boldsymbol{\varepsilon} = \boldsymbol{B}\boldsymbol{u} \qquad \boldsymbol{B}^T\boldsymbol{\sigma} = \boldsymbol{F}. \tag{4.26}$$

Similarly, from now on, the symbol $\mathbb{E}$ denotes the global discrete elastic operator obtained, for mixed finite elements, by assembling the matrices

$$\mathbb{E}^{\alpha,i} := \left[\sum_{\beta} \int_{\mathcal{B}} (\boldsymbol{N}_{\boldsymbol{\sigma}}^{\alpha})^T\, \hat{\mathbb{E}}^{-1} \boldsymbol{N}_{\boldsymbol{v}}^{\beta}\, d\mathbf{x} \right]^{-1}. \tag{4.27}$$

Accordingly, the definition of the discrete stiffness and the residual stress-plastic

strain matrices is

$$\boldsymbol{K} := \boldsymbol{B}^T \mathbb{E} \boldsymbol{B} \qquad \boldsymbol{Z} := \mathbb{E}\boldsymbol{B}\boldsymbol{K}^{-1}\boldsymbol{B}^T\mathbb{E} - \mathbb{E}. \tag{4.28}$$

Although the explicit presentation of the global matrices $\boldsymbol{B}$ and $\mathbb{E}$ giving the discrete strain-displacement and elastic relations is not common practice in the usual kinematical approach of incremental elastoplastic analysis, the asymptotic response algorithm proposed in this section is not essentially constrained to be used only with mixed finite elements interpolations. Indeed, it is possible to develop counterparts of (4.25), (4.27) and (4.28) in the framework of kinematical finite elements formulations. An example of this is the finite element $\boldsymbol{v}6$-UB (Zouain et al., 2014). Krabbenhøft et al. (2007b) offer a thorough discussion concerning this subject.

Furthermore, appendix B develops a conventional kinematic element ($\boldsymbol{v}6$) and builds the necessary matrices $\boldsymbol{B}$ and $\mathbb{E}$, allowing the implementation of the element with the direct methods present in this thesis.

The residual stress-plastic strain matrix $\boldsymbol{Z}$, which has important participation in the algorithm, could be effectively computed, once, in the preamble. However, this is a huge matrix for large size meshes, even using sparse storage. This was a drawback in the method for shakedown analysis proposed by Pycko (1997), already identified by that author. Instead of computing this matrix, the algorithm applies the same mapping by performing the sequence of operations in the definition of $\boldsymbol{Z}$ in (4.28). This is much more efficient in the use of memory and cpu time.

Consequently, to apply the influence operator $\boldsymbol{Z}$, the algorithm uses the fixed stiffness matrix $\boldsymbol{K}$, which is computed and decomposed once, initially.

4.5.2 Approximations in time

The time discretization renders N sub-intervals in the cycle interval $[t_0, t_N] = [0, 1]$. The discrete cyclic variables, defined at the time stations $j = 1 : N$ (the sequence from 1 to N), are

$$\boldsymbol{\varepsilon}^{p,j} := \boldsymbol{\varepsilon}^p(t_j) \qquad \boldsymbol{d}^{p,j} := \boldsymbol{d}^p(t_j) \qquad \boldsymbol{\sigma}^{r,j} := \boldsymbol{\sigma}^r(t_j) \qquad \boldsymbol{\sigma}^{E,j} := \boldsymbol{\sigma}^E(t_j). \tag{4.29}$$

With the implicit Euler approximation of the flow law, the backwards plastic strain increments are

$$\delta\boldsymbol{\varepsilon}^{p,j} := \boldsymbol{\varepsilon}^{p,j} - \boldsymbol{\varepsilon}^{p,(j-1)} = \int_{t_{j-1}}^{t_j} \boldsymbol{d}^p \, dt, \qquad j = 1 : N. \tag{4.30}$$

Consequently,

$$\Delta\boldsymbol{\varepsilon} = \int_0^1 \boldsymbol{d}^p \, dt = \sum_{j=1:N} \delta\boldsymbol{\varepsilon}^{p,j}. \tag{4.31}$$

Using the above definitions, integration of $\dot{\boldsymbol{\sigma}}^r = \boldsymbol{Z}\boldsymbol{d}^p$ leads to

$$\boldsymbol{\sigma}^{r,1} - \boldsymbol{\sigma}^{r,N} = \boldsymbol{Z}\delta\boldsymbol{\varepsilon}^{p,1} \tag{4.32}$$

$$\boldsymbol{\sigma}^{r,j} - \boldsymbol{\sigma}^{r,(j-1)} = \boldsymbol{Z}\delta\boldsymbol{\varepsilon}^{p,j} \qquad j = 2 : N. \tag{4.33}$$

4.5.3 Discrete formulation

In the asymptotic cyclic analysis, the discrete problem to be solved, based on (4.12-4.15), is stated as follows.

The discrete equations of the asymptotic response

Given $\boldsymbol{\sigma}^{E,j}$ for $j = 1 : N$, find $\boldsymbol{\sigma}^{r,j}$ and $\delta\boldsymbol{\varepsilon}^{p,j}$, for $j = 1 : N$, such that

$$\delta\boldsymbol{\varepsilon}^{p,j} \in N_P(\boldsymbol{\sigma}^{E,j} + \boldsymbol{\sigma}^{r,j}) \qquad j = 1 : N \tag{4.34}$$

$$\boldsymbol{\sigma}^{r,1} - \boldsymbol{\sigma}^{r,N} = \boldsymbol{Z}\delta\boldsymbol{\varepsilon}^{p,1} \tag{4.35}$$

$$\boldsymbol{\sigma}^{r,j} - \boldsymbol{\sigma}^{r,(j-1)} = \boldsymbol{Z}\delta\boldsymbol{\varepsilon}^{p,j} \qquad j = 2 : N \tag{4.36}$$

$$\boldsymbol{B}^T\boldsymbol{\sigma}^{r,N} = \boldsymbol{0} \tag{4.37}$$

with the subsidiary equations

$$\Delta\boldsymbol{\varepsilon} = \sum_{j=1:N} \delta\boldsymbol{\varepsilon}^{p,j} \qquad \Delta\boldsymbol{u} = \boldsymbol{K}^{-1}\boldsymbol{B}^T\mathbb{E}\Delta\boldsymbol{\varepsilon} \tag{4.38}$$

4.6 An algorithm for computing the steady state

This section includes an iterative algorithm to solve the elastoplastic steady-state problem, based on the formulation (4.34-4.37). The main idea of this method is to perform a fictitious sequence of cycles aiming to reduce the residuals of these equations. The procedure consists in a sequence of substitutions using the equalities (4.35) and (4.36) combined with return mapping operations with respect to the evolution relation (4.34).

The algorithm has two stages. Firstly, the basic update procedure, BU, at each time station. Secondly, the global procedure for computing the elastoplastic steady state, ESS, constituted of nested loops that apply the basic update.

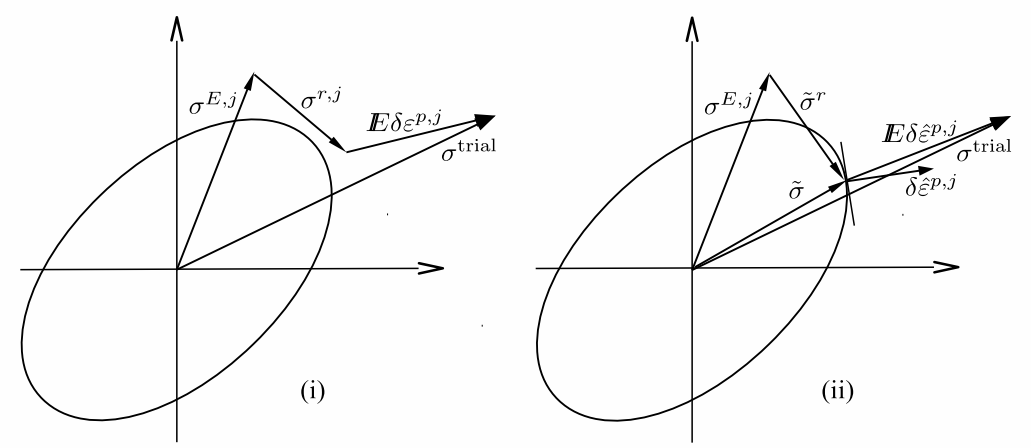

Figure 4.2: Projection procedure to obtain a new iterate $\delta\hat{\boldsymbol{\varepsilon}}^{p,j}$: (i) compute trial stress $\boldsymbol{\sigma}^{\text{trial}}$ and (ii) project $\boldsymbol{\sigma}^{\text{trial}}$ to find the update $\delta\hat{\boldsymbol{\varepsilon}}^{p,j}$.

4.6.1 Basic update (BU) at time station j

A pseudo-code defines the update procedure in sequel. Afterwards, remarks analyze and justify the method.

Procedure BU (at time station j)
Given the current global approximations, $\boldsymbol{\sigma}^{r,(j-1)}$, $\boldsymbol{\sigma}^{r,j}$ and $\delta\boldsymbol{\varepsilon}^{p,j}$, such that

$$\boldsymbol{\sigma}^{r,j} - \boldsymbol{\sigma}^{r,(j-1)} = \boldsymbol{Z}\delta\boldsymbol{\varepsilon}^{p,j} \qquad \boldsymbol{B}^T\boldsymbol{\sigma}^{r,j} = \mathbf{0} \qquad \boldsymbol{B}^T\boldsymbol{\sigma}^{r,(j-1)} = \mathbf{0} \tag{4.39}$$

compute the new iterate, $\hat{\boldsymbol{\sigma}}^{r,j}$ and $\delta\hat{\boldsymbol{\varepsilon}}^{p,j}$, as follows.

1. **for** all control points of the mesh

   Define (see Figure 4.2)

   $$\boldsymbol{\sigma}^{\text{trial}} := \boldsymbol{\sigma}^{E,j} + \boldsymbol{\sigma}^{r,j} + \mathbb{E}\delta\boldsymbol{\varepsilon}^{p,j} \tag{4.40}$$

   and find the new plastic strain approximation, $\delta\hat{\boldsymbol{\varepsilon}}^{p,j}$, such that

   $$\tilde{\boldsymbol{\sigma}} = \boldsymbol{\sigma}^{\text{trial}} - \mathbb{E}\delta\hat{\boldsymbol{\varepsilon}}^{p,j} \in P \tag{4.41}$$

   $$\delta\hat{\boldsymbol{\varepsilon}}^{p,j} \in N_P(\tilde{\boldsymbol{\sigma}}) \tag{4.42}$$

   end for

2. Compute new approximation of the residual stress

   $$\hat{\boldsymbol{\sigma}}^{r,j} = \boldsymbol{\sigma}^{r,(j-1)} + \boldsymbol{Z}\delta\hat{\boldsymbol{\varepsilon}}^{p,j} \tag{4.43}$$

end procedure BU

Algorithm 1: Basic Update

The following remarks serve to justify or analyze properties of this basic procedure.

1. The input, comprising $\boldsymbol{\sigma}^{r,(j-1)}$, $\boldsymbol{\sigma}^{r,j}$ and $\delta\boldsymbol{\varepsilon}^{p,j}$, fulfills the set of conditions (4.39). Moreover, the output values $\hat{\boldsymbol{\sigma}}^{r,j}$ and $\delta\hat{\boldsymbol{\varepsilon}}^{p,j}$ also satisfies the same set of conditions due to equation (4.43) and suitable initialization.

2. The projection procedure defined by (4.40), (4.41) and (4.42), sketched in figure 4.2, is formally identical to the return mapping (or closest point mapping) commonly utilized in incremental elastoplastic analysis. However, the trial stress is computed here from current iterates of the residual stress and the plastic strain increment, instead of using, as in standard incremental analysis, the time-step total strain increment.
   Consequently, the algorithm can perform this projection using all the common tools proposed and tested in a vast literature; see for instance Simo and Hughes (2006), de Souza Neto et al. (2008) and de Borst et al. (2012).

3. In the event that the input satisfies

$$\delta\boldsymbol{\varepsilon}^{p,j} \in N_P(\boldsymbol{\sigma}^{E,j} + \boldsymbol{\sigma}^{r,j}) \tag{4.44}$$

   the basic updating procedure replicates the input values at the output, that is $\hat{\boldsymbol{\sigma}}^{r,j} = \boldsymbol{\sigma}^{r,j}$ and $\delta\hat{\boldsymbol{\varepsilon}}^{p,j} = \delta\boldsymbol{\varepsilon}^{p,j}$. Hence, the heuristic equality (4.40) does not introduce any spurious constraint on the converged solution. In addition, it holds that a fixed point for the projection procedure (4.40-4.42) is necessarily comprised by a plastically admissible total stress $\boldsymbol{\sigma}^{E,j}+\boldsymbol{\sigma}^{r,j}$ and one associated plastic flow $\delta\boldsymbol{\varepsilon}^{p,j}$ (see definition (3.21)).

4.6.2 An algorithm for elastoplastic steady state

The proposed algorithm to compute the stabilized elastoplastic response consists of a sequence of fictitious time cycles, described in the following.

At each time step, labeled by $j \in 1:N$, it is performed a loop of applications of the basic update procedure BU. The loop ends when the difference between successive approximations of residual stress at one BU, $\int_{\mathcal{B}} \|\hat{\boldsymbol{\sigma}}^{r,j} - \boldsymbol{\sigma}^{r,j}\| d\mathbf{x}$, becomes less than a prescribed tolerance for the step, or when k exceeds $k_{\max}$.

At the end of each fictitious cycle, the total difference of residual stress $\sum_{j=1:N} \int_{\mathcal{B}} \|\boldsymbol{\sigma}^{r,j} - \boldsymbol{\sigma}^{r,j,\text{old}}\| d\mathbf{x}$ is checked for convergence. If a fixed point for the iterative algorithm is attained, then it solves the set of equations determining the asymptotic elastoplastic response.

The pseudo-code of the algorithm is given in the following.

Procedure ESS: Elastoplastic steady state

Compute iteratively $\boldsymbol{\sigma}^{r,j}$ and $\delta\boldsymbol{\varepsilon}^{p,j}$ as follows:

Initialize $\quad \text{icyc} = 0; \quad \boldsymbol{\sigma}^{r,j} = \mathbf{0}, \quad \delta\boldsymbol{\varepsilon}^{p,j} = \mathbf{0}, \quad j = 1 : N$
$\qquad\qquad\quad \text{Var}(\boldsymbol{\sigma}^r) = \text{big}; \quad \text{var}_j(\boldsymbol{\sigma}^{r,j}) = \text{big}, \quad j = 1 : N$

do while $\quad (\text{icyc} \leqslant \text{icyc}_{\max} \quad \textbf{and} \quad \text{Var}(\boldsymbol{\sigma}^r) \geqslant \text{tol}_{\text{cyc}})$

$\text{icyc} = \text{icyc} + 1$

for $j = 1 : N$

$k = 0$

$\boldsymbol{\sigma}^{r,j,\text{old}} = \boldsymbol{\sigma}^{r,j}$

do while $\quad \big(k \leqslant k_{\max} \quad \textbf{and} \quad \text{var}_j(\boldsymbol{\sigma}^{r,j}) \geqslant \text{tol}_{\text{step}}\big)$

$k = k + 1$

Use procedure BU to compute new approximations $\hat{\boldsymbol{\sigma}}^{r,j}$ and $\delta\hat{\boldsymbol{\varepsilon}}^{p,j}$

$\tau_j = \int_{\mathcal{B}} \|\hat{\boldsymbol{\sigma}}^{r,j}\| d\mathbf{x}$

$\xi_j = \int_{\mathcal{B}} \|\hat{\boldsymbol{\sigma}}^{r,j} - \boldsymbol{\sigma}^{r,j}\| d\mathbf{x}$

$\text{var}_j(\boldsymbol{\sigma}^{r,j}) = \xi_j / \max\{\tau_j, 1\}$

Update $\quad \boldsymbol{\sigma}^{r,j} = \hat{\boldsymbol{\sigma}}^{r,j}, \quad \delta\boldsymbol{\varepsilon}^{p,j} = \delta\hat{\boldsymbol{\varepsilon}}^{p,j}$

end do

end for

$\xi_j = \int_{\mathcal{B}} \|\boldsymbol{\sigma}^{r,j} - \boldsymbol{\sigma}^{r,j,\text{old}}\| d\mathbf{x}$

$\text{Var}(\boldsymbol{\sigma}^r) = (\sum_{1:N} \xi_j) \,/\, \max\{\sum_{1:N} \tau_j, 1\}$

end do

$\boldsymbol{\sigma}^j = \boldsymbol{\sigma}^{E,j} + \boldsymbol{\sigma}^{r,j}, \quad j = 1 : N$

Compute $\Delta\boldsymbol{\varepsilon}^p$ and $\Delta\boldsymbol{u}$ using (4.18)

$\Delta\boldsymbol{\varepsilon} = \sum_{j=1:N} \delta\boldsymbol{\varepsilon}^{p,j}$

$\Delta\boldsymbol{u} = \boldsymbol{K}^{-1}\boldsymbol{B}^T\mathbb{E}\Delta\boldsymbol{\varepsilon}$

end procedure ESS

Algorithm 2: Elastoplastic Steady State

This fictitious sequence of cycles qualifies as a direct method for the asymptotic problem mainly because the proposed trial stress

$$\boldsymbol{\sigma}^{\text{trial}} := \boldsymbol{\sigma}^{E,j} + \boldsymbol{\sigma}^{r,j} + \mathbb{E}\delta\boldsymbol{\varepsilon}^{p,j} \tag{4.40}$$

is computed from the ideally elastic stress and the current iterates of plastic strain increments and residual stress. On the other hand, in the standard elastoplastic

time-integration, the trial stress is

$$\boldsymbol{\sigma}^{\text{trial}} = \boldsymbol{\sigma}^{j-1} + \mathbb{E}\delta\boldsymbol{\varepsilon}^{j}, \tag{4.45}$$

with $\delta\boldsymbol{\varepsilon}^{j}$ calculated through

$$\delta\boldsymbol{\varepsilon}^{j} = \boldsymbol{B}\delta\boldsymbol{u}^{j} \qquad \delta\boldsymbol{u}^{j} = \hat{\boldsymbol{K}}^{-1}\delta\boldsymbol{F}^{j}. \tag{4.46}$$

where $\delta\boldsymbol{F}^{j}$ is the load step and $\hat{\boldsymbol{K}}$ the algorithmic consistent stiffness matrix, updated and decomposed at each time step.

So, another noticeable distinction between algorithm 2 and the standard time-integration in elastoplasticity is that the only global operations in ESS, (4.43), are always performed using a fixed decomposed stiffness matrix, differently from the usual computation and decomposition of the algorithmic tangent stiffness matrix.

The present procedure is implemented in Fortran; it uses the package Pardiso (Schenk and Gärtner, 2004) for solving sparse systems of linear equations.

4.7 Numerical examples

4.7.1 A tube under cyclic pressure and temperature

This section presents the application of the proposed procedure to compute the asymptotic cyclic response for a variation of the classical Bree's problem (Bree, 1967). Zouain and Silveira (2001) and Zouain (2018) used this model in shakedown analysis.

The model represents a long thick closed tube, with $R_{\text{ext}} = 1.25R_{\text{int}}$ (R_{ext} and R_{int} are external and internal radii of the tube).Figure 4.3 shows a sketch of the model.

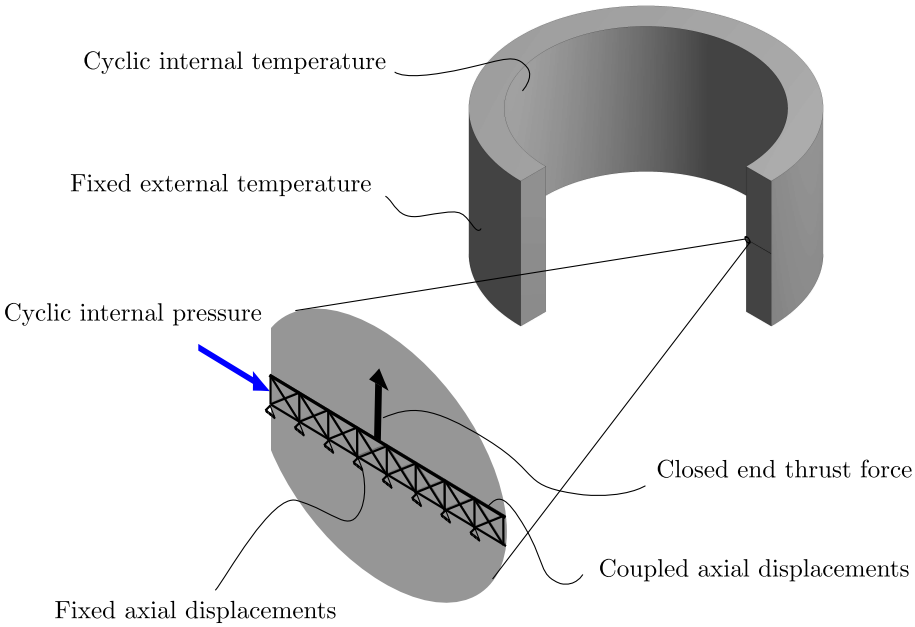

Figure 4.3: Closed tube under cyclic pressure and cyclic temperature profile.

The loading regime is cycle composed by four peaks of internal pressure p_{int} and temperature Θ_{int} (the external temperature is fixed at the reference temperature of the material). The imposed temperature fluctuation is quasi-static, thus producing a logarithmic decay through the wall thickness. The material is linear elastic-perfectly plastic, with constants E and ν, and obeys the Mises model with yield stress σ_Y. All material coefficients are independent of temperature. Since the tube is long, a boundary condition imposes that all cross sections remain plane during deformations.

A variable modification allows substitution of the radial coordinate R by the dimensionless coordinate r given below, together with the relevant geometric parameter ℓ.

$$r := \frac{R}{R_{\text{ext}}} \qquad \ell := \frac{R_{\text{ext}}}{R_{\text{int}}} \tag{4.47}$$

The following dimensionless pressure parameter applies

$$\hat{p} := \frac{p_{\text{int}}}{p_c} \qquad p_c = \frac{2}{\sqrt{3}} \sigma_Y \ln \ell \tag{4.48}$$

where p_c is the collapse pressure of the closed tube.

The temperature Θ at a distance r of the axis is

$$\Theta = \Theta_{\text{ext}} - (\Theta_{\text{int}} - \Theta_{\text{ext}}) \frac{\ln r}{\ln \ell} \tag{4.49}$$

Accordingly, the dimensionless thermal parameter is

$$\hat{q} := \frac{E c_\varepsilon \left(\Theta_{\text{int}} - \Theta_{\text{ext}}\right)}{2(1-\nu)\sigma_Y} \tag{4.50}$$

where E denotes the Young's modulus, ν is the Poisson's coefficient, and c_ε is the thermal expansion coefficient.

Gokhfeld and Charniavsky (1980) or Zouain (2018) include analytical expressions for the ideally elastic stresses produced by the above pressure and thermal loadings.

The class of cycles $\mathcal{C}$ used here to demonstrate the performance of the algorithm appears as rectangles in the $\hat{q}$ versus $\hat{p}$ plot of Figure 4.4, with vertices $(0,0)$, $(\underline{\hat{p}},0)$, $(\underline{\hat{p}},\underline{\hat{q}})$ and $(0,\underline{\hat{q}})$.

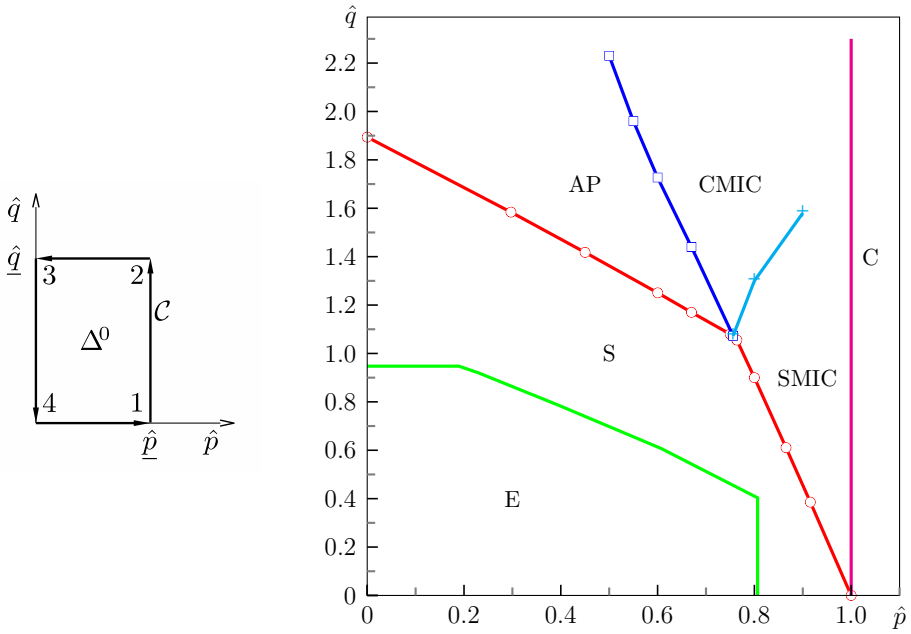

Figure 4.4: Interaction diagram for a closed tube, with $R_{\text{ext}} = 1.25 R_{\text{int}}$, under cycles $\mathcal{C}$ of internal pressure and logarithmic temperature. Label E identifies purely elastic response, S means (elastic) shakedown, AP is alternating plasticity, SMIC and CMIC are simple and combined mechanisms of incremental collapse, and C is plastic collapse.

Each one of these cycles $\mathcal{C}$ also defines a corresponding reference domain Δ^0 for the related shakedown analysis, which computes the maximally amplified domain $\mu\Delta^0$ among those that only contain loading programs (cyclic or not) leading to elastic accommodation. The plot of $\mu\underline{\hat{p}}$ versus $\mu\underline{\hat{q}}$ is shown in Figure 4.4b, marked by circles. This curve separates the safe region, S $\bigcup$ E, from the regions where *the class of cycles* $\mathcal{C}$ gives either plastic collapse (C), alternating plasticity (AP), simple mechanisms of incremental collapse (SMIC) or combined mechanism of incremental collapse (CMIC).

It is worth to emphasize that the region S $\bigcup$ E is safe for all kind of cycles embedded in each $\mu\Delta^0$ while the type of response obtained outside this region depends on the type of loading cycle considered, the class $\mathcal{C}$ in this study.

The following paragraphs describe the numerical experiments performed for this example. Data and results appear in terms of nondimensional quantities. All these tests assume $E = 1000\sigma_Y$ and $\nu = 0.3$.

The triangular finite elements used in this calculations are the axisymmetric versions of the mixed stress-displacement interpolations $\boldsymbol{\sigma}3$-$\boldsymbol{v}6$ and $\boldsymbol{S}3$-$\sigma_m 1$-$\boldsymbol{v}6$ defined in Zouain et al. (2014) for plane strain limit analysis. The mixed element named $\boldsymbol{\sigma}3$-$\boldsymbol{v}6$ assumes quadratic displacements (velocities in limit analysis), interpolated from six nodes in each triangle and being continuous between elements. The stresses are linear, interpolated from the three vertices of the triangle and discontinuous between elements. The element $\boldsymbol{S}3$-$\sigma_m 1$-$\boldsymbol{v}6$ uses the same displacement approximation, interpolates linearly and discontinuous the deviatoric stress components and constant and discontinuous the mean stress. Zouain et al. (2014) extensively tested these elements and compared to other finite elements for plane strain limit analysis.

The adopted mesh forms a rectangular strip, from the internal to the external surfaces of the tube, comprising 100 squares (in line radially), each one divided, by the square diagonals, into four equal triangles. It has 400 elements and 1003 nodes. Nodes at the strip bottom (with $z = 0$) are constrained in the axial direction and nodes at the strip top (with $z = (R_{\text{ext}} - R_{\text{int}})/100$) are constrained to move together in the axial direction; this results in 1605 dof.

The time discretization consists of $N = 32$ equal time intervals, with peaks reached at times $j = \{8;\ 16;\ 24;\ 32\}$.

The chosen control parameters of the algorithm are $\text{tol}_{\text{cyc}} = \text{tol}_{\text{step}} = 10^{-3}$ and $k_{\max} = 10$.

1. A preliminary task builds the Bree's interaction curve in Figure 4.4 by solving a sequence of classical shakedown problems. The circles in the figure represent these numerical results. The algorithm for shakedown analysis used is described in Zouain et al. (2002) and Zouain (2018). Additionally, this analysis precisely identifies the class of impending failure mechanism corresponding to each prescribed domain. The identification is alternating plasticity (AP) for the upper part of the shakedown limit and simple mechanism of incremental collapse (SMIC) for the lower part.

2. Each point computed by shakedown analysis (a circle in Figure 4.4) serve as a reference to validate the present numerical procedure for steady state response. Specifically, if $(\mu\underline{\hat{p}}, \mu\underline{\hat{q}})$ denotes one of these points, two asymptotic analyses were performed: (i) one for a loading cycle $\mathcal{C}$ determined by $(0.99\mu\underline{\hat{p}}, 0.99\mu\underline{\hat{q}})$

so as to obtain a purely elastic stabilized response, and (ii) the second one for loading cycle $\mathcal{C}$ determined by $(1.01\mu\underline{\hat{p}}, 1.01\mu\underline{\hat{q}})$ to obtain a cyclic (finite) mechanism of failure of the same kind predicted by the shakedown analysis.

The proposed asymptotic procedure ESS passed these tests.

3. The curve marked by squares in Figure 4.4 is the ratchet limit in this problem. It is the boundary of regions where the response to cycles $\mathcal{C}$ is alternating plasticity (AP) or combined mechanism of incremental collapse (CMIC). It was determined by direct tentative, using ESS, similar to the procedure of the previous item.

4. The boundary between SMIC and CMIC, marked by crosses, was obtained analogously. In this case, however, this curve could not be precisely identified because the component of alternating plasticity in the asymptotic cycle increases very slowly when we surpass this boundary, entering the CMIC region.

5. This item shows some numerical results and comparisons of the asymptotic response for the particular loading cycle $\bar{\mathcal{C}} := \{\underline{\hat{p}} = 0.8, \underline{\hat{q}} = 1.8\}$, a cycle producing CMIC according to the interaction diagram in Figure 4.4.

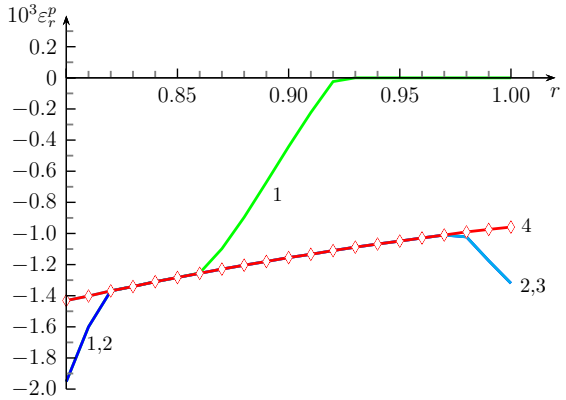

Figure 4.5: Per-cycle accumulated plastic radial strain versus radial coordinate. Asymptotic distributions at peaks 1, 2, 3 and 4 of cycle $\bar{\mathcal{C}}$.

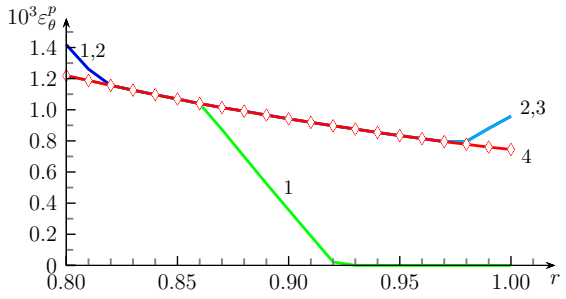

Figure 4.6: Per-cycle accumulated plastic circumferential strain vs radial coordinate. Asymptotic distributions at peaks 1, 2, 3 and 4 of cycle $\bar{\mathcal{C}}$.

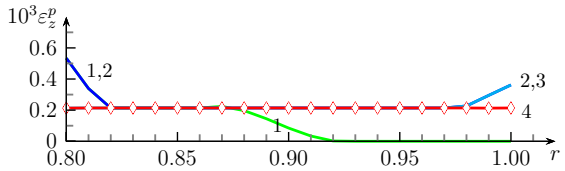

Figure 4.7: Per-cycle accumulated plastic axial strain versus radial coordinate. Asymptotic distributions at peaks 1, 2, 3 and 4 of cycle $\bar{\mathcal{C}}$.

Figures 4.5-4.7 display the asymptotic distributions, along the r-axis, of per-cycle accumulated plastic strain components ε_r^p, ε_θ^p and ε_z^p at peaks 1, 2, 3 and 4 of cycle $\bar{\mathcal{C}}$. The per-cycle increment of plastic strain components $\Delta\varepsilon_r^p$, $\Delta\varepsilon_\theta^p$ and $\Delta\varepsilon_z^p$, marked by diamonds, are not null; thus, the steady state is incremental collapse (IC).

The inner points of the tube, with $r < 0.82$, undergo positive circumferential plastic strain between peaks 0 and 1 (pressure increase) and negative circumferential plastic strain between peaks 2 and 3 (pressure decrease), characterizing *local alternating plasticity*. This completes the identification of a global combined mechanism of incremental collapse (CMIC). It is observed, in addition, that points with $r > 0.98$ also suffer direct and reverse circumferential plastic strain in each cycle.

There is also direct and reverse plastic strain increments in the r and z components, at the same internal and external cylindrical parts of the tube. Differently, points in the core region $0.82 < r < 0.98$ undergo only monotonic plastic strain evolution.

6. Now it is shown, for cycle $\bar{\mathcal{C}}$, a comparison of the results to a step-by-step solution obtained by running Ansys with the same mesh and time discretization. Figure 4.8 displays increments of plastic strain components given by both methods.

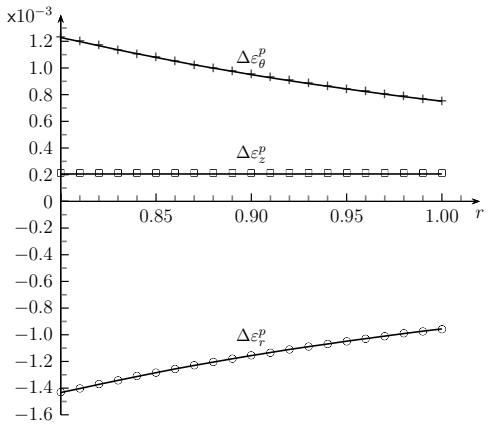

Figure 4.8: Increments of plastic strains for cycle $\bar{\mathcal{C}}$. Dots are present results and lines are stabilized incremental solutions with Ansys.

The plane183 second order displacement standard element of Ansys, and also the plane183 with mixed u-p formulation, were used in this comparison. The first stabilized cycle in the step-by-step response was detected, *a posteriori*, with a similar criterion than $\text{tol}_{\text{cyc}} = 10^{-3}$ used for stress convergence in the present algorithm.

The increments of plastic strain components, compared in Figure 4.8, show close agreement between the results of the present algorithm and those obtained by incremental analysis. The two adopted finite elements give solutions indistinguishable in the figure. Also the two variants of plane183, standard and u-p mixed, are coincident in the figure.

Table 4.3 displays the CPU time required for the proposed algorithm to solve this problem, compared to the time spent in the incremental analysis by Ansys. Both codes were running in the same computer (a laptop Intel i7 with 8GB RAM). For the incremental solution, it is only compared here the time spent up to the first stabilized cycle, although a normal run exceeds this time because of the lack of a stopping criterion for asymptotic convergence.

Table 4.3: Performance for the tube under cyclic loading $\bar{\mathcal{C}}$

	Direct		Incremental	
Finite element	$\boldsymbol{\sigma}$3-$\boldsymbol{v}$6	$\boldsymbol{S}$3-σ_m1-$\boldsymbol{v}$6	plane183	u-p
CPU elapsed time (sec)	4	4	450	8450
Cycles	19	19	6	7
Linear system solutions	1024	998	1019	2161
Total AP strain p_{AP}	6.2 %	6.2 %		

In summary, this example is solved by incremental analysis in more than 110

times the elapsed time in the present algorithm.

Table 6.1 also shows the percentage of plastic straining that corresponds to the alternating plasticity component of the asymptotic response, $p_{AP} = (P_a - P_b)/P_a$, given in the last row of the table.

4.7.2 Square plate with a central circular hole

This section considers a square plate of side length $2b$ with a central circular hole of radius $a = 0.2b$, shown in Figure 4.9. The plate is homogeneous, isotropic, linear elastic-ideally plastic, complying with von Mises criterion for a yield stress denoted σ_Y, and subjected to plane strain conditions. The material constants comply with the relations $E = 1000\sigma_Y$ and $\nu = 0.3$.

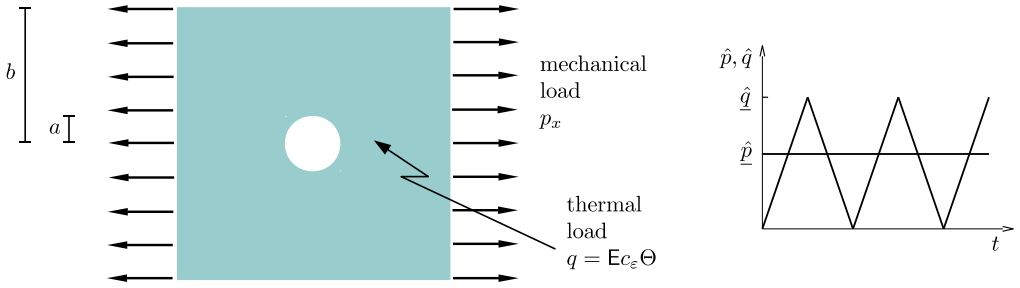

Figure 4.9: A perforated plate under thermo-mechanical cyclic loading.

Loadings consist of a constant uniform traction p_x and a fluctuating temperature Θ, assumed uniformly distributed in the plate at any instant. This cyclic loading is sketched in Figure 4.9 in terms of the nondimensional parameters $\hat{p} := p_x/\sigma_Y$ and $\hat{q} := q/\sigma_Y$, with $q := E c_\varepsilon \Theta$ (c_ε is the thermal expansion coefficient). The reference loading $\tilde{\mathcal{C}}$ for this example is defined by $(\underline{\hat{p}}, \underline{\hat{q}}) = (0.714, 1.428)$.

The unstructured mesh used has 11091 triangles, 22530 nodes and 44864 dof. It was adapted to better approximate the elastic stress solution under traction.

The model has triangular finite elements with mixed stress-displacement interpolations, $\boldsymbol{\sigma}3$-$\boldsymbol{v}6$ and $\boldsymbol{S}3$-$\sigma_m 1$-$\boldsymbol{v}6$ defined in Zouain et al. (2014) for limit analysis in plane strain. Between elements, displacements are continuous and stresses are discontinuous. They have quadratic interpolation of displacements and geometry in each triangle, associated to three nodes at vertices and three midside nodes. The element denoted $\boldsymbol{\sigma}3$-$\boldsymbol{v}6$ adopts linear interpolation for all stress components. In $\boldsymbol{S}3$-$\sigma_m 1$-$\boldsymbol{v}6$ deviatoric stress components are linear and the mean stress is piecewise constant.

In addition, solutions with a finite element, denoted $\boldsymbol{v}6$-UB, are included. This type of element is used by other authors for upper bound limit analysis; see for instance Makrodimopoulos and Martin (2007). The element $\boldsymbol{v}6$-UB, also described

and compared in Zouain et al. (2014), only assumes the quadratic interpolation of displacements but deviates from the standard quadratic kinematical finite element in order to guarantee rigourous upper bounds in plane strain or plane stress limit analysis. In particular, the formulation of this element substitutes the plastic dissipation function by a majorant function.

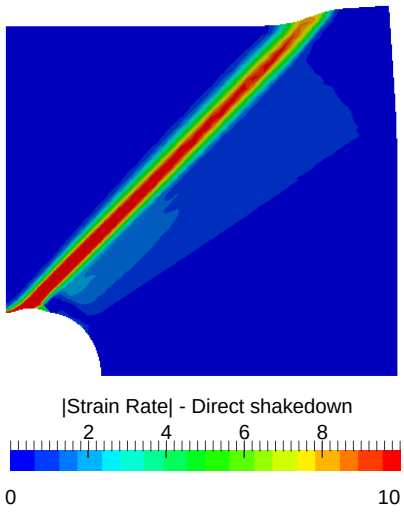

Figure 4.10: Strain rate modulus contour obtained by shakedown analysis of the perforated plate under the cyclic loading $\tilde{\mathcal{C}}$. The deformed configuration shown corresponds to small displacements proportional to the critical velocities.

Firstly, it is presented a shakedown analysis for the reference cycle $\tilde{\mathcal{C}}$. It consists in finding the maximal amplifying factor μ under the constraint that the cycle $\mu\tilde{\mathcal{C}}$ produces elastic shakedown as steady state. Using the procedure of Zouain et al. (2014), with element $\boldsymbol{\sigma}3$-$\boldsymbol{v}6$, we obtain $\mu = 0.9504$ and $(\mu\underline{\hat{p}}, \mu\underline{\hat{q}}) = (0.6786, 1.3572)$. This procedure gives the field of compatible strain rate depicted in Figure 4.10 and identifies this impending failure mechanism as combined incremental collapse. Limit analysis, with the same mesh and finite element, gives the plastic collapse traction $\hat{p}_C = 0.9237$.

Secondly, we computed the asymptotic response for cycle $\tilde{\mathcal{C}}$, obtaining the increment of displacements and strains depicted in Figure 4.11.a. Our results are validated by comparison with the incremental solution, performed by Ansys with the quadratic element PLANE183 (displacement formulation), shown in Figure 4.11b.

There are three rigid blocks embedded in the deformed plate of Figure 4.11: the first block moves down along the vertical axis, the second one moves to the right horizontally and the third one rotates counterclockwise with center in the upper right corner. The computed increment of displacement, divided by $10^{-4}a$, for the vertical block movement is -1.661 (-1.699 and -1.699) in the direct solution, with element $\boldsymbol{v}6$-UB (resp. $\boldsymbol{\sigma}3$-$\boldsymbol{v}6$ and $\boldsymbol{S}3$-$\sigma_m 1$-$\boldsymbol{v}6$), and -1.666 in the incremental solution. For

the horizontal displacement increment, the analogous values are 1.857 (1.909 and 1.906) in the direct solution and 1.868 in the incremental one.

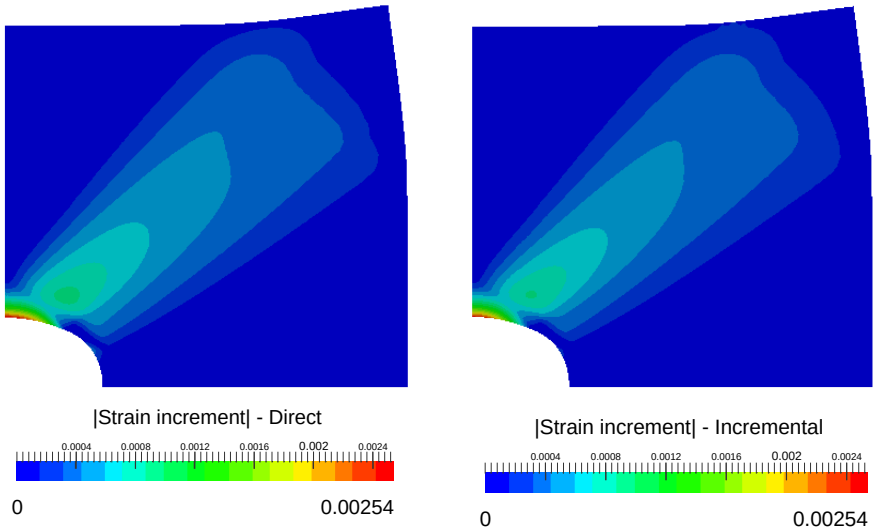

Figure 4.11: Per cycle increment of displacement and strain (modulus contour) for the perforated plate under loading $\tilde{\mathcal{C}}$. A comparison between direct and incremental numerical solutions.

Table 4.4 shows the performance of the direct and incremental procedures to compute the asymptotic response, in terms of elapsed cpu time. This comparison is important to justify the proposed direct method, intended to be faster than the integration along the load history. In this case, the direct procedure is remarkably faster.

The comparison in Table 4.4 was designed to be as fair as possible. Both programs were running the same mesh in the same computer (Intel i7 with 8GB RAM). Time expended in output operations of Ansys were eliminated from the cpu time reported in the table.

The difference in processing times may be partially explained by the fact that in the present approach the stiffness matrix is decomposed only once in the preamble of the iterative procedure.

The time integration was considered stabilized in 52 cycles, according to a criterion similar to the one in the present algorithm, which is a relative variation lower than 10^{-3} of the vector collecting all stress components in one cycle. The number of fictitious cycles of our algorithm are reported in Table 4.4.

Table 4.4 includes the percentage of plastic strains, $p_{AP} = 23.4\,\%$ (see (4.22)), corresponding to alternating plasticity, which indicates that the response is a combined mechanism of incremental collapse.

Table 4.4: Performance for the perforated plate under cyclic loading $\tilde{\mathcal{C}}$

	Direct			Incremental
Finite element	$\boldsymbol{v}$6-UB	$\boldsymbol{\sigma}$3-$\boldsymbol{v}$6	$\boldsymbol{S}$3-σ_m1-$\boldsymbol{v}$6	plane183
CPU elapsed time (sec)	45	58	62	10801
Cycles	68	70	56	52
Linear system solutions	531	544	431	912
Total AP strain p_{AP}	23.5 %	23.4 %	23.4 %	

Chapter 5

Ratchet-Limit Identification

The contents of the present chapter follows SantAnna and Zouain (2018). The project achieved all the topics included in the initial proposal for this thesis.

5.1 Computing the ratchet limit

This section introduces the main procedure proposed here to identify the ratchet boundary. In a diagram of loading parameters, this boundary contains all points that represent load cycles producing the impending phenomenon of ratcheting.

Accordingly, Algorithm 3 computes these critically amplified cycles, sequentially, one at a time.

The first task, in the following, is to define the mathematical conditions that precisely identify a critical loading cycle.

Conceptual description

Null plastic balance ($P_b = 0$) during the steady state defines cyclic programs inside the ratchet boundary. Differently, loading cycles beyond the ratchet-limit result in positive net plastic straining ($P_b > 0$).

The central idea of the method is to search for the most intense loading program amplification generating null net plastic balance ($P_b = 0$).

With this goal, the procedure solves the problem for modified loads inside and outside the boundary, which produce nested intervals $[\eta_{\text{inf}}, \eta_{\text{sup}}]$ bracketing the ratchet load factor η_R.

The procedure minimizes the size of the search intervals by applying the secant method, or modified *regula falsi* operations, until convergence.

5.2 The definition of a critical cyclic loading

The loading is decomposed in two prescribed sets of basic systems, represented by $\{\boldsymbol{\sigma}^E_{a,i},\ i = 1:n_a\}$ and $\{\boldsymbol{\sigma}^E_{f,i},\ i = 1:n_f\}$, in order to determine the class of cycles considered in the search of the ratchet limit. Loadings in the first set are amplified by a factor η, while loadings in the second set are not.

Accordingly, the following loading cycles are considered

$$\boldsymbol{\sigma}^E(t) = \eta\boldsymbol{\sigma}^E_a(t) + \boldsymbol{\sigma}^E_f(t) \qquad t \in (0,1) \tag{5.1}$$

where

$$\boldsymbol{\sigma}^E_a(t) = \sum_{i=1:n_a} c_{a,i}(t)\boldsymbol{\sigma}^E_{a,i} \qquad c_{a,i}(0) = c_{a,i}(1) \tag{5.2}$$

$$\boldsymbol{\sigma}^E_f(t) = \sum_{i=1:n_f} c_{f,i}(t)\boldsymbol{\sigma}^E_{f,i} \qquad c_{f,i}(0) = c_{f,i}(1) \tag{5.3}$$

The scalar functions $c_{a,i}(t)$ and $c_{f,i}(t)$ are prescribed in the outset.

Each cycle is denoted by

$$\mathcal{C}(\eta) = \{\eta\boldsymbol{\sigma}^E_a(t) + \boldsymbol{\sigma}^E_f(t),\ t \in (0,1)\} \tag{5.4}$$

The reference loading cycle is $\mathcal{C}(1) = \{\boldsymbol{\sigma}^E_a(t) + \boldsymbol{\sigma}^E_f(t),\ t \in (0,1)\}$.

The procedure searches for a critical value η_R such that $\mathcal{C}(\eta_R)$ is a cycle of impending ratcheting, in the following sense:

1. For any $\eta > \eta_R$, the cycle $\mathcal{C}(\eta)$ produces ratcheting.

2. For any $\eta < \eta_R$, the cycle $\mathcal{C}(\eta)$ produces a steady state that is either elastic or alternating plasticity.

When there are only two basic loadings (i.e. $n_a + n_f = 2$), it is possible to draw the cycles $\mathcal{C}(\eta)$ in a parametric plane. The arbitrary loading program and the rectangles in Fig. 2.1 are examples.

The classification of the basic loads as amplified and non-amplified is important to model properly the structure and the phenomenon of ratcheting. However, it is frequently found that different choices of amplified loading essentially describe the same situation and thus give rise to identical interaction diagrams.

It is worth noting that this approach does not introduce any constraint on this amplified/non-amplified classification.

According to the above definitions, given a reference cyclic load program $\mathcal{C}(1)$, the ratchet boundary lies where the loading amplification factor η causes an impending

net plastic balance P_b at the end of each steady-state cycle. That is

$$\eta_R = \max \{\eta^* \ \mid \ P_b(\mathcal{C}(\eta^*)) = 0\} \tag{5.5}$$

However, the solution for an asymptotic response adopts the procedure ESS, which terminates with small residuals in the equations and small errors in the computed solutions. This avoids strict null values for plastic balance, P_b, for cycles inside the non-ratchet region but near the ratchet boundary. This effect is always present (close to the ratchet limit) when the non-ratchet response is alternating plasticity. In turn, when (proper) ratcheting takes place, even for slightly greater amplifications above the boundary, the plastic balance P_b grows orders of magnitude above such residuals, clearly indicating the ratchet limit.

In view of the above remark, we choose a prescribed tolerance, tol_{P_b}, and state the numerical version of (5.5) as

$$\eta_R^{\text{app}} = \max \{\eta^* \ \mid \ P_b(\mathcal{C}(\eta^*)) \leqslant \text{tol}_{P_b}\} \tag{5.6}$$

Formulation (5.6) constitutes the core of the boundary identification procedure, Algorithm 3.

The indication of the boundary by (5.6) is clear in cases where the transition from alternating plasticity to ratcheting is sharp, as in most of our examples. However, it becomes sensitive to the tolerance tol_{P_b} when such transition is smooth. Remarkably, these cases are challenging not only for the present method but also (even worst) for incremental strategies. In such scenario, the analyst can use the specification of an allowable ratchet strain $\Delta\boldsymbol{\varepsilon}_a$, accumulated during the structure life, as some design codes already define. Indeed, recalling that P_b is the volume integral of per-cycle ratchet strain, the allowable ratcheting strain $\Delta\boldsymbol{\varepsilon}_a$ supports the use of the plastic balance tolerance $\text{tol}_{Pb} = \Delta\boldsymbol{\varepsilon}_a V/N$, where N is the structure life (in cycles) and V is the volume of the structure.

Procedure RL: Ratchet limit identification

Given the reference loading cycle $\mathcal{C}(1)$ and a factor η^* such that $P_b(\mathcal{C}(\eta^*)) > \mathrm{tol}_{P_b}$.

Compute η_R for $\mathcal{C}(\eta_R)$ at the ratchet limit:

Initialize: Set

$$j = 0 \qquad \eta^0_{\mathrm{inf}} = 0$$
$$k = 0 \qquad \eta^0_{\mathrm{sup}} = \eta^* + \delta\eta$$
$$k = 1 \qquad \eta^1_{\mathrm{sup}} = \eta^*$$

Use procedure ESS to compute

$$P^0_{b,\mathrm{sup}} = P_b(\mathcal{C}(\eta^0_{\mathrm{sup}})) \qquad P^1_{b,\mathrm{sup}} = P_b(\mathcal{C}(\eta^1_{\mathrm{sup}}))$$

do while $(\eta^k_{\mathrm{sup}} - \eta^j_{\mathrm{inf}} \geqslant \mathrm{tol}_\eta)$

(a) Update η_{new} by the secant method (Fig. 5.1):

$$\beta = \frac{\eta^{k-1}_{\mathrm{sup}} - \eta^k_{\mathrm{sup}}}{P^{k-1}_{b,\mathrm{sup}} - P^k_{b,\mathrm{sup}}} \qquad \eta_{\mathrm{new}} = \eta^k_{\mathrm{sup}} - \beta P^k_{b,\mathrm{sup}}$$

if $\eta_{\mathrm{new}} \notin]\eta^j_{\mathrm{inf}}, \eta^k_{\mathrm{sup}}[$ **then**

Change η_{new} applying *regula falsi* (Figure 5.2):

$$\alpha = \frac{\mathrm{tol}_{P_b}}{P^k_{b,\mathrm{sup}}} \qquad \eta_{\mathrm{new}} = \alpha\eta^k_{\mathrm{sup}} + (1-\alpha)\eta^j_{\mathrm{inf}}$$

end if

(b) Use procedure ESS to compute

$$P_{b,\mathrm{new}} = P_b(\mathcal{C}(\eta_{\mathrm{new}}))$$

Update the search interval $[\eta^j_{\mathrm{inf}}, \eta^k_{\mathrm{sup}}]$ using η_{new}

if $P_{b,\mathrm{new}} > \mathrm{tol}_{P_b}$ **then**

$k := k+1 \qquad \eta^k_{\mathrm{sup}} = \eta_{\mathrm{new}} \qquad P^k_{b,\mathrm{sup}} = P_{b,\mathrm{new}}$

else

$j := j+1 \qquad \eta^j_{\mathrm{inf}} = \eta_{\mathrm{new}}$

end if

end do

$\eta_R = \eta^j_{\mathrm{inf}}$

end procedure RL

Algorithm 3: Ratchet limit identification

The procedure RL adopts the secant method supplemented with *regula falsi* operations to minimize the interval $[\eta^j_{\mathrm{inf}}, \eta^k_{\mathrm{sup}}]$ that brackets the solution η_R, after j (respectively k) modifications of the left end (right end) of the initial interval.

The graph of the plastic balance in Fig. 5.1 is convex. Thus, when the proce-

dure starts above the ratchet limit, the secant iterations will estimate successive upper bounds η^k_{sup} $(k = 1, 2, 3...)$ of the ratchet limit. However, as the estimates converge to the solution η_R, the numerical errors in the computation of the plastic balance $P_b(\mathcal{C}(\eta^k_{\text{sup}}))$ and $P_b(\mathcal{C}(\eta^{k-1}_{\text{sup}}))$ may modify the secant angle, thus breaking this tendency.

Therefore, when the numerical errors become significant, the secant operation may deliver new lower bound estimates η^j_{inf} $(j = 0, 1, 2...)$ or even useless values outside the current bracketing interval. To avoid the latter event, the algorithm tests if the new estimate η_{new} falls outside the current interval $]\eta^j_{\text{inf}}, \eta^k_{\text{sup}}[$. If it does, a modified *regula falsi* iteration (Fig. 5.2) on the equation

$$P_b(\mathcal{C}(\eta)) - \text{tol}_{P_b} = 0 \tag{5.7}$$

substitutes the secant operation to assure convergence for the sequence of nested intervals.

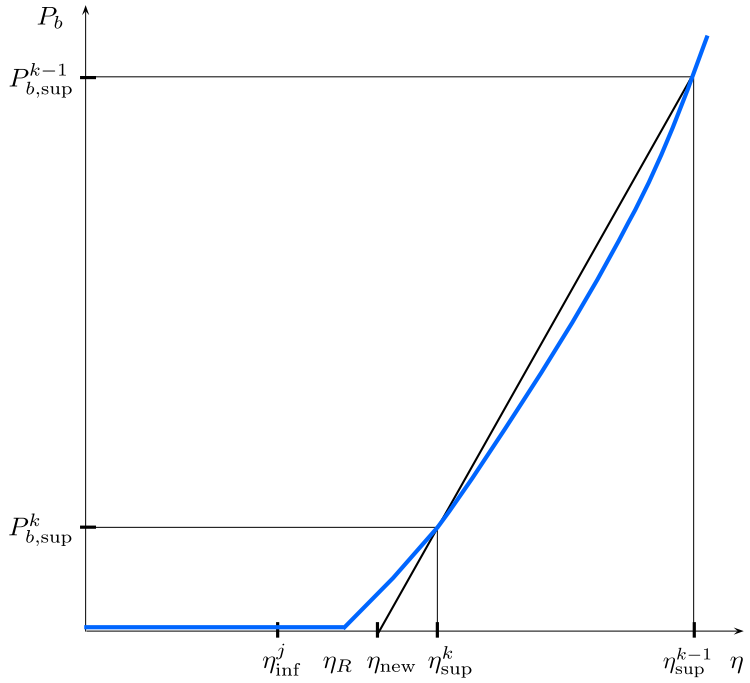

Figure 5.1: Update of η using the secant method.

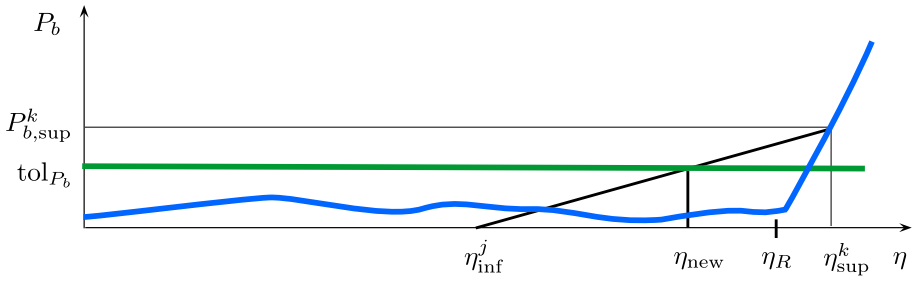

Figure 5.2: Modified update of η using *regula falsi*.

The plastic balance of the new steady-state cycle $P_b(\mathcal{C}(\eta_{\text{new}}))$ is the driver of the search interval update given in item (b) of Algorithm 3. It defines whether η_{new} replaces the lower bound η^j_{inf} or the upper bound η^k_{sup}; the end points of the search interval.

5.3 Implementation

The boundary identification method works as a new driver routine in a Fortran finite element software developed for research including a direct asymptotic solution module. This structure allows control of the development process and provides space for performance enhancements.

Besides, this procedure uses the same basic operations that any commercial finite element software does. Therefore, the same method may be implemented in any commercial finite element software with aid of user programmable functions.

5.4 Numerical examples

Each of the examples in this section has objectives with increasing levels of complexity.

The first example compares the method results with the analytical solution of the benchmark Bree's problem. The second includes more complex loading condition with cyclic non-proportional loading.

A third example assesses the Bree model under proportional loading. In this condition, an edge of the ratchet boundary is coincident with the plastic collapse limit, thus adding a numerical challenge.

In sequence, a non-conventional case appears embodying a tridimensional loading program.

In the next example, the algorithm solves a constrained block under cyclic thermal and mechanical loads. Again, cyclic non-proportional loading takes place. This

problem is the first multi-axial stress state problem analyzed here, adding another increment of complexity.

The next problem is a closed thick tube under cyclic thermal loading and variable internal pressure. The cyclic temperature profile is logarithmic following the solution of a thermal conduction problem. Therefore, it constitutes a multi-axial stress state with non-linear spatial distribution. A direct shakedown numerical solution serves for comparison, where the ratchet boundary is coincident with the SD limit. In the complementary part, step-by-step incremental computation performs the reference solution duty.

The last case represents an industrial application. A printed circuit heat exchanger model using a unit cell under plane strain, constant hot fluid pressure and representative temperature field. The results are verified against direct shakedown limits and incremental step-by-step solutions.

Unless declared in contrary, all examples adopt the following values for the elastic modulus, Poisson ratio and thermal expansion coefficient: $E = 1000\sigma_Y$, $\nu = 0.3$ and $c_{\boldsymbol{\varepsilon}} = 10^{-3}\ ^{\circ}C^{-1}$, respectively. Likewise, the initial step is set to $\delta\eta = 10^{-3} \cdot \eta^*$.

5.4.1 Classic Bree: fixed primary and cyclic secondary loads

The first numerical example is the standard Bree problem (Bree, 1967) about a bar under constant primary traction and cyclic thermal bending. The bar has cross-section area A and the material has yield stress σ_Y.

The reference cycle $\mathcal{C}(1)$ consists of an axial load $\boldsymbol{\sigma}_a^E = \sigma_Y$ superposed with a cyclic bending load $\boldsymbol{\sigma}_f^E(t)$ determined by imposed fluctuating temperature. At any instant, the temperature is linear across the bar and equal for all cross sections. The temperature of the top of the bar, Θ_1, is the reference (ambient) temperature and the temperature at the bottom varies cyclically from Θ_1 to a maximum denoted Θ_2. Then, the thermal stress cycle is described in terms of the nondimensional stress parameter

$$Q = \frac{Ec_{\boldsymbol{\varepsilon}}(\Theta_2 - \Theta_1)}{2\sigma_Y} \tag{5.8}$$

Fig. 5.3 contains a sketch of loads and prescribed boundary conditions.

The model uses plane stress interpolations on triangles, with quadratic displacements (Zouain et al., 2014). The mesh in Fig. 5.3 has 400 triangular elements and 1003 nodes, which form a strip orthogonal to the bar, comprising 100 squares divided into four triangles.

Fig. 5.3 depicts a traditional Bree interaction diagram for the usual mechanical and thermal parameters. To draw each point of this curve, the procedure sets one value of Q, solve for η_R and then plot the point $(P, Q) = (\eta_R, Q)$. Note that $p = \eta_R\sigma_Y$ is the constant traction force in the critical cycle computed by the search algorithm

RL.

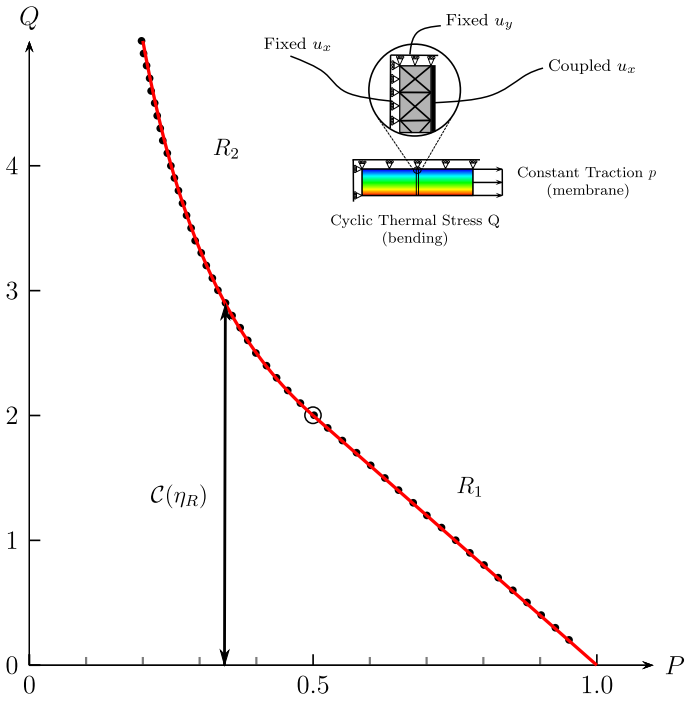

Figure 5.3: Ratchet boundary for the classic Bree problem: analytical results plotted in red and direct results in black dots. The small circle marks the transition between regions: R_1, of simple ratcheting, and R_2, of combined ratcheting.

The red curve in Fig. 5.3 is the analytic solution (Bree, 1967), whereas the fifty black dots compose the present direct solution. Errors are negligible in this example and this serves as an initial test of the method and its implementation.

In Fig. 5.3, R_1 and R_2 identify, respectively, the regions where simple or combined incremental collapse (ratcheting) is the steady-state response. This classification is obtained here by comparing, according to Table 4.2, the values P_a and P_b computed for an amplified cycle $\mathcal{C}(\eta)$ with η slightly greater than η_R.

5.4.2 Modified Bree: cyclic out-of-phase primary and secondary loads

In this example the loading program is modified with respect to the previous model. Now, primary and secondary loads vary following a non-proportional path as shown by the oriented rectangle in Fig. 5.4.

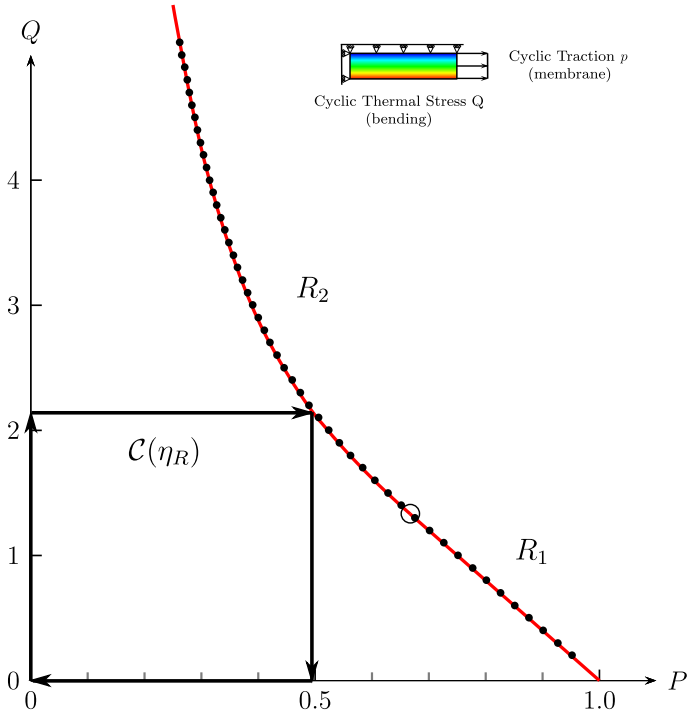

Figure 5.4: Ratchet boundary for the modified Bree problem, with out-of-phase cyclic primary and secondary stresses. Analytic results plotted in red and direct results in black dots. The small circle marks the transition between regions: R_1, of simple ratcheting, and R_2, of combined ratcheting.

Again, the direct numerical solution precisely fits the analytical solution given by Bradford (2017).

5.4.3 Modified Bree: cyclic in-phase primary and secondary loads

This example constitutes another loading modification of the basic Bree problem, concerning a proportional cyclic loading program. Fig. 5.5 shows the mechanical model and one critical cycle, $\mathcal{C}(\eta_R)$, of the class considered here.

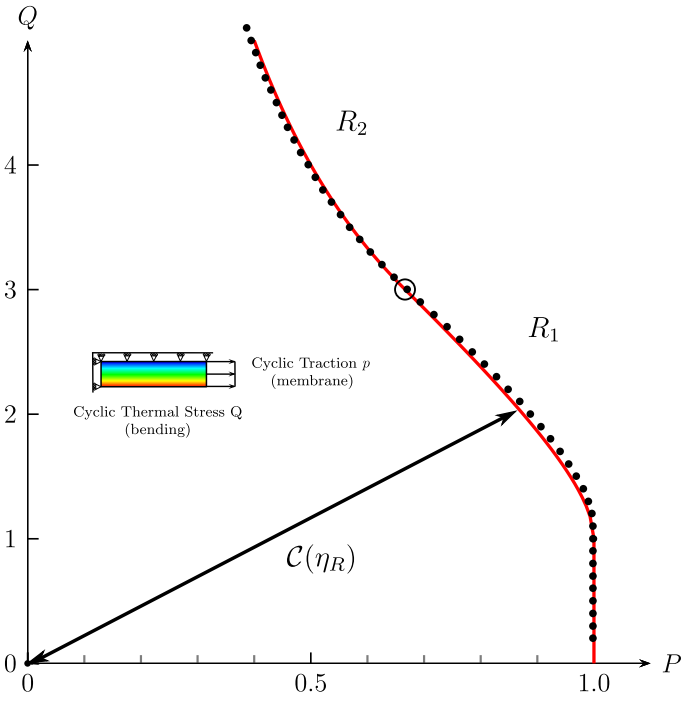

Figure 5.5: Ratchet boundary for a modified Bree problem, with in-phase cyclic primary and secondary stresses. Analytic solution plotted in red and present direct results in black dots.

Fig. 5.5 depicts the direct solution and the analytic solution by Bradford (2012). Since the numerical method applies spatial and time discretizations, small differences between analytical and numerical solutions occur. Clearly, the direct procedure passes this test too.

5.4.4 Bree 3D: two independent primary loads

A modification in loadings of the original Bree problem (Section 5.4.1) produces an example with a tridimensional load space. Now, two superposed loading functions $\bar{P}_1(t)$ and $\bar{P}_2(t)$ form a time dependent load $\bar{P}(t)$.

The loading $\bar{P}_1(t)$ is constant, with amplitude P_1 whereas $\bar{P}_2(t)$ is cyclic with amplitude P_2 and null mean value. The graph in Fig. 5.6a defines the functions $\bar{P}_1$, $\bar{P}_2(t)$ and $\bar{Q}(t)$. As in the original problem, the secondary load $\bar{Q}(t)$ is the nondimensional thermal stress and has range Q, defined through equation (5.8).

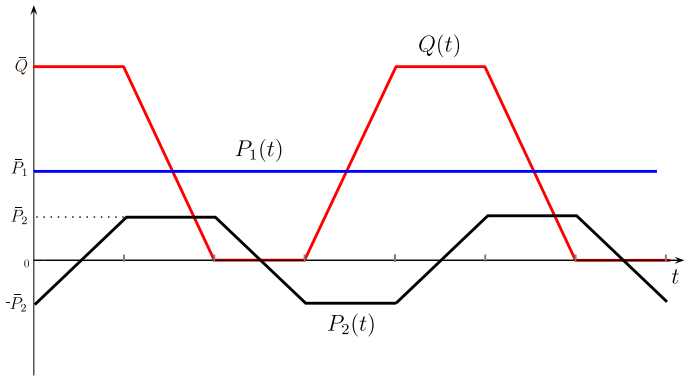

(a) Basic loads $\bar{P}_1(t)$, $\bar{P}_2(t)$ and $\bar{Q}(t)$

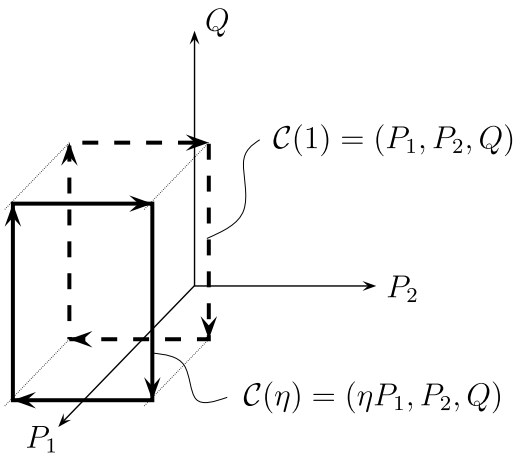

(b) Loading space: the reference cycle $\mathcal{C}(1)$ and the amplified cycle $\mathcal{C}(\eta)$

Figure 5.6: Loads - Definition and amplification

The reference cycle $\mathcal{C}(1)$ in Figure 5.6b is a representation, in the tridimensional space, of the loads specified in Fig. 5.6a. The amplified cycle $\mathcal{C}(\eta)$ is obtained with a factor η amplifying P_1.

Adopting this choice of amplification, the present method determines the ratchet-limit points marked with crosses in Fig. 5.7. A surface fitting these points appears in the same figure with a rainbow gradient.

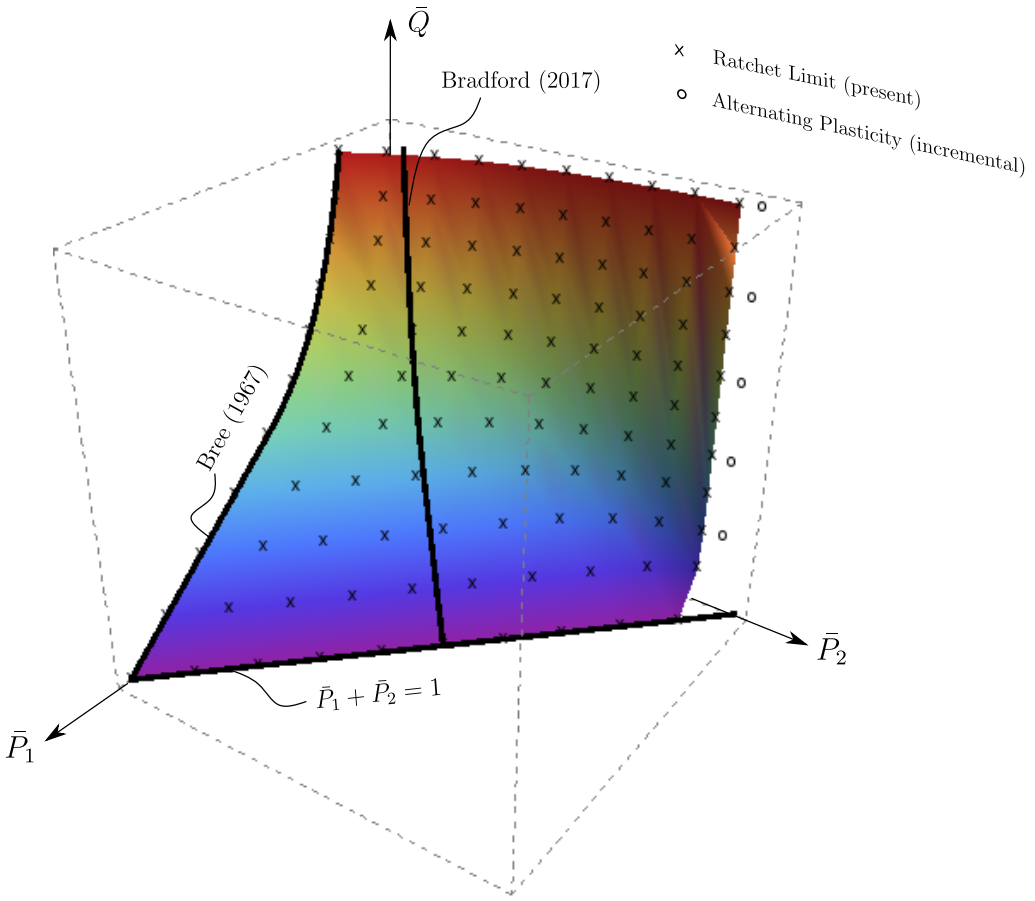

Figure 5.7: Ratchet limit surface in the load parameter space for cyclic thermal loading and two independent mechanical loadings (constant and cyclic).

To verify the results, it is compared with three analytical solutions (Bradford, 2017; Bree, 1967) and a set of five incremental step-by-step calculations.

The analytical curves in Fig. 5.7 are: (i) the Bree solution presented in Section 5.4.1, which excludes the variable mechanical load, that is, for $\bar{P}_2 = 0$, (ii) the solution given by Bradford (2017), when $\bar{P}_2 = \bar{P}_1$, and (iii) the plastic collapse plane $\bar{P}_1 + \bar{P}_2 = 1$.

Fig. 5.7 shows that the surface of present results matches all three analytical curves.

In addition, step-by-step calculations are performed with Ansys at five points. The chosen positions are inside the ratchet boundary, at the plane $P_1 = 0$. In all points, marked with non-filled dots at the plane $P_1 = 0$, the stabilized solution is alternating plasticity, meaning a non-ratcheting condition, as expected.

Comparisons between the analytical solutions and step-by-step calculations show that the proposed method is capable of generating solutions for multidimensional load spaces. Moreover, there are no restrictions when choosing constant (in time) loads, or cyclic loads, as either amplified or non-amplified loadings.

5.4.5 A block, in plane strain, under out-of-phase traction and temperature

This subsection deals with another benchmark problem: a block constrained to plane strain deformation and submitted to cyclic temperature (uniform at any instant) superposed to cyclic out-of-phase uniaxial traction.

The loading nondimensional parameters P and Q are now defined as

$$P = \frac{p}{\sigma_Y} \qquad Q = \frac{Ec_\varepsilon \Theta}{\sigma_Y} \tag{5.9}$$

where p is the applied traction and Θ is the difference between the block temperature and the reference temperature.

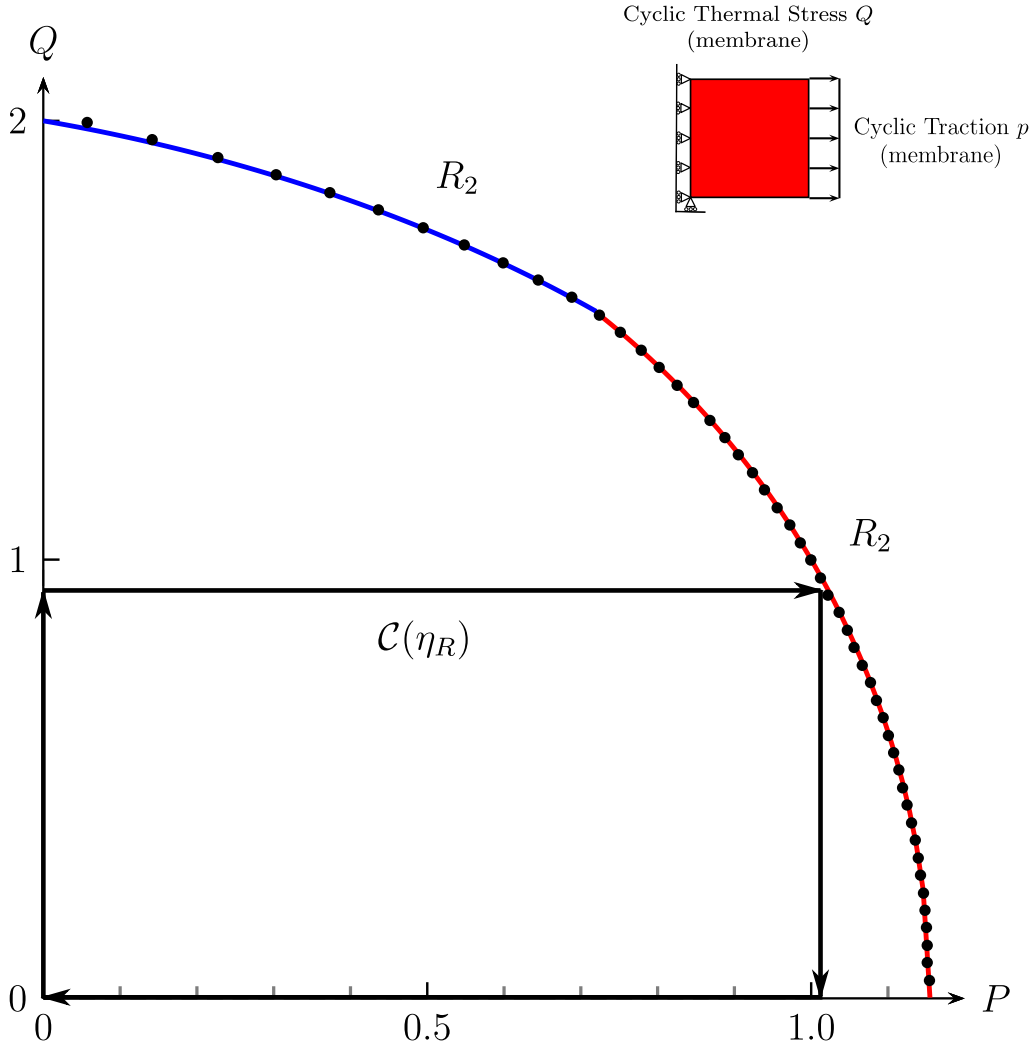

Figure 5.8: Ratchet boundary for the plane strain block under uniaxial traction and uniform temperature.

The shakedown analysis of this block is solved in closed form in Zouain (2018, p. 34) serving as a reference solution. Then, for consistency, the Poisson ratio is

$\nu = 0.2$ in this case.

It is known, in advance, that in this example the shakedown and ratcheting solutions coincide because incremental collapse is the critical mechanism defining the whole boundary of the shakedown domain in the analytical solution.

The exact shakedown boundary depicted in Fig. 5.8 has two parts, marked in red and blue, corresponding to two different kinds of impending combined ratcheting; see details in (Zouain, 2018, p. 34). The black dots in Fig. 5.8 compose the numerical solution obtained with the method devised in this article. A close agreement between both solutions occur.

5.4.6 Closed tube under internal pressure and logarithmic temperature

The pioneer Bree problem (Section 5.4.1) originates from simplifications applied to the modeling of a thin tube under constant internal pressure and cyclic through-thickness temperature profile.

The model used in this section (Zouain, 2018, p. 37) disregards many simplifications usually adopted in the literature. Indeed, it considers a closed thick tube under cyclic temperature obeying a logarithmic trough-thickness profile (quasi-static thermal conduction solution) and cyclic internal pressure.

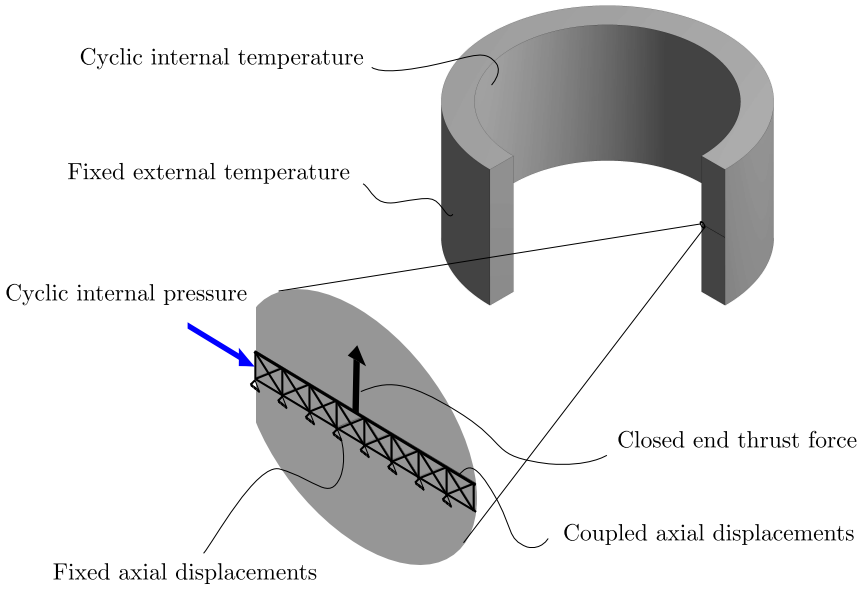

Figure 5.9: Closed thick tube: axisymmetric elements mesh, loads and boundary conditions.

Figure 5.9 depicts the axisymmetric finite element mesh. The model has null axial displacements at the bottom edge and coupled axial displacements at the top. A strip with 400 second order triangular elements and 1003 nodes forms the mesh.

The problem has pressure cycles out-of-phase with internal temperature, following the rectangular path shown in Fig. 5.10.

The nondimensional pressure load P is the ratio of internal pressure p and plastic collapse pressure p_c, that is

$$P = \frac{p}{p_c} \qquad p_c = \frac{2}{\sqrt{3}}\sigma_Y \ln \ell \qquad \ell = \frac{R_{\text{ext}}}{R_{\text{int}}} \tag{5.10}$$

where R_{int} and R_{ext} are the internal and external radii, respectively.

The through-thickness temperature profile is

$$\Theta(r) = \Theta_{ext} - (\Theta_{int} - \Theta_{ext})\frac{\ln r}{\ln \ell} \qquad r = \frac{R}{R_{\text{ext}}} \tag{5.11}$$

where Θ_{int} is the internal temperature, while Θ_{ext} is the external and reference temperature, and $c_{\boldsymbol{\varepsilon}}$ is the thermal expansion coefficient.

The nondimensional thermal parameter is

$$Q = \frac{E c_{\boldsymbol{\varepsilon}} (\Theta_{int} - \Theta_{ext})}{2(1-\nu)\sigma_Y} \tag{5.12}$$

Exact and numerical shakedown solutions for the same cylinder and conditions are shown in (Zouain, 2018, p. 37), for a ratio $\ell = 1.25$. This serves as reference solution where the shakedown and ratchet boundaries coincide. In the complementary part, step-by-step integrations (Incremental results), performed with Ansys, give the reference bounds bracketing the ratchet limit.

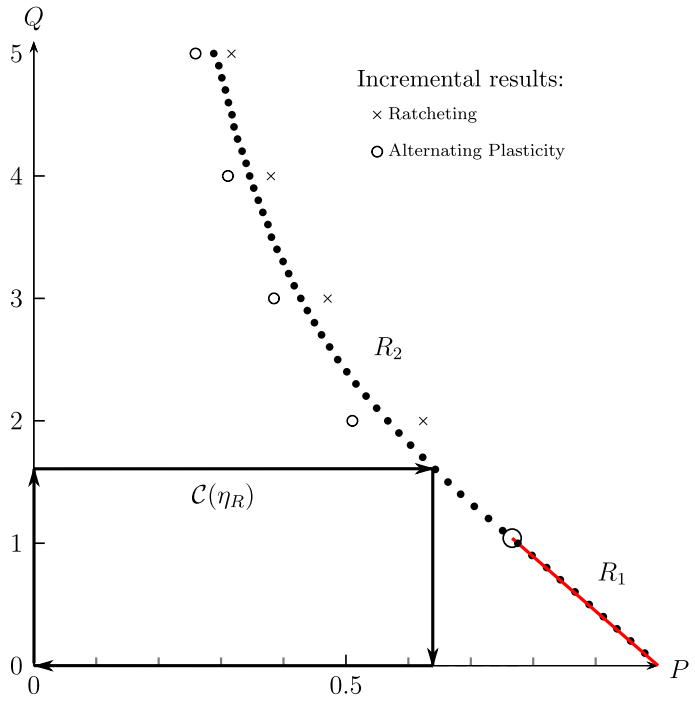

Figure 5.10: Ratchet boundary for the thick tube ($\ell = 1.25$) under internal pressure and logarithmic temperature.

The present solution, shown by full dots in Fig. 5.10, matches the numerical shakedown reference solution, shown by the red curve, where ratcheting and shakedown boundary coincide. For the complementary part, the ratchet boundary is consistent with the incremental results generated with Ansys.

5.4.7 Printed circuit heat exchanger

Fig. 5.11 presents a printed circuit heat exchanger (PCHE) . Using diffusion bonded plates; this type of equipment is compact and designed to operate in high-pressure systems. Applications include offshore oil production platforms (gas compression modules) and the expansion to nuclear industry is achievable.

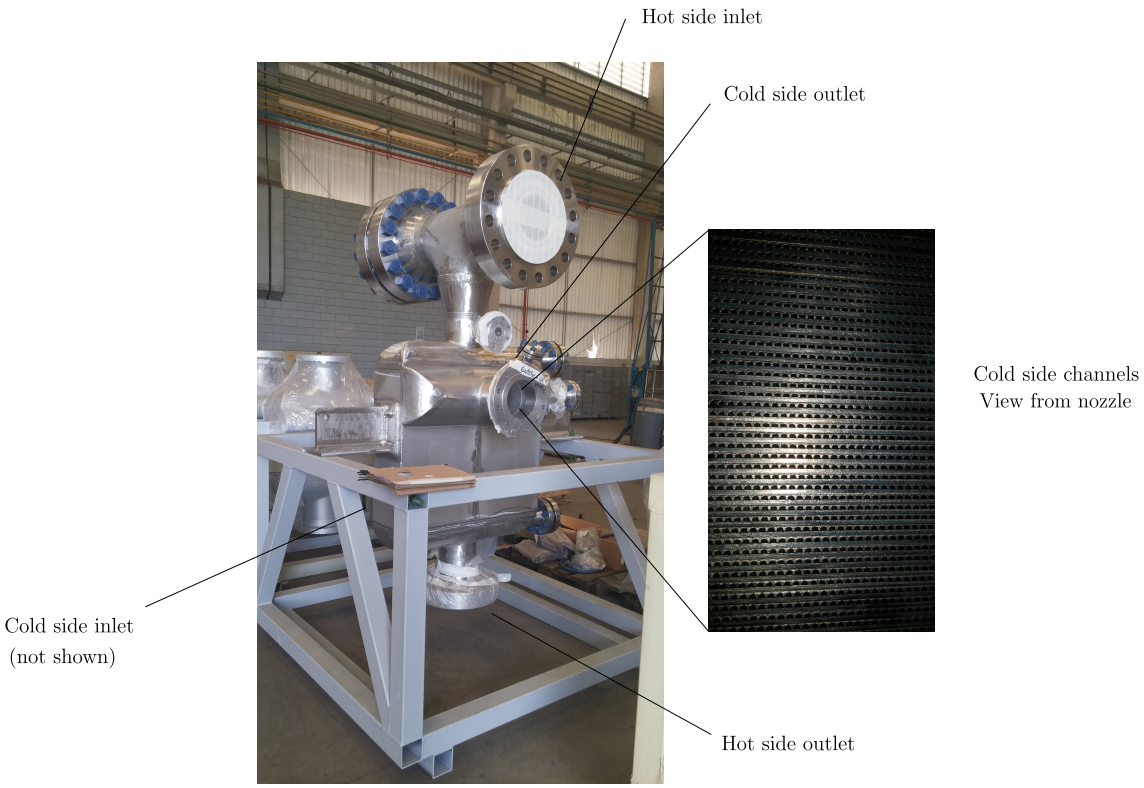

Figure 5.11: Printed circuit heat exchanger.

An unitary cell model of a PCHE appears in fig. 5.12. The cell dimensions are the same reported in Natesan et al. (2009, 2006). To avoid a singularity in the elastic solution, the model includes a corner radius of 0.042 mm at the basis of both semi-circular channels.

The model has coupled normal displacements at the left and top boundaries. Whereas, the right and bottom edges have null normal displacements to represent symmetry. Moreover, plane strain is assumed, making a conservative model, as noted by Lee and Lee (2014).

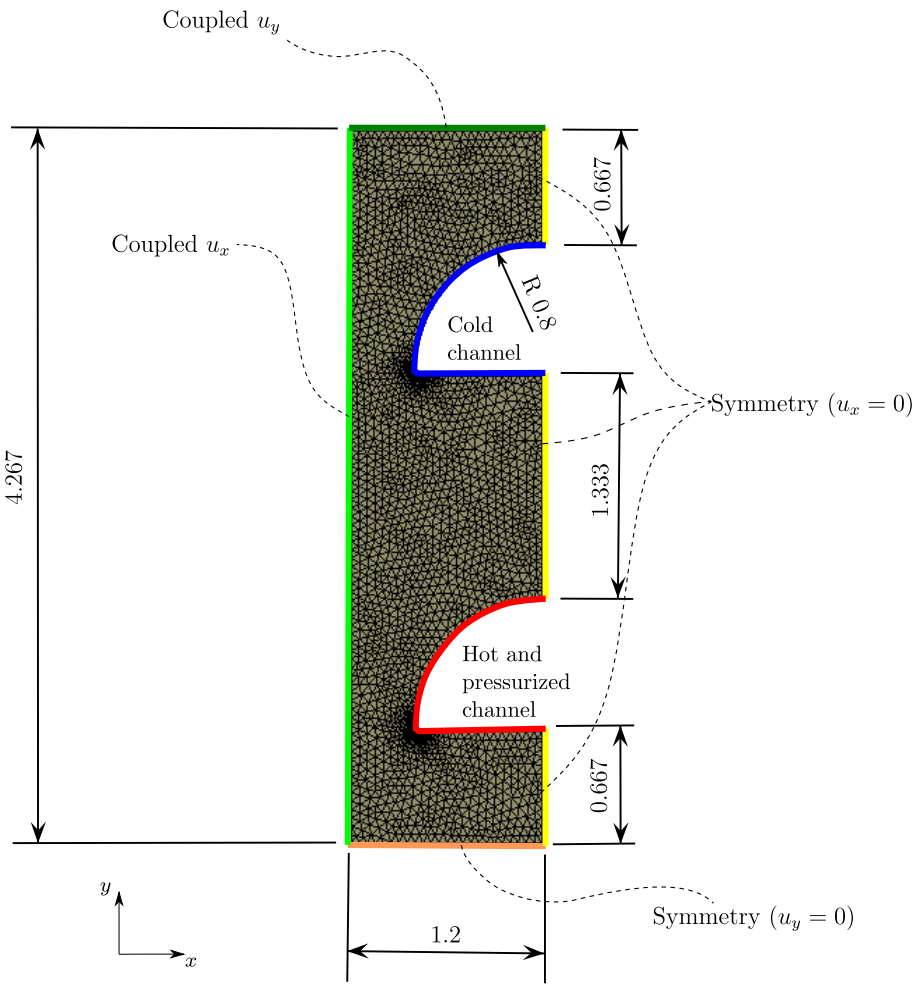

Figure 5.12: Unitary cell model for a printed circuit heat exchanger. Dimensions in millimeters.

The mesh has 12857 nodes building 6206 triangular elements. The type of the finite elements is second order with mixed stress-displacement formulation (Zouain et al., 2014).

The primary loading is internal pressure p applied at the hot channel.

The secondary loading corresponds to a simplified thermal analysis with prescribed temperatures Θ_h and Θ_c at the hot and cold channel walls, respectively. The temperature is coupled between top and bottom edges of the cell. There is no thermal flux at both lateral boundaries.

The primary and secondary parameters are

$$P = \frac{p}{\sigma_Y} \qquad Q = \frac{E c_\varepsilon (\Theta_h - \Theta_c)}{\sigma_Y}. \tag{5.13}$$

Pressure is sustained, whereas thermal loading is cyclic, as shown by the loading program in Fig. 5.13. The thermal expansion coefficient is $c_\varepsilon = 1.2 \cdot 10^{-5}\ ^\circ C^{-1}$.

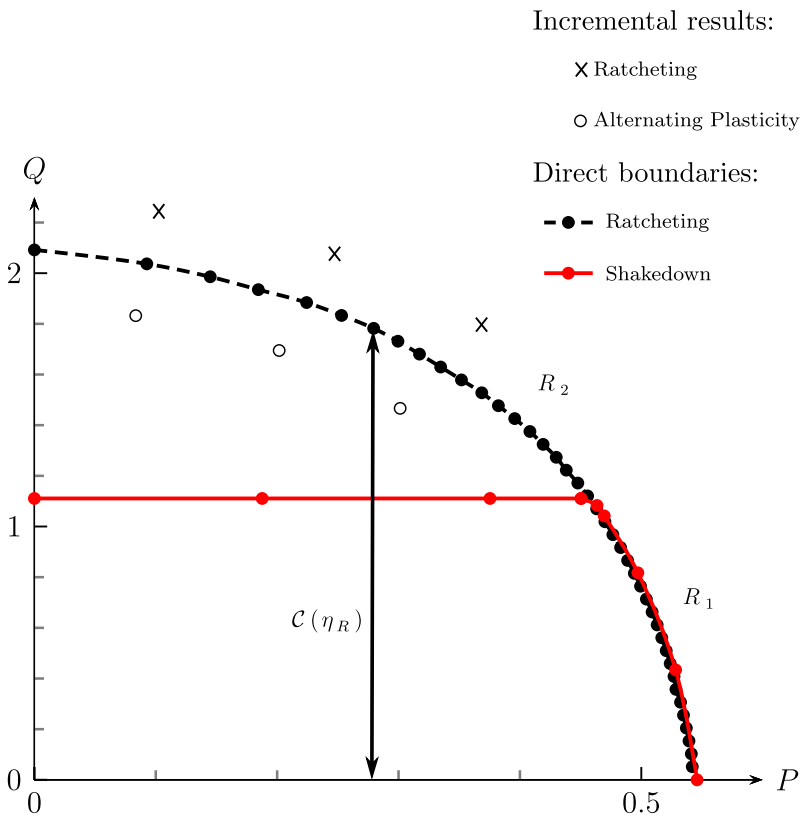

Figure 5.13: Ratcheting and shakedown boundaries for the PCHE plane strain model.

Fig. 5.13 depicts the ratchet boundary produced by the present algorithm. As a reference solution, the shakedown limits obtained with the direct method developed by Zouain et al. (2002) appear as the red curve in the same figure.

Shakedown and ratchet-search direct methods agree, in Fig. 5.13, where the shakedown limit is determined by an impending ratchet mechanism.

When alternating plasticity defines the shakedown boundary (upper plateau), incremental analysis generate the bounds to compare with the present solution. The step-by-step solutions, made in Ansys, are devised to bracket the transition of steady-state responses from alternating plasticity to ratcheting. In agreement with the direct solution, ratcheting is active for points outside the boundary. Furthermore, alternating plasticity manifested, in incremental analyses, for points lying between the ratcheting and shakedown limits.

The position of points representing incremental analyses in Fig. 5.13 was defined to allow clear identification of the steady-state response. When these points are closer to the ratchet boundary, the incremental solution requires higher numbers of cycles to stabilize increasing the uncertainty to identify the ratchet-limit. Each one of the 6 points in Fig. 5.13 has a predefined set up of 20 cycles. The total computation took 260 minutes of cpu, which gives the entry 43.3 minutes per point in Table 5.1.

On the other hand, the direct procedure required a mean time of 4.76 minutes per point. According to Procedure RL (Algoritm 3), each of these points corresponds to a series of direct steady-state solutions, by Procedure ESS (Algorithm 2), automated to identify the boundary. In the present case, a mean value of 9 steady-state solutions was necessary to reach a ratchet-limit point. That gives a mean time of 0.53 minutes for each steady-state cyclic solution.

Table 5.1: Mean time to compute a solution, in minutes

Solution type	Direct Shakedown	Present method	Incremental
Steady-state cycle	–	0.53	43.3
Ratchet-boundary point	5.01	4.76	–

From the viewpoint of efficiency in the steady-state solution, the direct procedures perform, in this example, 81.7 times faster than the incremental solution.

Regarding efficiency in the overall process of identifying one amplification of loads at impending ratcheting, there are many comparisons to consider. Note that the report in this example has only two step-by-step computations bracketing each point of the target curve; this is obviously not an actual process of identification. Nevertheless, the time spent in these two computations, 86.6 minutes, is a lower bound for any incremental search and it is 18 times the cpu time, 4.76 minutes, taken by the proposed algorithm.

A final comparison can be made in Table 5.1 for points where the shakedown and ratchet boundaries coincide: the mean time of 4.76 minutes is of same order than 5.01 minutes, which corresponds to a direct shakedown solution computed by the optimization algorithm proposed by Zouain et al. (2002).

Figure 5.14 shows a close agreement between direct and incremental solutions for $\|\Delta \boldsymbol{u}\|$, in a point with $(P, Q) = (0.368, 1.793)$. It is remarkable that both solutions differ not only by the solution strategy, but also by the finite element formulation. While the present method adopts a stress-displacement formulation, the incremental solution adopts the kinematical formulation.

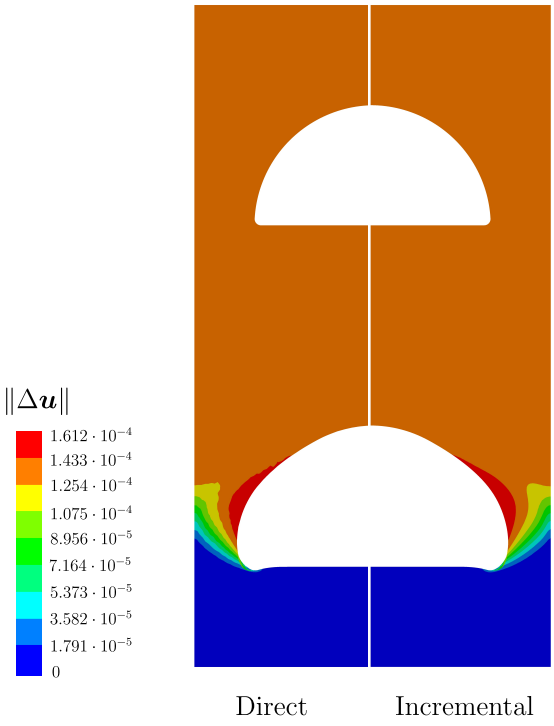

Figure 5.14: Norm of the displacement increment $\|\Delta \boldsymbol{u}\|$ per-cycle, using direct and incremental methods. Deformed shape amplified by 1000.

Figure 5.15 shows the norm of the ratchet strain $\|\Delta \boldsymbol{\varepsilon}\|$ with both solutions strategies. Indeed, the figure turns evident the ratcheting at the border of the hot channel.

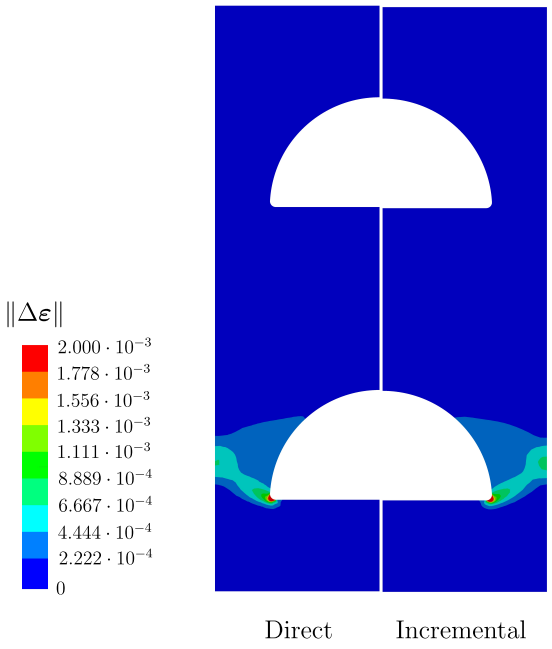

Figure 5.15: Norm of the ratchet strain $\|\Delta\boldsymbol{\varepsilon}\|$, using direct and incremental methods.

5.4.8 Specified tolerances and time discretization

Table 5.2 describes the mean time per ratchet-limit point (MTP) performed by the present procedure, for all the numerical examples. The same table includes the prescribed tolerances tol_η and tol_{Pb}, the adopted number of time steps N for backward Euler integration and the number of vertexes n_v that compose the loading cycle $\mathcal{C}(\eta)$.

Table 5.2: Tolerances, time steps and mean time per ratchet-limit point (MTP).

Example	tol_{Pb}	$\text{tol}\eta$	N	n_v	MTP(s)
Classic Bree	$1.0 \cdot 10^{-7}$	$1.0 \cdot 10^{-4}$	32	2	10.1
Bree out-of-phase	$1.0 \cdot 10^{-7}$	$1.0 \cdot 10^{-4}$	64	4	13.6
Bree in-phase	$1.0 \cdot 10^{-6}$	$1.0 \cdot 10^{-4}$	32	2	11.7
Bree 3D	$1.0 \cdot 10^{-7}$	$1.0 \cdot 10^{-4}$	64	4	11.9
Plane strain block	$1.0 \cdot 10^{-6}$	$1.0 \cdot 10^{-4}$	64	4	3.3
Closed Tube	$1.0 \cdot 10^{-7}$	$1.0 \cdot 10^{-4}$	64	4	19.9
PCHE	$1.0 \cdot 10^{-6}$	$1.0 \cdot 10^{-3}$	32	2	285.6

N is the number of integration steps and n_v the number of vertexes of the path $\mathcal{C}(\eta)$.

In addition, $\text{tol}_{\text{cyc}} = \text{tol}_{\text{step}} = 1.0 \cdot 10^{-3}$ and $k_{\max} = 10$ were set at ESS procedure, for all examples. Table 5.3 shows the mean number of iterations for a ratchet-limit

point identification. It also includes the mean number of secant and regula-falsi iterations.

Table 5.3: Mean iterations per ratchet-limit point.

Example	total	secant	regula
Classic Bree	10	6	4
Bree out-of-phase	10	6	4
Bree in-phase	11	6	5
Bree 3D	10	6	4
Plane strain block	11	7	4
Closed Tube	8	6	2
PCHE	9	6	3

Table 5.4 summarizes the difference between present method and analytical, closed form, reference solutions. The ratio e^i is the relative difference between a ratchet-limit factor η_R^i determined by present method and the reference solution η_{ref}^i. Considering a ratchet-limit curve, composed by n points, $\bar{e}$ measures the mean relative difference between present and reference curves. In addition, s measures the standard deviation of e^i.

$$\bar{e} = \frac{1}{n}\sum_{i=1}^{n} e^i \qquad e_i = \frac{\eta_R^i - \eta_{ref}^i}{\eta_{ref}^i} \tag{5.14}$$

$$s = \sqrt{\frac{\sum_{i=1}^{n}(e^i - \bar{e})^2}{n-1}} \tag{5.15}$$

Table 5.4: Numerical precision measures.

Example	$\bar{e}$ (%)	s (%)
Classic Bree	−0.12	0.48
Bree in-phase	0.08	0.99
Plane strain block	0.00	0.14

5.5 Discussion

On the ratchet-limit algorithm

The developed method adopts plasticity theory equations. Thus, upgrading it from perfect plasticity to more general models follows the strategies developed for step-by-step incremental integration described in de Souza Neto et al. (2008). Indeed, the nonlinear kinematic hardening module is already integrated with the ratchet limit

determination module. Thus a systematic research on the existence of such limit, when using AF hardening is possible. This research is suggested as a future work using the implemented procedure and is outside the qualified scope of this thesis.

The same procedure can be applied for shakedown-limit identification simply substituting P_b by P_a inside the RL procedure. Here, the choice to pursue ratchet instead of shakedown limit is due to the to the apparent existence of a higher quantity of scientific gaps to fulfill in the former than the latter, when considering GSM materials. Despite of that, the implementation and use of this method to deal with shakedown has the advantage to be more natural to engineers that prefer to treat the problem without recovering to optimization theory.

The application of the procedure for shakedown identification, using nonlinear kinematic hardening is another potential research route. Naturally, the lessen theoretical basis of the AF model for shakedown also calls for caution and requires systematic research.

For the RL procedure, the presence of a sustained load is non-mandatory. Moreover, the method allows the analyst to choose any of the loads to amplify. No restriction applies on the number of different prescribed loads. In other words, the ratcheting boundary is not restricted to be a curve in a bi-dimensional Bree like interaction diagram. To the author knowledge, this is the first direct method for ratchet-limit determination with those capabilities. It follows the same path devised for shakedown with multi-dimensional loading spaces described in Simon and Weichert (2012).

Converged steady-state solutions build the ratcheting boundary, with no need of solving a modified limit load problem. In this aspect, it resembles a step-by-step incremental strategy, but without storing transient solution results and without wasting time to verify if the steady state was reached. The augmented secant method drives the algorithm automatically to the ratcheting boundary solution.

On the generality of non-ratcheting condition

A remarkable characteristic of shakedown analysis is that it allows the definition of a safe domain for loading programs rather than assuring safety for a particular loading program. For instance, this extension of safety assessment from a particular loading program to a domain of loading programs allows working under the realistic assumption that maximum ranges of loadings are anticipated instead of the complete history of loadings.

In general, the extension of a safety condition from a particular cyclic program to a domain encapsulating an infinite set of interior load paths holds true only inside the shakedown region König (1987); Ponter and Chen (2001); Zouain (2018).

To clarify this subject, Figure 5.16 combines two analytical ratchet-limit solu-

tions. The blue curve is the sustained primary loading program $\mathcal{C}(\eta_R)$ (vertical loading path) solution, given by Bree (1967). Whereas the red curve, is the rectangular program $\bar{\mathcal{C}}(\eta_R)$ ratcheting boundary, given by Bradford (2017).

The same figure identifies an example of sustained pressure program $\mathcal{C}(\eta^*)$ rendering ratcheting, once $\eta^* > \eta_R$. Remarkably, the same program is encapsulated by the rectangular $\bar{\mathcal{C}}(\eta_R)$.

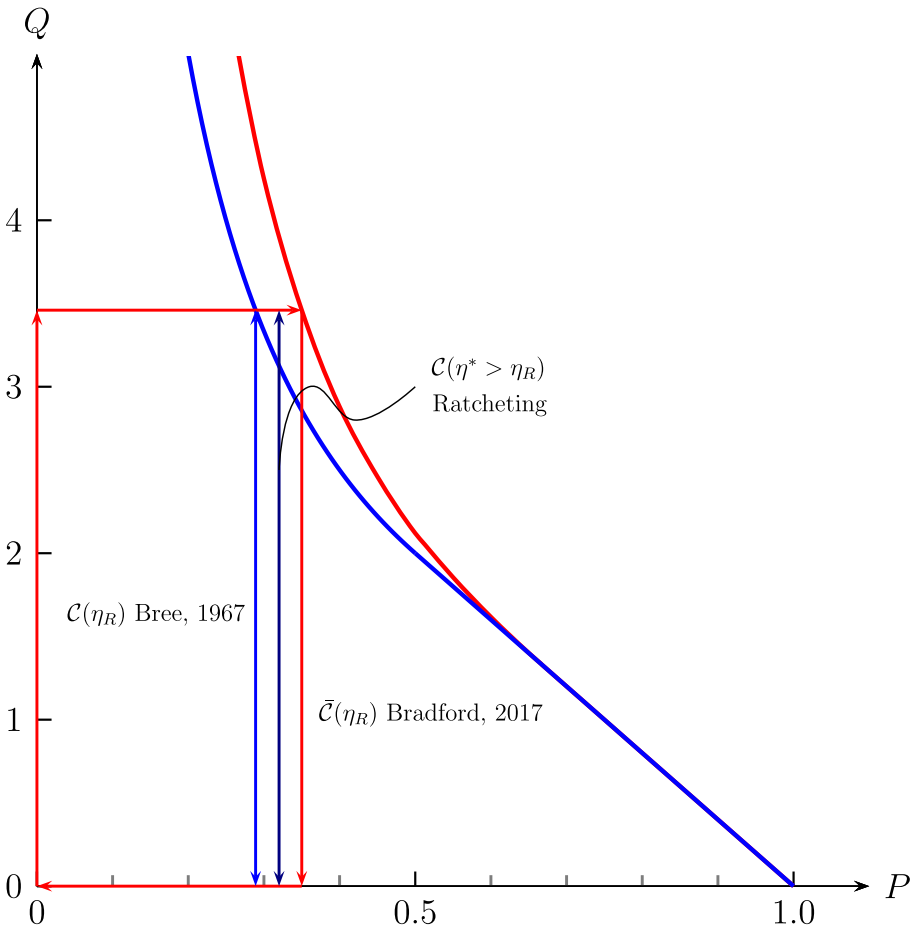

Figure 5.16: Counter-example on the ratcheting program to domain extension.

Indeed, the case constitutes a counter-example showing that the extension from safe program to safe domain does not hold inside the entire ratcheting boundary as it would inside shakedown limits. If the same extension kept its validity for the ratcheting limit, it would be impossible to identify any arbitrary cycle inside the rectangular cycle $\bar{\mathcal{C}}(\eta_R)$ capable of developing ratcheting.

Moreover, the author verified, by testing with direct and incremental methods, that a simple change in the orientation of the cycle has the potential to change the ratchet-limit position for some problems. This can be verified comparing the boundaries given in sections 4.7.1 and 5.4 for the closed tube. Both examples follow rectangular paths and differ only by its cyclic orientation, that is counter-clockwise

in the former against to clockwise in the latter. This observation corroborates with the suspects raised by Bradford (2017), which suggests this verification as a future work for the Bree model. The author intent to investigate this sensibility in future research.

The restriction has hidden implications in practical application of ratcheting limits for equipment integrity assessment. The proposed loading program must represent accurately the cyclic program that the equipment is expected to suffer.

Strictly speaking, the examples shows that a small modification in the cyclic regime can activate an unexpected ratcheting mechanism.

On the conceptual distinction of direct and incremental methods

Another remarkable observation, is that the conceptual distance between direct and incremental methods decreases when dealing with ratcheting boundary determination.

Outside shakedown limits, direct methods become restricted to identify loading program dependent structural responses. Paradoxically, this is the goal that motivated the development incremental methods. In direct methods, usually the goal is to identify load domain (encapsulating infinite programs inside) dependent structural responses.

Independently of the development intentions and the conceptual approximation, the superior computational performance and precision of the direct path justifies further research on such strategy, even when the establishment of safe domains is not possible.

Chapter 6

Nonlinear Kinematic Hardening

The contents of this chapter follows Zouain and SantAnna (2018). The article upgrades the direct method presented in chapter 4 with nonlinear kinematic hardening.

All the cited contributions were oriented and conduced with Professor Zouain close integration. The work benefited to understand the different types of ratcheting, and allowed the establishment of several future topics of research.

6.1 Introduction

Experiments with many metals shows Baushinger effect. That is a decrease in the compression yield stress after the plastic action in tension and vice versa. Theoretically, this effect can be included through a translation of the yield surface, that is with a kinematic hardening. Thus, the modeling requires the back-stress $\boldsymbol{A}$ as an additional variable. This state variable measures the translation of the yield surface inside the stress space.

Experimental evidences also display a bound in the translation of the yield surface and that the transition to this bound is asymptotic (Lemaitre and Chaboche, 1994). In other words, a nonlinear saturation in hardening. A model capable of reproducing those experimental facts is the one proposed by Armstrong and Frederick (1966).

Moreover, the chosen model can represent material ratcheting, that is, the plastic strain accumulation for unsymmetrical cycles of controlled stress acting in a material point. This capability may help in improving computational accuracy to model ratcheting as discussed in section 2.3.

6.2 Plasticity with nonlinear kinematic hardening

The elastoplastic material considered here behaves linear and isotropic in elasticity. Imposed thermal strains are isotropic and all material constants are independent of temperature. The Mises yield function and the Armstrong and Frederick (1966) kinematical hardening rule determine the plastic response. The constitutive equations are as follows (Auricchio and Taylor, 1995; de Souza Neto et al., 2008; Lemaitre and Chaboche, 1994)

$$\boldsymbol{S} = 2G(\boldsymbol{\varepsilon}^{dev} - \boldsymbol{\varepsilon}^{p}) \tag{6.1}$$

$$\sigma_m = K\,\mathrm{tr}\,(\boldsymbol{\varepsilon} - \boldsymbol{\varepsilon}^{\Theta}) \tag{6.2}$$

$$\boldsymbol{A} = \frac{2}{3}H^{\mathrm{kin}}\boldsymbol{\beta} \tag{6.3}$$

$$\mathrm{tr}\,(\boldsymbol{A}) = 0 \tag{6.4}$$

$$\boldsymbol{d}^{p} = \sqrt{\frac{3}{2}}\dot{\lambda}\boldsymbol{n} \tag{6.5}$$

$$\dot{\boldsymbol{A}} = \dot{\lambda}\left(\sqrt{\frac{2}{3}}H_{ki}\boldsymbol{n} - H_{nl}\boldsymbol{A}\right) \tag{6.6}$$

$$\boldsymbol{n} = \frac{\boldsymbol{S} - \boldsymbol{A}}{\|\boldsymbol{S} - \boldsymbol{A}\|} \tag{6.7}$$

$$f(\boldsymbol{S}, \boldsymbol{A}) = \sqrt{\frac{3}{2}}\|\boldsymbol{S} - \boldsymbol{A}\| - \sigma_Y^0 \leq 0 \tag{6.8}$$

$$\dot{\lambda}f(\boldsymbol{S}, \boldsymbol{A}) = 0 \tag{6.9}$$

$$\dot{\lambda} \geq 0 \tag{6.10}$$

where G and K are the shear and bulk elastic moduli, "tr" is the trace operator, and the constants H_{ki} and H_{nl} are the linear and nonlinear kinematic hardening coefficients.

The inclusion of the back-stress $\boldsymbol{A}$ imposes its dual strain-like internal variable $\boldsymbol{\beta}$, as a consequence. Thus, the specific dissipation is $\mathsf{d}_{\mathrm{int}} = \boldsymbol{\sigma} \cdot \boldsymbol{d}^{p} - \boldsymbol{A} \cdot \dot{\boldsymbol{\beta}}$ for this model.

Relations (6.1–6.4) are the state equations of the material. The plastic strain evolution (6.5) is associated with respect to the plastic function (6.8). Equations (6.5) and (6.7) give rise to the following relation.

$$\dot{\lambda} = d^{p}_{eq} = \sqrt{\frac{2}{3}}\|\boldsymbol{d}^{p}\| \tag{6.11}$$

The hardening evolution (6.6) is non-associated whenever $H_{nl} \neq 0$. Remarkably,

the associativity would demand that

$$\dot{\boldsymbol{\beta}} = -\frac{\partial(f(\boldsymbol{S},\boldsymbol{A}))}{\partial \boldsymbol{A}} = \boldsymbol{d}^p. \tag{6.12}$$

However, (6.6) can be viewed in the form

$$\dot{\boldsymbol{\beta}} = \boldsymbol{d}^p - H_{nl} d^p_{eq} \boldsymbol{\beta} \tag{6.13}$$

due to (6.3), (6.5) and (6.11), thus not satisfying (6.12). Pragers linear hardening is recovered for $H_{nl} = 0$, in which case the backstress is unbounded and the model becomes associated.

For an effective AF hardening, with $H_{nl} > 0$, the following bound for the equivalent back-stress is deduced from (6.6).

$$\sqrt{\frac{3}{2}}\|\boldsymbol{A}\| \leq \frac{H_{ki}}{H_{nl}} \tag{6.14}$$

Consequently, using $\|\boldsymbol{S}\| \leq \|\boldsymbol{S} - \boldsymbol{A}\| + \|\boldsymbol{A}\|$ and (6.8)

$$\|\boldsymbol{S}\| \leq \sigma_{Y\infty} = \sigma^0_Y + \frac{H_{ki}}{H_{nl}} \tag{6.15}$$

6.3 The equations of steady state with AF hardening

The mechanical and thermal loadings are represented again by the fictitious elastic field $\boldsymbol{\sigma}^E(t)$, for $t \in (0,1)$ and the main unknown is the residual stress, varying in space and time.

The following set of equations governs the asymptotic cyclic response and it is analogous to the one deduced by Polizzotto (2003, p.2679) for GSM. This system of equations is part of the set that characterizes incremental analysis under a general loading program (possibly non-cyclic). The main difference between both analyses is that the initial conditions of the incremental problem are substituted, in the direct asymptotic analysis, by constraints enforcing the asymptotic stress and backstress to be cyclic and with same period as the loadings. The self-equilibrium condition, at all times, is imposed here in a simplified manner, taking into account the periodicity constraint, as explained below.

Given $\boldsymbol{\sigma}^E(t)$, find $\boldsymbol{\sigma}^r(t)$, $\boldsymbol{A}(t)$ and $\boldsymbol{d}^p(t)$ such that, for all times

$$\boldsymbol{S} = \boldsymbol{\sigma}^{E,\mathrm{dev}} + \boldsymbol{\sigma}^{r,\mathrm{dev}} \tag{6.16}$$

$$\boldsymbol{d}^p = \sqrt{\tfrac{3}{2}}\dot{\lambda}\boldsymbol{n} \tag{6.17}$$

$$\dot{\boldsymbol{A}} = \dot{\lambda}\left(\sqrt{\tfrac{2}{3}}H_{ki}\boldsymbol{n} - H_{nl}\boldsymbol{A}\right) \tag{6.18}$$

$$\boldsymbol{n} = \frac{\boldsymbol{S}-\boldsymbol{A}}{\|\boldsymbol{S}-\boldsymbol{A}\|} \tag{6.19}$$

$$f = \sqrt{\tfrac{3}{2}}\|\boldsymbol{S}-\boldsymbol{A}\| - \sigma_Y^0 \leq 0 \qquad \dot{\lambda} \geq 0 \qquad \dot{\lambda} f = 0 \tag{6.20}$$

$$\dot{\boldsymbol{\sigma}}^r = \boldsymbol{\mathcal{Z}}\boldsymbol{d}^p \tag{6.21}$$

and at the end of each cycle

$$\boldsymbol{\sigma}^r(1) = \boldsymbol{\sigma}^r(0) \tag{6.22}$$

$$\mathcal{D}'\boldsymbol{\sigma}^r(1) = \boldsymbol{0} \tag{6.23}$$

$$\boldsymbol{A}(1) = \boldsymbol{A}(0) \tag{6.24}$$

The equilibrium conditions, $\mathcal{D}'\boldsymbol{\sigma}^r = \boldsymbol{0}$ for all $t \in (0,1)$, are deduced now from (6.21–6.23). Indeed, $\mathcal{D}'\dot{\boldsymbol{\sigma}}^r = \boldsymbol{0}$ because of (6.21) and the fact that the range of $\boldsymbol{\mathcal{Z}}$ is the self-equilibrium space; hence $\boldsymbol{\sigma}^r(t) = \boldsymbol{\sigma}^r(0) + \int_0^t \dot{\boldsymbol{\sigma}}^r(t)dt^*$ is self-equilibrated, since $\mathcal{D}'\boldsymbol{\sigma}^r(0) = \mathcal{D}'\boldsymbol{\sigma}^r(1) = \boldsymbol{0}$ due to (6.22) and (6.23).

Another important consequence of the asymptotic response equations (6.16–6.24) is that the increment of plastic strain accumulated in each cycle, $\Delta\boldsymbol{\varepsilon}$, is compatible. That is, there exists a displacement field $\Delta\boldsymbol{u}$, giving the increment of deformation produced in any cycle, and such that

$$\mathcal{D}\Delta\boldsymbol{u} = \Delta\boldsymbol{\varepsilon} \qquad \Delta\boldsymbol{\varepsilon} = \int_0^1 \boldsymbol{d}^p dt \tag{6.25}$$

where $\boldsymbol{d}^p$ solves (6.16–6.24). This is proven, for instance, in Zouain and SantAnna (2017, p. 269) and reproduced in section 4.2.

In this formulation, (6.25) constitutes a subsidiary relation determining the increment of displacement per cycle $\Delta\boldsymbol{u}$. The subsidiary problem $\mathcal{D}\Delta\boldsymbol{u} = \Delta\boldsymbol{\varepsilon}$ is consistent and has a unique solution because $\Delta\boldsymbol{u}$ is kinematically compatible and $\mathcal{D}$ is non-singular. However, $\Delta\boldsymbol{u}$ is only approximately compatible when obtained in the computational solution of (6.16–6.24) and hence the subsidiary problem may become numerically inconsistent. In view of this, $\Delta\boldsymbol{u}$ is computed solving the linear system

$$\boldsymbol{\mathcal{K}}\Delta\boldsymbol{u} = \mathcal{D}'\mathbb{E}\Delta\boldsymbol{\varepsilon} \tag{6.26}$$

This is equivalent to $\mathcal{D}\Delta\boldsymbol{u} = \Delta\boldsymbol{\varepsilon}$, whenever $\Delta\boldsymbol{\varepsilon}$ is exactly compatible, and always has a unique solution (even for an incompatible $\Delta\boldsymbol{\varepsilon}$). In addition, the corresponding matrix of the system (6.26) is already available in decomposed form and the right-hand side is easily computed.

6.4 The discretized equations of the steady state

Discrete counterparts of the proposed continuum equations are generated defining a grid in the time interval $[0, 1]$ and using finite element interpolations for the stress and displacement fields or using traditional kinematical interpolations. It is adopted here the mixed finite elements presented in Zouain et al. (2014).

The present algorithm has two alternative approximate integrations of the evolution equations, following techniques of stress analysis in the presence of nonlinear hardening. These alternatives are: (i) the backward Euler integration scheme, and (ii) the generalized midpoint rule, aiming second-order accuracy (Artioli et al., 2007). As a result, it is ensured that the direct solution exactly matches the one obtained, at the stabilized regime, by a conventional incremental analysis that uses the same integration, mesh and finite element interpolation.

Spatial and time discretizations

The procedure adopts the same strategy present in section 4.5 for discretization in time and space. Complementing the notation presented in the cited section, the discretized backstress vector at the time station j is $\boldsymbol{A}^j := \boldsymbol{A}(t_j)$.

6.5 An algorithm for computing the steady state

The iterative algorithm solves the elastoplastic steady state problem, which is based on a discretized version of the formulation (6.16-6.24). The main proposal is to perform a fictitious sequence of cycles aiming to reduce the residuals of these equations.

The procedure consists in a sequence of substitutions: in $\delta\boldsymbol{\sigma}^r = \boldsymbol{\mathcal{Z}}\delta\boldsymbol{\varepsilon}^p$, to update residual stresses, combined with return mappings, using evolution relations, to update plastic strain increments.

This algorithm is presented in two stages. First, the basic update procedure, BU, at each time station. Second, the global procedure for computing the elastoplastic steady state, ESS, constituted of nested loops that apply the basic update.

This section explains a crucial component of the algorithm for direct cyclic analysis. It consists of the following modification in the return mapping of the usual integration of elastoplastic analysis.

First, consider the backward Euler approximation of the constitutive equations (6.1-6.10).

$$\boldsymbol{S}^j - \boldsymbol{S}^{j-1} = 2G(\delta\boldsymbol{\varepsilon}^{\text{dev}} - \delta\boldsymbol{\varepsilon}^p) \tag{6.27}$$

$$\delta\sigma_m = K \operatorname{tr}\left(\delta\boldsymbol{\varepsilon} - \delta\boldsymbol{\varepsilon}^{\Theta}\right) \tag{6.28}$$

$$\delta\boldsymbol{\varepsilon}^p = \delta\lambda\boldsymbol{n} \tag{6.29}$$

$$\boldsymbol{A}^j - \boldsymbol{A}^{j-1} = \delta\lambda\left(\sqrt{\tfrac{2}{3}}H_{ki}\boldsymbol{n} - H_{nl}\boldsymbol{A}^j\right) \tag{6.30}$$

$$\boldsymbol{n} = \frac{\boldsymbol{S}^j - \boldsymbol{A}^j}{\|\boldsymbol{S}^j - \boldsymbol{A}^j\|} \tag{6.31}$$

$$f = \sqrt{\tfrac{3}{2}}\|\boldsymbol{S}^j - \boldsymbol{A}^j\| - \sigma_Y^0 \leqslant 0 \qquad \delta\lambda \geqslant 0 \qquad f\delta\lambda = 0 \tag{6.32}$$

In incremental analysis, the usual projection procedure, driven by a globally computed strain increment $\delta\boldsymbol{\varepsilon}$, is to set $\bar{\boldsymbol{S}}^{\text{trial}} := \boldsymbol{S}^{j-1} + 2G\delta\boldsymbol{\varepsilon}^{\text{dev}}$ and then solve the system above with (6.27) in the form $\bar{\boldsymbol{S}}^{\text{trial}} = \boldsymbol{S}^j + 2G\delta\boldsymbol{\varepsilon}^p$.

The present algorithm adopts a different trial stress for asymptotic analysis. Specifically, using the current approximations denoted by $\boldsymbol{S}^{r,j}$, $\delta\boldsymbol{\varepsilon}^{p,j}$ and $\boldsymbol{A}^{j-1}$, the driving parameters are defined, according to Figure 6.1.ii, as

$$\boldsymbol{S}^{\text{trial}} := \boldsymbol{S}^{E,j} + \boldsymbol{S}^{r,j} + 2G\delta\boldsymbol{\varepsilon}^{p,j} \qquad \boldsymbol{A}^{\text{trial}} := \boldsymbol{A}^{j-1} \tag{6.33}$$

where $\boldsymbol{S}^{E,j} := (\boldsymbol{\sigma}^{E,j})^{\text{dev}}$ and $\boldsymbol{S}^{r,j} := (\boldsymbol{\sigma}^{r,j})^{\text{dev}}$ are the deviatoric parts of the residual and ideally elastic stresses at time j.

Then, the method finds the new approximations $\delta\hat{\boldsymbol{\varepsilon}}^{p,j}$ and $\hat{\boldsymbol{A}}^j$ by solving the following backward Euler version of the constitutive relations (6.1-6.10), with additional (dummy) unknowns $\tilde{\boldsymbol{S}}$, $\delta\lambda$ and $\boldsymbol{n}$. That is (Figure 6.1.ii)

$$\boldsymbol{S}^{\text{trial}} = \tilde{\boldsymbol{S}} + 2G\delta\hat{\boldsymbol{\varepsilon}}^{p,j} \tag{6.34}$$

$$\hat{\boldsymbol{\varepsilon}}^{p,j} = \sqrt{\tfrac{3}{2}}\delta\lambda\boldsymbol{n} \tag{6.35}$$

$$\hat{\boldsymbol{A}}^j - \boldsymbol{A}^{\text{trial}} = \delta\lambda\left(\sqrt{\tfrac{2}{3}}H_{ki}\boldsymbol{n} - H_{nl}\hat{\boldsymbol{A}}^j\right) \tag{6.36}$$

$$\boldsymbol{n} = \frac{\tilde{\boldsymbol{S}} - \hat{\boldsymbol{A}}^j}{\|\tilde{\boldsymbol{S}} - \hat{\boldsymbol{A}}^j\|} \tag{6.37}$$

$$f = \sqrt{\tfrac{3}{2}}\|\tilde{\boldsymbol{S}} - \hat{\boldsymbol{A}}^j\| - \sigma_Y^0 \leqslant 0 \qquad \delta\lambda \geqslant 0 \qquad f\,\delta\lambda = 0 \tag{6.38}$$

The system (6.34-6.38) is formally identical to a standard incremental return mapping. The trial parameters, given by (6.33), are the only special assumptions pertaining to the asymptotic algorithm.

Consequently, the method can perform this projection using common tools pro-

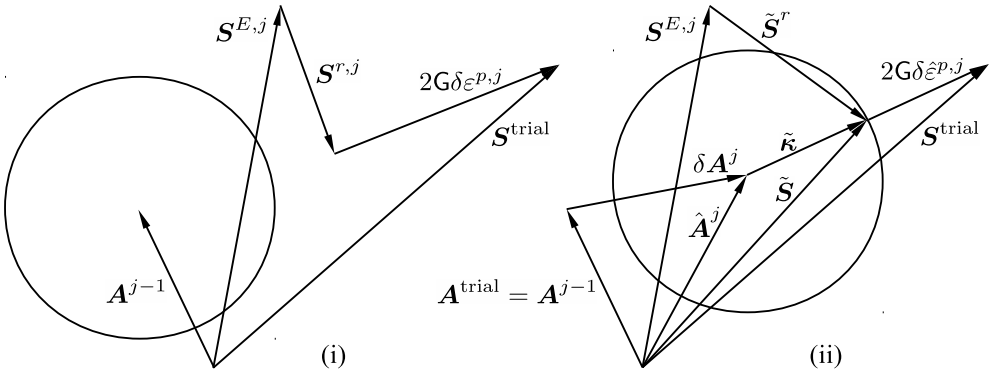

Figure 6.1: Projection procedure to obtain new iterates $\delta\hat{\boldsymbol{\varepsilon}}^{p,j}$ and $\hat{\boldsymbol{A}}^j$: (i) compute trial stress $\boldsymbol{S}^{\text{trial}}$, by (6.33), and (ii) project $\boldsymbol{S}^{\text{trial}}$ to find the updates.

posed and tested in a vast literature; see for instance Simo and Hughes (2006), de Souza Neto et al. (2008), Auricchio and Taylor (1995), Artioli et al. (2007), Armero (2018) and De Angelis and Taylor (2016).

In summary, the above return mapping computes, at local level, new iterates $\delta\hat{\boldsymbol{\varepsilon}}^{p,j}$ and $\hat{\boldsymbol{A}}^j$, for plastic strain increments and hardening variables, which are then used as input for a global operation to update the residual stresses. This scheme is formalized in the following basic update procedure.

6.5.1 Basic update (BU) at time station j

The update procedure is defined in the form of a pseudo-code, and afterward justified in some remarks.

Procedure BU (at time station j)
Given the current global approximations, $\boldsymbol{\sigma}^{r,(j-1)} = \boldsymbol{S}^{r,(j-1)} + \sigma_m^{r,(j-1)}\boldsymbol{1}$, $\boldsymbol{A}^{j-1}$, $\boldsymbol{\sigma}^{r,j} = \boldsymbol{S}^{r,j} + \sigma_m^{r,j}\boldsymbol{1}$ and $\delta\boldsymbol{\varepsilon}^{p,j}$, such that

$$\boldsymbol{\sigma}^{r,j} - \boldsymbol{\sigma}^{r,(j-1)} = \boldsymbol{Z}\delta\boldsymbol{\varepsilon}^{p,j} \qquad \boldsymbol{B}^T\boldsymbol{\sigma}^{r,(j-1)} = \boldsymbol{0} \tag{6.39}$$

compute the new iterates, $\hat{\boldsymbol{\sigma}}^{r,j} = \hat{\boldsymbol{S}}^{r,j} + \hat{\sigma}_m^{r,j}\boldsymbol{1}$, $\hat{\boldsymbol{A}}^{j}$ and $\delta\hat{\boldsymbol{\varepsilon}}^{p,j}$, as follows.

1. **for** all control points of the mesh
   Set (Figure 6.1)

$$\boldsymbol{S}^{\text{trial}} := \boldsymbol{S}^{E,j} + \boldsymbol{S}^{r,j} + 2G\delta\boldsymbol{\varepsilon}^{p,j} \tag{6.40}$$

$$\boldsymbol{A}^{\text{trial}} := \boldsymbol{A}^{j-1} \tag{6.41}$$

   if $\sqrt{\frac{3}{2}}\|\boldsymbol{S}^{\text{trial}} - \boldsymbol{A}^{\text{trial}}\| \leqslant \sigma_Y^0$

   then Elastic step. Set

$$\delta\hat{\boldsymbol{\varepsilon}}^{p,j} = \boldsymbol{0} \qquad \hat{\boldsymbol{A}}^{j} = \boldsymbol{A}^{\text{trial}} \tag{6.42}$$

   else Elastoplastic step.
   Find new approximations, $\delta\hat{\boldsymbol{\varepsilon}}^{p,j}$ and $\hat{\boldsymbol{A}}^{j}$, by solving the following system for the unknowns $\tilde{\boldsymbol{S}}$, $\hat{\boldsymbol{A}}^{j}$, $\delta\hat{\boldsymbol{\varepsilon}}^{p,j}$, $\delta\lambda > 0$ and $\boldsymbol{n}$.

$$\boldsymbol{S}^{\text{trial}} = \tilde{\boldsymbol{S}} + 2G\delta\hat{\boldsymbol{\varepsilon}}^{p,j} \tag{6.43}$$

$$\hat{\boldsymbol{\varepsilon}}^{p,j} = \sqrt{\tfrac{3}{2}}\delta\lambda\boldsymbol{n} \tag{6.44}$$

$$\hat{\boldsymbol{A}}^{j} - \boldsymbol{A}^{\text{trial}} = \delta\lambda\left(\sqrt{\tfrac{2}{3}}H_{ki}\boldsymbol{n} - H_{nl}\hat{\boldsymbol{A}}^{j}\right) \tag{6.45}$$

$$\boldsymbol{n} = \frac{\tilde{\boldsymbol{S}} - \hat{\boldsymbol{A}}^{j}}{\|\tilde{\boldsymbol{S}} - \hat{\boldsymbol{A}}^{j}\|} \tag{6.46}$$

$$\sqrt{\tfrac{3}{2}}\|\tilde{\boldsymbol{S}} - \hat{\boldsymbol{A}}^{j}\| = \sigma_Y^0 \tag{6.47}$$

   end if
end for

2. Compute new approximation of the residual stress

$$\hat{\boldsymbol{\sigma}}^{r,j} = \boldsymbol{\sigma}^{r,(j-1)} + \boldsymbol{Z}\delta\hat{\boldsymbol{\varepsilon}}^{p,j} \tag{6.48}$$

end of Procedure BU

Algorithm 4: Basic Update with AF

Remarks on Procedure BU

1. Conditions (6.39), assumed to be fulfilled by the input and involving $\boldsymbol{\sigma}^{r,(j-1)}$, $\boldsymbol{\sigma}^{r,j}$ and $\delta\boldsymbol{\varepsilon}^{p,j}$, are also satisfied by the output $\hat{\boldsymbol{\sigma}}^{r,j}$ and $\delta\hat{\boldsymbol{\varepsilon}}^{p,j}$, due to (6.48).

2. The projection procedure defined by (6.43-6.47) and sketched in Figure 6.1 is analyzed in the section 6.6.

3. If the input satisfies (6.43-6.47), the basic updating procedure replicates the input values at the output, that is $\hat{\boldsymbol{\sigma}}^{r,j} = \boldsymbol{\sigma}^{r,j}$, $\delta\hat{\boldsymbol{\varepsilon}}^{p,j} = \delta\boldsymbol{\varepsilon}^{p,j}$ and $\hat{\boldsymbol{A}}^{j} = \boldsymbol{A}^{j}$. Hence, the heuristic equality (6.40) does not introduce any spurious constraint on the converged solution. Furthermore, it holds that a fixed point for the projection procedure (6.43-6.47) is necessarily comprised by a plastically admissible total net stress $\boldsymbol{\kappa}^{j} := \boldsymbol{\sigma}^{E,j} + \boldsymbol{\sigma}^{r,j} - \boldsymbol{A}^{j}$ and a plastic flow $\delta\boldsymbol{\varepsilon}^{p,j}$ associated with $\boldsymbol{\sigma}^{E,j} + \boldsymbol{\sigma}^{r,j}$.

6.5.2 An algorithm for computing the elastoplastic steady state

The algorithm to compute the stabilized elastoplastic response consists of a sequence of fictitious time cycles, described in the following.

At each time step, labeled by $j \in 1:N$, it is performed a loop of applications of the basic update procedure BU. The loop ends when the difference between successive approximations of residual stress at one BU, $\int_{\mathcal{B}} \|\hat{\boldsymbol{\sigma}}^{r,j} - \boldsymbol{\sigma}^{r,j}\| d\mathbf{x}$, becomes less than a prescribed tolerance for the step, or when the number of loops exceeds $k_{\max}$.

At the end of each fictitious cycle, the total difference of residual stress $\sum_{j=1:N} \int_{\mathcal{B}} \|\boldsymbol{\sigma}^{r,j} - \boldsymbol{\sigma}^{r,j,\mathrm{old}}\| d\mathbf{x}$ is checked for convergence. If a fixed point for the iterative algorithm is attained, then the current iterate solves the set of equations determining the asymptotic elastoplastic response.

The algorithm pseudo-code is given in the following.

Procedure: Elastoplastic steady state (ESS)

Compute iteratively $\boldsymbol{\sigma}^{r,j}$, $\delta\boldsymbol{\varepsilon}^{p,j}$ and $\boldsymbol{A}^j$ as follows:

Initialize $\quad \text{icyc} = 0; \quad \boldsymbol{\sigma}^{r,j} = \mathbf{0}, \quad \delta\boldsymbol{\varepsilon}^{p,j} = \mathbf{0}, \quad \hat{\boldsymbol{A}}^j = \mathbf{0},$
$\text{Var}(\boldsymbol{\sigma}^r) = \text{big}; \quad \text{var}_j(\boldsymbol{\sigma}^{r,j}) = \text{big}, \quad j = 1 : N$

do while $\quad (\text{icyc} \leqslant \text{icyc}_{\max} \quad \textbf{and} \quad \text{Var}(\boldsymbol{\sigma}^r) \geqslant \text{tol}_{\text{cyc}})$

$\text{icyc} = \text{icyc} + 1$

for $j = 1 : N$

$k = 0$

$\boldsymbol{\sigma}^{r,j,\text{old}} = \boldsymbol{\sigma}^{r,j}$

do while $\quad \big(k \leqslant k_{\max} \quad \textbf{and} \quad \text{var}_j(\boldsymbol{\sigma}^{r,j}) \geqslant \text{tol}_{\text{step}}\big)$

$k = k + 1$

Use procedure BU to compute new iterates $\hat{\boldsymbol{\sigma}}^{r,j}$, $\delta\hat{\boldsymbol{\varepsilon}}^{p,j}$ and $\hat{\boldsymbol{A}}^j$.

$\tau_j = \int_{\mathcal{B}} \|\hat{\boldsymbol{\sigma}}^{r,j}\| d\mathbf{x}$

$\xi_j = \int_{\mathcal{B}} \|\hat{\boldsymbol{\sigma}}^{r,j} - \boldsymbol{\sigma}^{r,j}\| d\mathbf{x}$

$\text{var}_j(\boldsymbol{\sigma}^{r,j}) = \xi_j / \max\{\tau_j, 1\}$

Update $\quad \boldsymbol{\sigma}^{r,j} = \hat{\boldsymbol{\sigma}}^{r,j}, \quad \delta\boldsymbol{\varepsilon}^{p,j} = \delta\hat{\boldsymbol{\varepsilon}}^{p,j}, \quad \boldsymbol{A}^j = \hat{\boldsymbol{A}}^j$

end do

end for

$\xi_j = \int_{\mathcal{B}} \|\boldsymbol{\sigma}^{r,j} - \boldsymbol{\sigma}^{r,j,\text{old}}\| d\mathbf{x}$

$\text{Var}(\boldsymbol{\sigma}^r) = (\sum_{1:N} \xi_j) \,/\, \max\{\sum_{1:N} \tau_j, 1\}$

end do

$\boldsymbol{\sigma}^j = \boldsymbol{\sigma}^{E,j} + \boldsymbol{\sigma}^{r,j}, \quad j = 1 : N$

$\Delta\boldsymbol{\varepsilon} = \sum_{j=1:N} \delta\boldsymbol{\varepsilon}^{p,j}$

$\Delta\boldsymbol{u} = \boldsymbol{K}^{-1}\boldsymbol{B}^T\mathbb{E}\Delta\boldsymbol{\varepsilon}$

end procedure ESS

Algorithm 5: Elastoplastic steady state with AF

This fictitious sequence of cycles qualifies a direct method using similar arguments to the ones described in section 4.6.2. Again, remarkably, the stiffness matrix $\boldsymbol{K}$ is decomposed only once in the preamble.

6.6 The return mapping problem

This section is devoted to the solution of the return mapping problem, defined by (6.43-6.47), adopting the backward Euler integration, or by (6.88-6.93), when

generalized midpoint integration is used. It follows Auricchio and Taylor (1995), Artioli et al. (2007) and De Angelis and Taylor (2016).

6.6.1 Using backward Euler integration

The return mapping (6.43-6.47) is reformulated below.

The notation used in Figure 6.1 is simplified as: $\boldsymbol{S} := \tilde{\boldsymbol{S}} = \boldsymbol{S}^{E,j} + \tilde{\boldsymbol{S}}^{r}$ (dropping the tilde), $\boldsymbol{A} := \hat{\boldsymbol{A}}^{j}$ and $\delta\boldsymbol{\varepsilon}^{p} := \delta\hat{\boldsymbol{\varepsilon}}^{p,j}$ (dropping hat and superscripts).

Problem 1. Given: $\boldsymbol{S}^{\text{trial}}$ and $\boldsymbol{A}^{\text{trial}}$ as in (6.40) and (6.41).

Find: $\boldsymbol{S}$, $\boldsymbol{A}$, $\delta\lambda > 0$ and $\boldsymbol{n}$ such that

$$\boldsymbol{S}^{\text{trial}} = \boldsymbol{S} - \sqrt{6}G\delta\lambda\boldsymbol{n} \tag{6.49}$$

$$\boldsymbol{A} = \boldsymbol{A}^{\text{trial}} + \delta\lambda\left(\sqrt{\tfrac{2}{3}}H_{ki}\boldsymbol{n} - H_{nl}\boldsymbol{A}\right) \tag{6.50}$$

$$\boldsymbol{n} = \frac{\boldsymbol{S} - \boldsymbol{A}}{\|\boldsymbol{S} - \boldsymbol{A}\|} \tag{6.51}$$

$$\sqrt{\tfrac{3}{2}}\|\boldsymbol{S} - \boldsymbol{A}\| = \sigma_Y^0 \tag{6.52}$$

The next section describes how this system is solved in the present implementation. The most effective strategy is adopted (Auricchio and Taylor, 1995; De Angelis and Taylor, 2016; de Souza Neto et al., 2008) consisting of first reducing the problem to an independent equation in $\delta\lambda$. In this case, $\delta\lambda$ is the least positive root of the fourth-order polinomial. Once $\delta\lambda$ is obtained, the algorithm computes the other unknowns as follows.

$$T_\lambda = (1 + H_{nl}\delta\lambda)^{-1} \tag{6.53}$$

$$\boldsymbol{\kappa}^{\text{trial}} = \boldsymbol{S}^{\text{trial}} - T_\lambda\boldsymbol{A}^{\text{trial}} \tag{6.54}$$

$$\boldsymbol{n} = \frac{\boldsymbol{\kappa}^{\text{trial}}}{\|\boldsymbol{\kappa}^{\text{trial}}\|} \tag{6.55}$$

$$\boldsymbol{S} = \boldsymbol{S}^{\text{trial}} - \sqrt{6}G\delta\lambda\boldsymbol{n} \tag{6.56}$$

Finally, the method updates the selected variables as

$$\delta\hat{\boldsymbol{\varepsilon}}^{p,j} = \sqrt{\tfrac{3}{2}}\delta\lambda\boldsymbol{n} \tag{6.57}$$

$$\hat{\boldsymbol{A}}^{j} = T_\lambda\left(\boldsymbol{A}^{\text{trial}} + \sqrt{\tfrac{2}{3}}H_{ki}\delta\lambda\boldsymbol{n}\right) \tag{6.58}$$

$$\delta\hat{\boldsymbol{\beta}}^{j} = \tfrac{3}{2H_{ki}}(\hat{\boldsymbol{A}}^{j} - \boldsymbol{A}^{\text{trial}}) \tag{6.59}$$

It is not necessary to calculate $\boldsymbol{S}$ here because the stresses are only updated in

the global stage (6.48) of the basic procedure BU.

The polynomial equation in the backward Euler integration

This section describes the equations and procedures (Auricchio and Taylor, 1995; De Angelis and Taylor, 2016) used to solve Problem 1, given by (6.49-6.52).

First, setting $\boldsymbol{\kappa} := \boldsymbol{S} - \boldsymbol{A}$ and simplifying Problem 1 to the following form.

Given: $\boldsymbol{S}^{\text{trial}}$ and $\boldsymbol{A}^{\text{trial}}$ as in (6.40) and (6.41).
Find $\boldsymbol{\kappa}$, $\delta\lambda > 0$ and $\boldsymbol{n}$ such that

$$\boldsymbol{\kappa} = \boldsymbol{S}^{\text{trial}} - T_\lambda \boldsymbol{A}^{\text{trial}} - U_\lambda \boldsymbol{n} \tag{6.60}$$

$$\boldsymbol{n} = \frac{\boldsymbol{\kappa}}{\|\boldsymbol{\kappa}\|} \tag{6.61}$$

$$T_\lambda = (1 + H_{nl}\delta\lambda)^{-1} \tag{6.62}$$

$$U_\lambda = \left(\sqrt{6}G + \sqrt{\tfrac{2}{3}}H_{ki}T_\lambda\right)\delta\lambda \tag{6.63}$$

$$\sqrt{\tfrac{3}{2}}\|\boldsymbol{\kappa}\| = \sigma_Y^0 \tag{6.64}$$

with subsidiary equations

$$\boldsymbol{A} = T_\lambda\left(\boldsymbol{A}^{\text{trial}} + \sqrt{\tfrac{2}{3}}H_{ki}\delta\lambda\boldsymbol{n}\right) \tag{6.65}$$

$$\boldsymbol{S} = \boldsymbol{\kappa} + \boldsymbol{A} \tag{6.66}$$

The solution of the above problem is considered next.

From (6.60) it is obtained

$$\boldsymbol{\kappa}^{\text{trial}}(\delta\lambda) := \boldsymbol{S}^{\text{trial}} - T_\lambda \boldsymbol{A}^{\text{trial}} = \boldsymbol{\kappa} + U_\lambda \boldsymbol{n} \tag{6.67}$$

Since $\boldsymbol{\kappa} = \|\boldsymbol{\kappa}\|\boldsymbol{n}$ and $U_\lambda > 0$ it is deduced now that $\boldsymbol{\kappa}^{\text{trial}} = \|\boldsymbol{\kappa}^{\text{trial}}\|\boldsymbol{n}$ and

$$\|\boldsymbol{S}^{\text{trial}} - T_\lambda \boldsymbol{A}^{\text{trial}}\| = \|\boldsymbol{\kappa}\| + U_\lambda \tag{6.68}$$

Moreover, by using (6.64), a transform (6.68) in

$$s_{SS} + T_\lambda^2 s_{AA} - 2T_\lambda s_{SA} = (\sqrt{\tfrac{2}{3}}\sigma_Y^0 + U_\lambda)^2 \tag{6.69}$$

applies with

$$s_{SS} := \|\boldsymbol{S}^{\text{trial}}\|^2 \qquad s_{AA} := \|\boldsymbol{A}^{\text{trial}}\|^2 \qquad s_{SA} := \boldsymbol{S}^{\text{trial}} \cdot \boldsymbol{A}^{\text{trial}} \tag{6.70}$$

The relation (6.69) is a nonlinear scalar equation for the single variable $\delta\lambda$ that reduces to the following quartic

$$p(\delta\lambda) = 0 \qquad p(t) := a_4 t^4 + a_3 t^3 + a_2 t^2 + a_1 t + a_0 \tag{6.71}$$

where

$$a_4 = 6G^2 H_{nl}^2 > 0 \tag{6.72}$$

$$a_3 = 12G^2 H_{nl} + 4G H_{ki} H_{nl} + 4G H_{nl}^2 \sigma_Y^0 > 0 \tag{6.73}$$

$$a_2 = 6G^2 + 4G H_{ki} + \tfrac{2}{3} H_{ki}^2 + 8G H_{nl} \sigma_Y^0 + \tfrac{4}{3} H_{ki} H_{nl} \sigma_Y^0 + \tfrac{2}{3} H_{nl}^2 \sigma_{Y0}^2 - H_{nl}^2 s_{SS} \tag{6.74}$$

$$a_1 = 4G\sigma_Y^0 + \tfrac{4}{3} H_{ki} \sigma_Y^0 + \tfrac{4}{3} H_{nl} \sigma_{Y0}^2 - 2H_{nl} \left(s_{SS} - s_{SA}\right) \tag{6.75}$$

$$a_0 = \tfrac{2}{3} \sigma_{Y0}^2 - s_{SS} + 2s_{SA} - s_{AA} < 0 \tag{6.76}$$

Then, $\delta\lambda$ is the least positive root of the quartic polynomial (6.71), computed by Laguerre's method.

In particular, the solution for linear hardening, when $H_{nl} = 0$, is directly obtained as

$$\delta\lambda = \frac{\sqrt{\mathrm{b}^2 - \mathrm{ac}} - \mathrm{b}}{\mathrm{a}} \tag{6.77}$$

where

$$\mathrm{a} = 6G^2 + 4G H_{ki} + \tfrac{2}{3} H_{ki}^2 > 0 \tag{6.78}$$

$$\mathrm{b} = 2G\sigma_Y^0 + \tfrac{2}{3} H_{ki} \sigma_Y^0 > 0 \tag{6.79}$$

$$\mathrm{c} = \tfrac{2}{3} \sigma_{Y0}^2 - s_{SS} + 2s_{SA} - s_{AA} < 0 \tag{6.80}$$

6.6.2 Using generalized midpoint integration

This subsection introduces a generalized midpoint approximation (Artioli et al., 2007; de Souza Neto et al., 2008; Iserles, 2009) for the evolution equations in each time step, as an alternative in the proposed method.

In this case, the modeling only substitutes the system of equations (6.43-6.47) by the system (6.88-6.93), as described in the following. Besides this modification, both procedures, BU and ESS, remain unchanged.

The model adopts the following generalized midpoint integration of the constitutive equations (6.16-6.20), depending on the parameter $\vartheta \in [0, 1]$. Here, $\vartheta = 1$

gives the backward Euler approximation, $\vartheta = 0.5$ the (genuine) midpoint rule and $0 < \vartheta < 1$ generalized implicit integrations (Artioli et al., 2007, p. 1829).

$$\boldsymbol{S}^j - \boldsymbol{S}^{j-1} = 2\mathcal{G}(\delta\boldsymbol{\varepsilon}^{\mathrm{dev},j} - \delta\boldsymbol{\varepsilon}^{p,j}) \tag{6.81}$$

$$\delta\boldsymbol{\varepsilon}^{p,j} = \sqrt{\tfrac{3}{2}}\delta\lambda\boldsymbol{n}^{\vartheta} \tag{6.82}$$

$$\boldsymbol{A}^j - \boldsymbol{A}^{j-1} = \delta\lambda\left(\sqrt{\tfrac{2}{3}}H_{ki}\boldsymbol{n}^{\vartheta} - H_{nl}\boldsymbol{A}^{\vartheta}\right) \tag{6.83}$$

$$\boldsymbol{n}^{\vartheta} := \frac{\boldsymbol{S}^{\vartheta} - \boldsymbol{A}^{\vartheta}}{\|\boldsymbol{S}^{\vartheta} - \boldsymbol{A}^{\vartheta}\|} \tag{6.84}$$

$$f^j = \sqrt{\tfrac{3}{2}}\|\boldsymbol{S}^j - \boldsymbol{A}^j\| - \sigma_Y^0 \leqslant 0 \qquad \delta\lambda \geqslant 0 \qquad f^j\delta\lambda = 0 \tag{6.85}$$

with

$$\boldsymbol{S}^{\vartheta} := \vartheta\boldsymbol{S}^j + (1-\vartheta)\boldsymbol{S}^{j-1} \tag{6.86}$$

$$\boldsymbol{A}^{\vartheta} := \vartheta\boldsymbol{A}^j + (1-\vartheta)\boldsymbol{A}^{j-1} \tag{6.87}$$

Based on the above midpoint integration rules, a method for the asymptotic response is formulated next, using the same choice on the trial stresses adopted, in (6.40), for the backward Euler integration.

Problem 2. Given: $\boldsymbol{S}^{\mathrm{trial}}$ and $\boldsymbol{A}^{\mathrm{trial}}$ as in (6.40) and (6.41).

Find: $\boldsymbol{S}$, $\boldsymbol{A}$, $\delta\lambda > 0$ and $\boldsymbol{n}^{\vartheta}$ such that

$$\boldsymbol{S}^{\mathrm{trial}} = \boldsymbol{S} + \sqrt{6}\mathcal{G}\delta\lambda\boldsymbol{n}^{\vartheta} \tag{6.88}$$

$$\boldsymbol{A} - \boldsymbol{A}^{\mathrm{trial}} = \delta\lambda\left(\sqrt{\tfrac{2}{3}}H_{ki}\boldsymbol{n}^{\vartheta} - H_{nl}\boldsymbol{A}^{\vartheta}\right) \tag{6.89}$$

$$\boldsymbol{n}^{\vartheta} := \frac{\boldsymbol{S}^{\vartheta} - \boldsymbol{A}^{\vartheta}}{\|\boldsymbol{S}^{\vartheta} - \boldsymbol{A}^{\vartheta}\|} \tag{6.90}$$

$$\boldsymbol{S}^{\vartheta} := \vartheta\boldsymbol{S} + (1-\vartheta)\boldsymbol{S}^{j-1} \tag{6.91}$$

$$\boldsymbol{A}^{\vartheta} := \vartheta\boldsymbol{A} + (1-\vartheta)\boldsymbol{A}^{\mathrm{trial}} \tag{6.92}$$

$$\sqrt{\tfrac{3}{2}}\|\boldsymbol{S} - \boldsymbol{A}\| = \sigma_Y^0 \tag{6.93}$$

The next section sketches how this system is solved by first computing $\delta\lambda$ as the least positive root of a tenth-degree polynomial. The remaining unknowns are

obtained using the following relations.

$$\boldsymbol{S}^{\vartheta,\text{trial}} := \vartheta \boldsymbol{S}^{\text{trial}} + (1-\vartheta)\boldsymbol{S}^{j-1} \tag{6.94}$$

$$V_\lambda := (1 + \vartheta H_{nl}\delta\lambda)^{-1} \tag{6.95}$$

$$\boldsymbol{\kappa}^\lambda := \boldsymbol{S}^{\vartheta,\text{trial}} - V_\lambda \boldsymbol{A}^{\text{trial}} \tag{6.96}$$

$$\boldsymbol{n}^\vartheta = \frac{\boldsymbol{\kappa}^\lambda}{\|\boldsymbol{\kappa}^\lambda\|} \tag{6.97}$$

$$\boldsymbol{S}^\vartheta = \boldsymbol{S}^{\vartheta,\text{trial}} - \sqrt{6}\vartheta G \delta\lambda \boldsymbol{n}^\vartheta \tag{6.98}$$

$$\boldsymbol{S} = \tfrac{1}{\vartheta}\left[\boldsymbol{S}^\vartheta - (1-\vartheta)\boldsymbol{S}^{j-1}\right] \tag{6.99}$$

$$\boldsymbol{A}^\vartheta = V_\lambda \boldsymbol{A}^{\text{trial}} + \sqrt{\tfrac{2}{3}}\vartheta H_{ki}\delta\lambda V_\lambda \boldsymbol{n}^\vartheta \tag{6.100}$$

Finally, the computation of the selected local updates follows

$$\delta\hat{\boldsymbol{\varepsilon}}^{p,j} = \sqrt{\tfrac{3}{2}}\delta\lambda \boldsymbol{n}^\vartheta \tag{6.101}$$

$$\hat{\boldsymbol{A}}^j = \tfrac{1}{\vartheta}\left[\boldsymbol{A}^\vartheta - (1-\vartheta)\boldsymbol{A}^{\text{trial}}\right] \tag{6.102}$$

$$\delta\hat{\boldsymbol{\beta}}^j = \tfrac{3}{2H_{ki}}(\hat{\boldsymbol{A}}^j - \boldsymbol{A}^{\text{trial}}) \tag{6.103}$$

It is not necessary to calculate $\boldsymbol{S}^\vartheta$ and $\boldsymbol{S}$ here because the stresses are only updated in the global stage (6.48) of the basic procedure BU.

The polynomial equation in the generalized midpoint integration

This section describes the equations and procedures (Artioli et al., 2007) used to solve Problem 2, given by (6.88-6.93).

Eliminating the unknown $\delta\boldsymbol{\varepsilon}^{p,j}$ from the system of equations (6.88-6.93), a system appears to be solved for the main unknowns $\delta\lambda > 0$, $\boldsymbol{S}$ and $\boldsymbol{A}$.

$$\boldsymbol{S}^{\text{trial}} = \boldsymbol{S} + \sqrt{6}G\delta\lambda\boldsymbol{n}^\vartheta \tag{6.104}$$

$$\boldsymbol{A} - \boldsymbol{A}^{\text{trial}} = \delta\lambda\left(\sqrt{\tfrac{2}{3}}H_{ki}\boldsymbol{n}^\vartheta - H_{nl}\boldsymbol{A}^\vartheta\right) \tag{6.105}$$

$$\boldsymbol{n}^\vartheta := \frac{\boldsymbol{S}^\vartheta - \boldsymbol{A}^\vartheta}{\|\boldsymbol{S}^\vartheta - \boldsymbol{A}^\vartheta\|} \tag{6.106}$$

$$\boldsymbol{S}^\vartheta := \vartheta\boldsymbol{S} + (1-\vartheta)\boldsymbol{S}^{j-1} \tag{6.107}$$

$$\boldsymbol{A}^\vartheta := \vartheta\boldsymbol{A} + (1-\vartheta)\boldsymbol{A}^{\text{trial}} \tag{6.108}$$

$$\sqrt{\tfrac{3}{2}}\|\boldsymbol{S} - \boldsymbol{A}\| = \sigma_Y^0 \tag{6.109}$$

The following paragraphs sketch the procedure to obtain a single equation for $\delta\lambda$.

Combining (6.104), (6.107) and (6.94), it follows that

$$\boldsymbol{S}^{\vartheta} = \boldsymbol{S}^{\vartheta,\text{trial}} - \sqrt{6}\vartheta G \delta\lambda \boldsymbol{n}^{\vartheta} \tag{6.110}$$

Likewise, from (6.105), (6.108) and (6.95) it comes

$$\boldsymbol{A}^{\vartheta} = V_\lambda \boldsymbol{A}^{\text{trial}} + \sqrt{\tfrac{2}{3}}\vartheta H_{ki}\delta\lambda V_\lambda \boldsymbol{n}^{\vartheta} \tag{6.111}$$

Furthermore, combining (6.110), (6.111), (6.96) and the definitions

$$\boldsymbol{\kappa}^{\vartheta} := \boldsymbol{S}^{\vartheta} - \boldsymbol{A}^{\vartheta} \tag{6.112}$$

$$Y_\lambda := \vartheta\delta\lambda\left(\sqrt{6}G + \sqrt{\tfrac{2}{3}}H_{ki}V_\lambda\right) \tag{6.113}$$

one obtains

$$\boldsymbol{\kappa}^{\lambda} = \boldsymbol{\kappa}^{\vartheta} + Y_\lambda \boldsymbol{n}^{\vartheta} \tag{6.114}$$

In the equation above, it holds that $\boldsymbol{\kappa}^{\vartheta} = \|\boldsymbol{\kappa}^{\vartheta}\|\boldsymbol{n}^{\vartheta}$, due to (6.106) and (6.112). Moreover, $Y_\lambda > 0$; hence, deducing from (6.114) that

$$\boldsymbol{n}^{\vartheta} = \frac{\boldsymbol{\kappa}^{\lambda}}{\|\boldsymbol{\kappa}^{\lambda}\|} \tag{6.115}$$

and $\|\boldsymbol{\kappa}^{\lambda}\| = \|\boldsymbol{\kappa}^{\vartheta}\| + Y_\lambda$.

Note that with

$$\boldsymbol{\kappa} := \boldsymbol{S} - \boldsymbol{A} \qquad \boldsymbol{\kappa}^{j-1} := \boldsymbol{S}^{j-1} - \boldsymbol{A}^{\text{trial}} \tag{6.116}$$

it holds

$$\boldsymbol{\kappa}^{\vartheta} = \vartheta\boldsymbol{\kappa} + (1-\vartheta)\boldsymbol{\kappa}^{j-1} \tag{6.117}$$

Now using (6.114), (6.115) and (6.117) to write

$$\vartheta\boldsymbol{\kappa} = \left(1 - \frac{Y_\lambda}{\|\boldsymbol{\kappa}^{\lambda}\|}\right)\boldsymbol{\kappa}^{\lambda} - (1-\vartheta)\boldsymbol{\kappa}^{j-1} \tag{6.118}$$

Finally, taking modulus and square both sides in (6.118), and also using (6.109), it is obtained the aimed scalar equation for the single variable $\delta\lambda$.

$$\left(1 - \frac{Y_\lambda}{\|\boldsymbol{\kappa}^{\lambda}\|}\right)^2 \|\boldsymbol{\kappa}^{\lambda}\|^2 + (1-\vartheta)^2\|\boldsymbol{\kappa}^{j-1}\|^2 - 2(1-\vartheta)\left(1 - \frac{Y_\lambda}{\|\boldsymbol{\kappa}^{\lambda}\|}\right)\boldsymbol{\kappa}^{j-1}\cdot\boldsymbol{\kappa}^{\lambda} - \tfrac{2}{3}\vartheta^2{\sigma_Y^0}^2 = 0 \tag{6.119}$$

It is still necessary to perform cumbersome substitutions in (6.119), and eliminate denominators containing $\delta\lambda$, to obtain explicit expressions for all the coefficients of the tenth-degree polynomial in $\delta\lambda$. Appendix C contains the detailed computation of the polynomial coefficients.

Finally, $\delta\lambda$ is the least positive root of the tenth-degree polynomial, computed by Laguerre's method.

6.7 Examples of application

For all examples, the following material constants are assumed: $E = 210\,\mathrm{GPa}$, $\nu = 0.3$, $H_{ki} = 280\,\mathrm{GPa}$, $H_{nl} = 1300$ and $\sigma_Y^0 = 225\,\mathrm{MPa}$.

This section describes the application of the algorithm ESS, defined in Section 6.5.2, with the parameters $\mathrm{tol}_{\mathrm{cyc}} = \mathrm{tol}_{\mathrm{step}} = 10^{-3}$ and $k_{\max} = 10$. For midpoint integration, it is adopted $\vartheta = 0.5$ unless mentioned otherwise.

6.7.1 Material ratcheting in tensile testing

The first example considers a material point obeying the AF rule and being cycled in uniaxial stress range $\sigma_x \in [\sigma_x^{\min}, \sigma_x^{\max}]$. Whenever the applied stress has non-zero mean value, the steady state solution results in material ratcheting.

Let $\bar{\sigma}_x := \sigma_x/\sigma_Y^0$, $\bar{A}_x := A_x/\sigma_Y^0$ and $\bar{h} := H_{ki}/(H_{nl}\sigma_Y^0)$ define nondimensional quantities.

Figure 6.2 displays the graph of the axial stress $\bar{\sigma}_x$ and backstress $\bar{A}_x$ versus the plastic strain ε_x^p. Without loss of generality, zero plastic strain at the start of the cycle is assumed; that is, $\varepsilon_x^p(0) = 0$ and thus $\Delta\varepsilon_x^p = \varepsilon_x^p(1)$ is the ratcheting plastic strain.

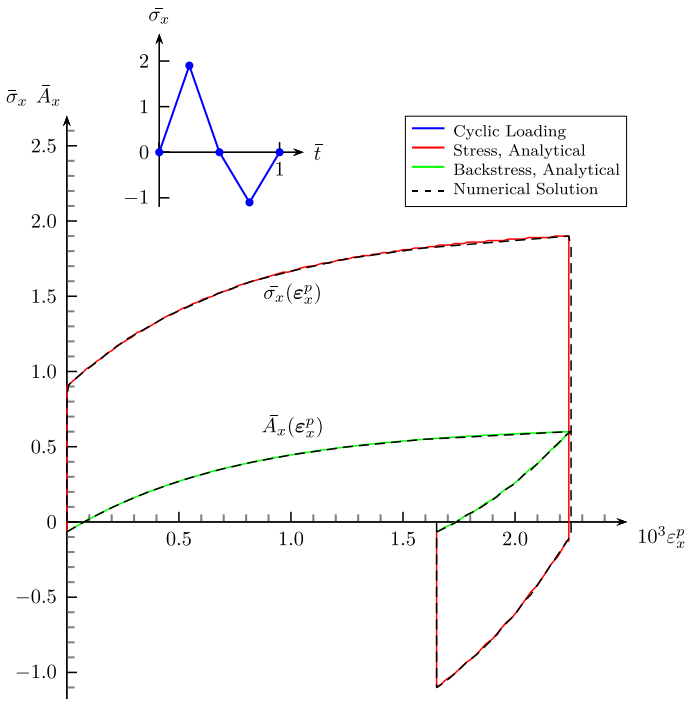

Figure 6.2: Material ratcheting with AF kinematic hardening. Numerical and analytical solutions for an imposed cyclic uniaxial stress $\bar{\sigma}_x$ in $[-1.1, 1.9]$.

As a reference, a summary of the results of a closed form integration of this problem appears in the following. First, from the loading data $\bar{\sigma}_x^{\min}$ and $\bar{\sigma}_x^{\max}$, the computation of the ratcheting plastic strain follows

$$\Delta\varepsilon_x^p = \frac{1}{H_{nl}} \ln \frac{(\bar{\sigma}_x^{\min} + 1)^2 - \bar{h}^2}{(\bar{\sigma}_x^{\max} - 1)^2 - \bar{h}^2} \tag{6.120}$$

and the peak values

$$\bar{A}_x^{\min} = \tfrac{2}{3}(\bar{\sigma}_x^{\min} + 1) \qquad \bar{A}_x^{\max} = \tfrac{2}{3}(\bar{\sigma}_x^{\max} - 1) \tag{6.121}$$

$$\varepsilon_x^{p,\max} = -\frac{1}{H_{nl}} \ln \frac{\bar{\sigma}_x^{\max} - 1 - \bar{h}}{\bar{\sigma}_x^{\min} + 1 - \bar{h}} \tag{6.122}$$

Then, for the plastic loading phase (Figure 6.2) $\varepsilon_x^p \in [0, \varepsilon_x^{p,\max}]$ and

$$\bar{A}_x(\varepsilon_x^p) = \tfrac{2}{3}\bar{h} + \left(\bar{A}_x^{\min} - \tfrac{2}{3}\bar{h}\right) \exp(-H_{nl}\varepsilon_x^p) \tag{6.123}$$

$$\bar{\sigma}_x(\varepsilon_x^p) = \tfrac{3}{2}\bar{A}_x(\varepsilon_x^p) + \sigma_Y^0 \tag{6.124}$$

For the plastic unloading phase, $\varepsilon_x^p \in [\Delta\varepsilon_x^p, \varepsilon_x^{p,\max}]$ and

$$\bar{A}_x(\varepsilon_x^p) = -\tfrac{2}{3}\bar{h} + \left(\bar{A}_x^{\max} + \tfrac{2}{3}\bar{h}\right) \exp\left[-H_{nl}(\varepsilon_x^{p,\max} - \varepsilon_x^p)\right] \tag{6.125}$$

$$\bar{\sigma}_x(\varepsilon_x^p) = \tfrac{3}{2}\bar{A}_x(\varepsilon_x^p) - \sigma_Y^0 \tag{6.126}$$

The numerical solution is obtained considering a cylinder under axial load and its discretization with mixed axisymmetric triangular finite elements (linear stress-quadratic displacement). The mesh in the meridian plane consists of a square divided into two triangles. Figure 6.2 shows numerical and analytical solutions for a repeated loading with $\bar{\sigma}_x$ in $[-1.1, 1.9]$.

This example demonstrates that the numerical method matches the analytical solution precisely. Next sections address the capability of this method for solving complex problems, where no analytical solution is available.

6.7.2 Tube under internal pressure

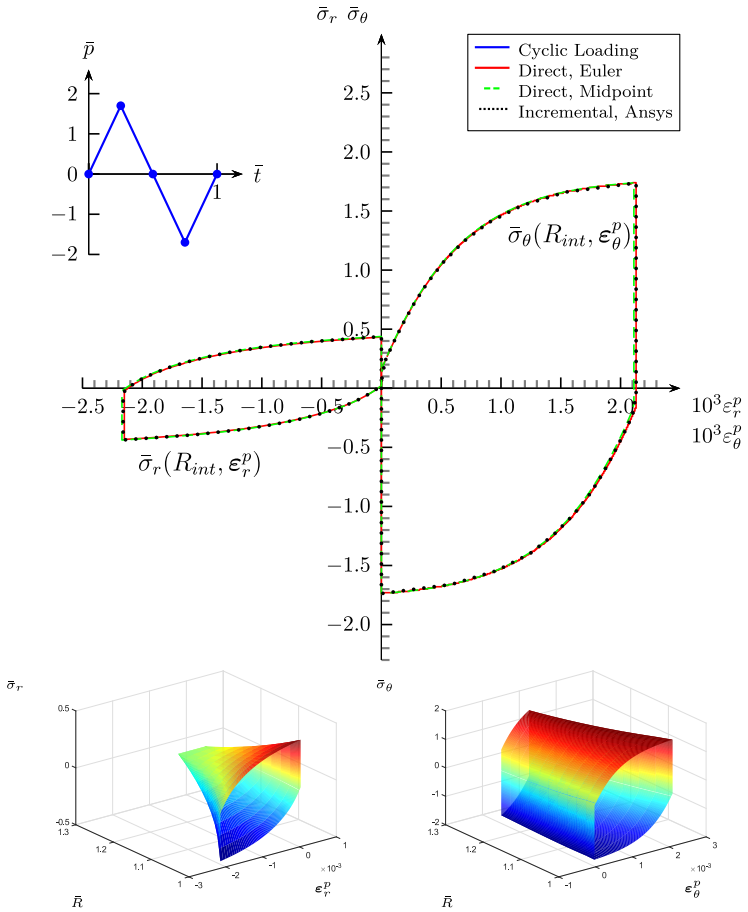

Figure 6.3: Stresses versus plastic strains for the tube under cyclic pressure $\bar{p}$ in $[-1.7, 1.7]$. (a) Direct and incremental steady state solutions for $\bar{\sigma}_r$ and $\bar{\sigma}_\theta$ at the internal surface. (b)-(c) Present solutions, $\bar{\sigma}_r(\bar{R}, \boldsymbol{\varepsilon}_r^p)$ and $\bar{\sigma}_\theta(\bar{R}, \boldsymbol{\varepsilon}_\theta^p)$, displayed across tube thickness.

The subsection considers a long thick closed tube, with $R_{\text{ext}} = 1.25R_{\text{int}}$ (R_{ext} and R_{int} are external and internal radii), submitted to a differential of pressure p (internal minus external), varying cyclically in the range $[p_{\min}, p_{\max}]$.

The nondimensional radial coordinate is denoted $\bar{R} := R/R_{\text{int}}$.

The nondimensional pressure is

$$\bar{p} := \frac{p}{p_{\text{ref}}} \qquad p_{\text{ref}} := \frac{2}{\sqrt{3}}\sigma_Y^0 \ln\left(\frac{R_{\text{ext}}}{R_{\text{int}}}\right) \tag{6.127}$$

with reference to the collapse pressure of a parent tube assumed elastic-ideally plastic and with yield stress σ_Y^0. The ultimate pressure for the tube

$$p_u = \frac{2}{\sqrt{3}}\left(\sigma_Y^0 + \frac{H_{ki}}{H_{nl}}\right) \ln\left(\frac{R_{\text{ext}}}{R_{\text{int}}}\right) \tag{6.128}$$

corresponds to the maximum Mises equivalent stress, $\sigma_Y^0 + \frac{H_{ki}}{H_{nl}}$, asymptotically reached with AF-hardening. For the assumed material $p_u = 1.957 p_{\text{ref}}$.

Nondimensional stresses are defined as follows

$$\bar{\sigma}_r := \frac{\sigma_r}{\sigma_Y^0} \qquad \bar{\sigma}_\theta := \frac{\sigma_\theta}{\sigma_Y^0} \qquad \bar{\sigma}_z := \frac{\sigma_z}{\sigma_Y^0} \tag{6.129}$$

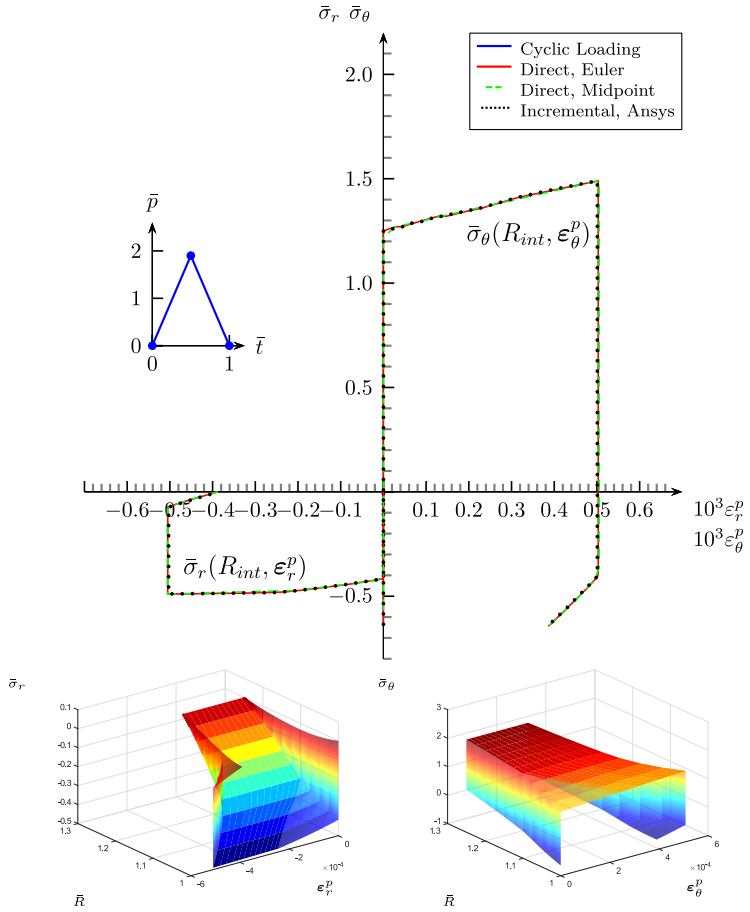

Figure 6.4: Stresses versus plastic strains for the tube under cyclic pressure $\bar{p}$ in $[0, 1.9]$. (a) Direct and incremental steady state solutions for $\bar{\sigma}_r$ and $\bar{\sigma}_\theta$ at the internal surface. (b)-(c) Present solutions, $\bar{\sigma}_r(\bar{R}, \boldsymbol{\varepsilon}^p_r)$ and $\bar{\sigma}_\theta(\bar{R}, \boldsymbol{\varepsilon}^p_\theta)$, displayed across tube thickness.

The mesh and boundary conditions used here are the same described in section 5.4.6.

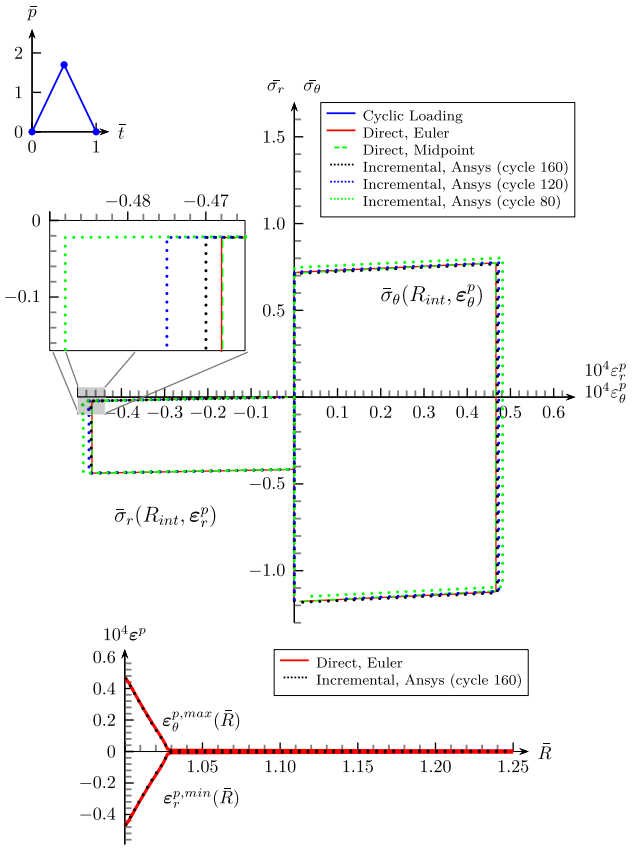

Figure 6.5: Stresses versus plastic strains for the tube under cyclic pressure $\bar{p}$ in $[0, 1.7]$. (a) Direct and incremental steady state solutions for $\bar{\sigma}_r$ and $\bar{\sigma}_\theta$ at the internal surface. (b) Extreme plastic strains during one steady cycle, across tube thickness.

Table 6.1: Computational times, in seconds, for the tube under cyclic pressure.

LR	$[\bar{p}_{\min}, \bar{p}_{\max}]$	Direct			Incremental
		Euler[a]	Euler[b]	Midpoint[c]	Ansys[d]
1	$[-1.7, 1.7]$	211	52	16	86
2	$[0, 1.9]$	68	36	4	2229
3	$[0, 1.7]$	526	136	12	13021

(a) Reference direct solution (RDS): 4000 time steps for first load range (LR1) and 2000 for LR2 and LR3

(b) RDS ±0.7%: 1000 time steps for LR1 and LR2, 500 time steps for LR3

(c) RDS ±0.6%: 120 time steps for LR1, 60 for LR2 and 38 for LR3

(d) RDS ±1.5% 10 substeps per cycle for LR1 and 200 for LR2 and LR3

The responses to three loading programs, with pressure ranges within ultimate limits, are evaluated in the following.

The first range, $[-1.7p_{\text{ref}}, 1.7p_{\text{ref}}]$, results in alternating plasticity (Figure 6.3).

Ratcheting occurs for the second range, $[0, 1.9p_{\text{ref}}]$ (Figure 6.4). In both cases the entire tube thickness undergoes plastic deformations during the steady state cycle.

The third case, with pressure varying in $[0, 1.7p_{\text{ref}}]$, results in alternating plasticity, restricted to a core region adjacent to the interior surface of the tube (Figure 6.5).

Results of our direct procedure are checked against incremental solutions generated by Ansys (Figures 6.3 to 6.5). The same model is cycled, performing true incremental integration in Ansys, and applying fictitious cycles in the present algorithm, until the stabilized solutions are obtained to the same prescribed tolerance. Note that the finite elements and the integration scheme are different in the present procedure and in Ansys.

For all cases evaluated (Figures 6.3 to 6.5) the differences in stabilized results are marginal.

Table 6.1 presents CPU times for the load ranges named LR1, LR2 and LR3. The first column of times, labeled Euler^a, corresponds to the reference direct solutions (RDS), obtained with very small time steps and backward Euler integration. With respect to this reference solution, the footnote of Table 6.1 gives the deviation of the other solutions at a representative point. For instance, when the note says that "RDS $\pm 0.7\%$" holds for the column labeled Euler^b, it means that the convergence indicator deviates from RDS less than $\pm 0.7\%$, when computed for LR1, LR2 and LR3. We choose the maximum plastic strain increment in a cycle, at the internal surface, as the indicator for convergence.

The relevant remark on the results in Table 6.1 is that the time spent in the incremental method is always significantly greater than the time consumed in the direct procedure. This is the main justification for the present algorithm.

6.7.3 Holed plate in plane strain

This subsection assesses the cyclic response of a holed square plate in plane strain conditions and submitted to uniaxial lateral loading. The hole has diameter $D = 0.2L$, where L is the edge length.

The loading $\bar{p} := p/\sigma_Y^0$ and the boundary conditions are depicted in Figure 6.6. The mesh has 1152 triangles and 2405 nodes. It uses second order plane strain elements with mixed formulations, described in Zouain et al. (2014). The same mesh is adopted in Ansys, with standard kinematical second order triangular elements.

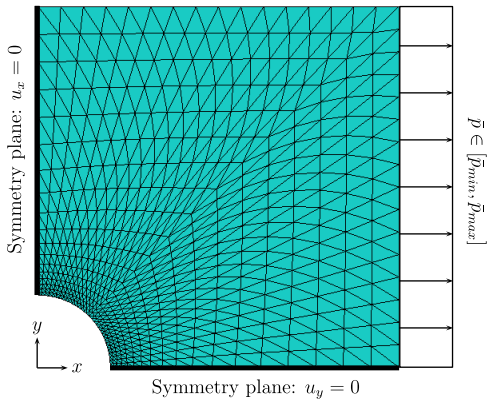

Figure 6.6: Plane strain finite element model of the holed plate.

Two load ranges are evaluated.

Figure 6.7 summarizes results from incremental and direct methods for the load range with $\bar{p}$ in $[-0.5, 1.2]$. The focus is the maximum increment, in a cycle, of the plastic strain component in the direction coincident with the load (x-axis). This particular result is important due to its relation with the fatigue life of the plate.

Figure 6.8 shows results for the second load range, with $\bar{p}$ in $[-0.3, 1.6]$. Here, when using midpoint integration, we set $\vartheta = 0.75$ to avoid numerical instability. For this loading, ratcheting becomes significant near the north position of the hole. Accordingly, this is a case of structural ratcheting.

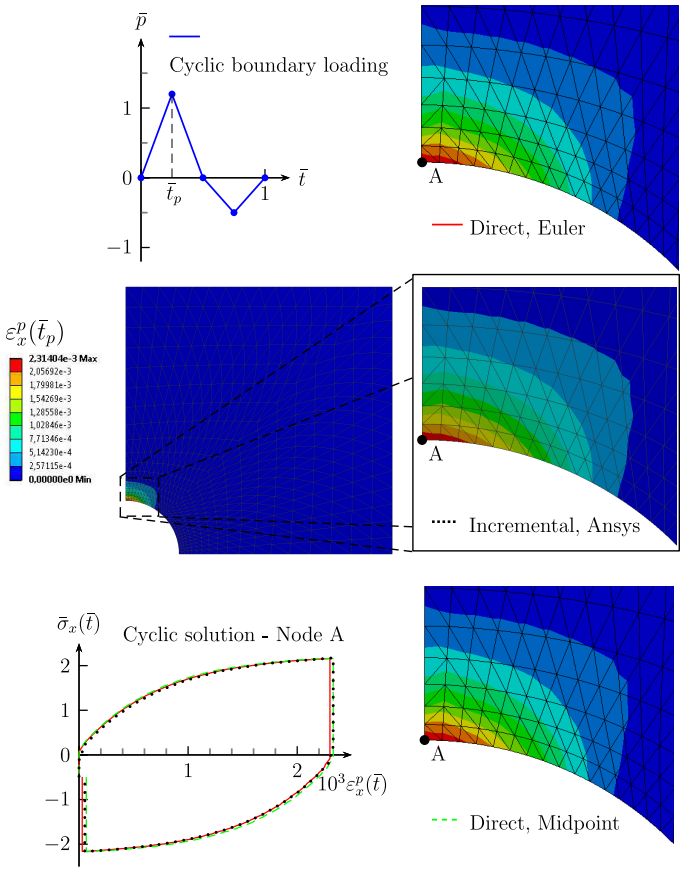

Figure 6.7: Direct and incremental asymptotic solutions for the plate at the upper point of the hole (A), under a cyclic loading $\bar{p}$ in $[-0.5, 1.2]$. The contour plots show the strain range $\varepsilon_x^p(\bar{t}_p)$ in a steady-state cycle.

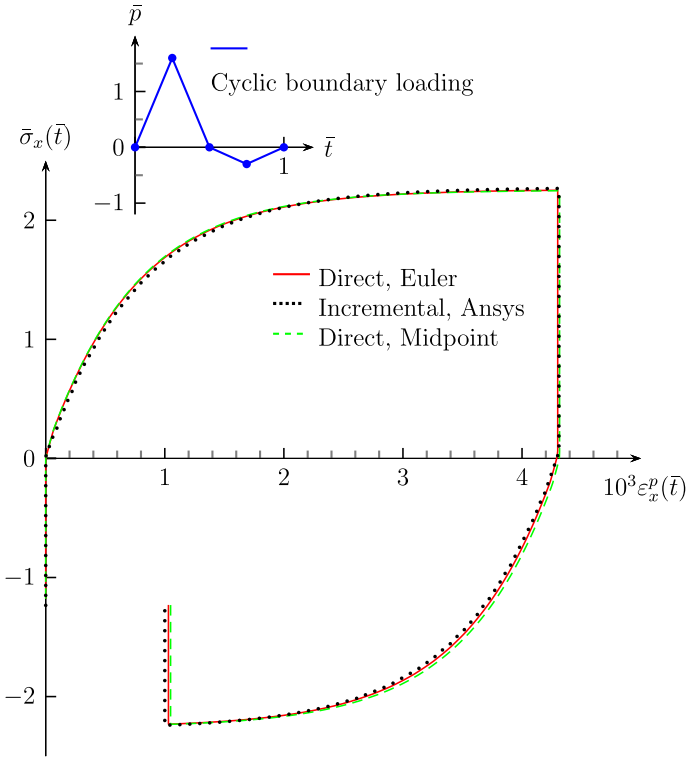

Figure 6.8: Direct and incremental asymptotic solutions for the plate at the upper point of the hole (A in Figure 6.7), under a cyclic loading $\bar{p}$ in $[-0.3, 1.6]$.

For both load cases, differences between direct and incremental solutions are marginal. It is remarked that the finite element interpolations used in the direct and incremental computations are different, as well as the discrete time integration.

Times shown in Table 6.2 demonstrate that the direct method performed much faster than the true incremental procedure (with similar tolerances). For the second range the direct solution with backward Euler integration is 12 times faster than the incremental procedure. In all load cases and for both integration schemes, it is at least 9 times faster.

Table 6.2: Computational times, in seconds, for the holed plate.

LR	$[\bar{p}_{\min}, \bar{p}_{\max}]$	Direct		Incremental
		Euler[a]	Midpoint[b]	Ansys[c]
1	$[-0.5, 1.2]$	457	463	4195
2	$[-0.3, 1.6]$	1572	2196	19117

(a) 200 time steps for LR1 and 400 for LR2

(b) 200 time steps for LR1 and 400 for LR2

(c) 40 substeps per cycle for LR1 and 400 for LR2

Chapter 7

Conclusions

Chapter 4 describes a procedure for the direct computation of the asymptotic response of elastoplastic solids submitted to cyclic loadings. The algorithm is robust and fast, as was demonstrated in section 4.7.

The approach does not introduce any additional approximations or constraints, besides the time and space discretization usually adopted in incremental elastoplastic analyses. Specifically, it uses the implicit (backward Euler) approximation of the plastic strain evolution relation and a true closest point projection. This implies that the direct and incremental converged approximations are exactly equal whenever the finite element interpolation and time discretization coincide.

The special trial stress (4.40) for the closest point projection performed in the algorithm is based on the direct formulation of the asymptotic problem. This essential component of the procedure proved to be efficient for inducing convergence.

Robustness of the algorithm, meaning good rate of successful convergence, was experimentally investigated with respect to the qualitative different critical scenarios of alternating plasticity and simple or combined incremental collapse. The observed behavior was robust for all types of cyclic response. This statement is strictly based on the limited scope of applications shown in the thesis, although some other applications have been run with similar results. Concerning this issue, it is worth to point out that many usual elastoplastic incremental procedures may undergo convergence difficulties because, for instance, of an inappropriate time discretization and that this effect may appear in the proposed direct approach. Finally, there is no assumption in the formulation suggesting a selective convergence limitation.

In chapter 5, the author presents a novel direct method to identify structural ratchet boundaries for elastoplastic solids under periodic loading programs.

The method is devised in a general framework of elastoplasticity where the presence of a sustained load is non-mandatory. Moreover, the method allows the analyst to choose any of the loads to amplify. No restriction applies on the number of different prescribed loads. In other words, the ratchet boundary is not restricted to

be a curve in a bidimensional Bree-like interaction diagram. In this capability, the approach is similar to the procedure for shakedown described in Simon and Weichert (2012) for shakedown analysis with multi-dimensional loading spaces.

Through comparison with analytical and numerical benchmark solutions, the thesis assessed the proposed procedure under several circumstances. Namely, (i) uniaxial and multi-axial stress states; (ii) linear and non-linear spatial stress distributions; (iii) non-proportional and proportional loading programs; (iv) bidimensional and multi-dimensional loading spaces.

In view of the above mentioned features, the proposed method constitutes an enhanced alternative approach to other previously developed direct methods.

In an industrial application example, on a printed circuit exchanger model, the method demonstrates precision by comparison with the standard numerical iterative solutions. The improvements in computational performance became evident, with the method being at least 80 times faster than step-by-step integration.

All the algorithms described here are written in terms of general linear elasticity and associated ideal plasticity, although only applications adopting the Mises model of plasticity are shown. In Zouain and SantAnna (2018) (chapter 6) it is constructed an extension for the solver ESS, which computes one steady-state response, when the material model is nonlinear kinematic hardening plasticity. Using such extensions the present method can be applied to other constitutive behaviors.

Chapter 6 describes an upgrade in the direct method to compute the cyclic response of a solid that allows the use of nonlinear kinematic hardening. This is the first direct approach for the steady state elastoplastic problem with nonlinear kinematic hardening. This capability is important to model material ratcheting.

Again, the algorithm performed much faster than an incremental stabilized procedure in some typical applications. Tables 6.1 and 6.2 show CPU times at least nine times faster than the incremental solution of the tube under periodic pressure and the holed plate submitted to cyclic traction. These rapid responses are perhaps the main justification for developing a direct method.

The algorithm ESS, formalized in Section 6.5.2, basically consists of alternate updates of the plastic strain increments, by a particular projection scheme, and the residual stresses, by using the fixed influence (residual) operator relating residual stresses to inelastic strains. The special return mapping defined by (6.43-6.47) is the key component of the method. In the case of AF nonlinear kinematical hardening, the integration approach becomes important to the efficiency of the procedure. This issue required the implementation and testing of various alternative integration techniques. To this respect, the conclusion drawn from the examples is that the direct method is much faster than incremental procedures, regardless of the integration schemes adopted.

The proposed method does not include any supplementary approximation or simplification other than the standard discretization by the finite element method.

The fact that the Armstrong-Frederick hardening model is non-associated significantly lessen the theoretical results concerning existence of cyclic solutions and convergence of incremental solutions to cyclic responses. Nevertheless, computational experience in step-by-step integration indicates that convergence is the rule. In this regard, the procedure, giving verifiable converged cyclic solutions, may be a useful computational tool to address this issue.

In summary, the main contributions of the research are:

(i) The development of a direct method to compute the asymptotic steady-state solution in ideal elastoplasticity. Validation examples show that the method is fast and accurate. The performance ranges from one to two orders of magnitude higher than incremental analysis.

(ii) The performance allowed the development of a direct strategy to identify the structural ratchet-limit. The procedure applies to periodical loads and has no limitations on the number of applied loads.

(iii) The upgrade of the asymptotic solution method with nonlinear kinematic hardening, which is required to model the Baushinger effect and material ratcheting. To the author knowledge, this is the first direct method for steady-state solution with this capability. Comparison with step-by-step solutions shows a increase in performance of one order of magnitude, at least.

Future research

The author indicates some future research topics related to the developments of the thesis. (i) The use of the direct procedure to numerically reproduce experimental data and to evaluate the sensibility to material hardening parameters; (ii) the implementation of the procedures described herein in a commercial finite element software, to amplify its industrial usage; (iii) the application of the direct procedure to identify shakedown and ratchet limits with non-linear hardening material.

Bibliography

Abdel-Karim, M., 2005. Shakedown of complex structures according to various hardening rules. International Journal of Pressure Vessels and Piping 82 (6), 427–458.

Abou-Hanna, J., McGreevy, T. E., 2011. A simplified ratcheting limit method based on limit analysis using modified yield surface. International Journal of Pressure Vessels and Piping 88, 11–18.

Adibi-Asl, R., Reinhardt, W., 2011a. Non-cyclic shakedown/ratcheting boundary determination - Part 1: Analytical approach. International Journal of Pressure Vessels and Piping 88, 311–320.

Adibi-Asl, R., Reinhardt, W., 2011b. Non-cyclic shakedown/ratcheting boundary determination - Part 2: Numerical implementation. International Journal of Pressure Vessels and Piping 88, 321–329.

Ahn, Y. J., Bertocchi, E., Barber, J., 2008. Shakedown of coupled two-dimensional discrete frictional systems. Journal of the Mechanics and Physics of Solids 56 (12), 3433–3440.

Armero, F., 2018. Elastoplastic and viscoplastic deformations in solids and structures. In: Encyclopedia of Computational Mechanics, 2nd Edition. Wiley Online Library, pp. 1–41.

Armstrong, P. J., Frederick, C., 1966. A mathematical representation of the multiaxial Bauschinger effect. Vol. 731. Central Electricity Generating Board [and] Berkeley Nuclear Laboratories, Research & Development Department Berkeley.

Artioli, E., Auricchio, F., da Veiga, L. B., 2007. Second-order accurate integration algorithms for von-mises plasticity with a nonlinear kinematic hardening mechanism. Computer Methods in Applied Mechanics and Engineering 196 (9-12), 1827–1846.

Auricchio, F., Taylor, R. L., 1995. Two material models for cyclic plasticity: nonlinear kinematic hardening and generalized plasticity. International Journal of Plasticity 11 (1), 65–98.

Bari, S., Hassan, T., 2002. An advancement in cyclic plasticity modeling for multiaxial ratcheting simulation. International Journal of Plasticity 18 (7), 873–894.

Bodovillé, G., de Saxcé, G., 2001. Plasticity with non-linear kinematic hardening: modelling and shakedown analysis by the bipotential approach. European Journal of Mechanics-A/Solids 20 (1), 99–112.

Bouby, C., Kondo, D., De Saxcé, G., 2015. A comparative analysis of two formulations for non linear hardening plasticity models: Application to shakedown analysis. European Journal of Mechanics-A/Solids 53, 48–61.

Bradford, R. A. W., 2012. The bree problem with primary load cycling in-phase with the secondary load. International Journal of Pressure Vessels and Piping 99-100, 44–50.

Bradford, R. A. W., 2015. Solution of the ratchet-shakedown bree problem with an extra orthogonal primary load. International Journal of Pressure Vessels and Piping 129-130, 32–42.

Bradford, R. A. W., 2017. The bree problem with the primary load cycling out-of-phase with the secondary load. International Journal of Pressure Vessels and Piping 154, 83–94.

Bree, J., 1967. Elastic-plastic behavior of thin tubes subjected to internal pressure and intermittent high-heat fluxes with application to fast-nuclear-reactor fuel elements. The Journal of Strain Analysis for Engineering Design 2, 226–238.

Bree, J., 1989. Plastic deformation of a closed tube due to interaction of pressure stresses and cyclic thermal stresses. International Journal of Mechanical Sciences 31, 865–872.

Carter, P., 2005a. Analysis of cyclic creep and rupture. Part 1: Bounding theorems and cyclic reference stresses. International Journal of Pressure Vessels and Piping 82 (1), 15–26.

Carter, P., 2005b. Analysis of cyclic creep and rupture. Part 2: Calculation of cyclic reference stresses and ratcheting interaction diagrams. International Journal of Pressure Vessels and Piping 82 (1), 27–33.

Chaboche, J., 2008. A review of some plasticity and viscoplasticity constitutive theories. International Journal of Plasticity 24 (10), 1642–1693.

Chaboche, J.-L., 1991. On some modifications of kinematic hardening to improve the description of ratchetting effects. International journal of plasticity 7 (7), 661–678.

Chelminski, K., 2003. Mathematical analysis of the armstrong-frederick model from the theory of inelastic deformations of metals. first results and open problems. Continuum Mechanics and Thermodynamics 15 (3), 221–245.

Chełmiński, K., Neff, P., Owczarek, S., 2015. A first regularity result for the armstrong–frederick cyclic hardening plasticity model with cosserat effects. Journal of Mathematical Analysis and Applications 423 (1), 283–304.

Chen, H., Ponter, A. R., 2001. A method for the evaluation of a ratchet limit and the amplitude of plastic strain for bodies subjected to cyclic loading. European Journal of Mechanics - A/Solids 20, 555–571.

Chen, H., Ponter, A. R., 2010. A direct method on the evaluation of ratchet limit. Journal of Pressure Vessel Technology 132, 1–8.

Comi, C., Maier, G., Perego, U., 1992. Generalized variable finite element modeling and extremum theorems in stepwise holonomic elastoplasticity with internal variables. Computer Methods in Applied Mechanics and Engineering 96 (2), 213–237.

De Angelis, F., Taylor, R. L., 2016. A nonlinear finite element plasticity formulation without matrix inversions. Finite Elements in Analysis and Design 112, 11–25.

de Borst, R., Crisfield, M. A., Remmers, J. J., Verhoosel, C. V., et al., 2012. Nonlinear finite element analysis of solids and structures. John Wiley & Sons.

de Saxcé, G., Tritsch, J.-B., Hjiaj, M., 2000. Shakedown of elastic-plastic structures with non linear kinematical hardening by the bipotential approach. In: Inelastic analysis of structures under variable loads. Springer, pp. 167–182.

de Souza Neto, E. A., Peric, D., Owen, D. R. J., 2008. Computational Methods for Plasticity Theory and Applications, 1st Edition. Wiley.

Dettmer, W., Reese, S., 2004. On the theoretical and numerical modelling of armstrong–frederick kinematic hardening in the finite strain regime. Computer Methods in Applied Mechanics and Engineering 193 (1-2), 87–116.

Felippa, C. A., 2004. Introduction to Finite Element Methods. Department of Aerospace Engineering Sciences and Center for Aerospace Structures University of Colorado, Boulder, Colorado 80309-0429, USA.

Francfort, G. A., Stefanelli, U., 2013. Quasi-static evolution for the armstrong–frederick hardening-plasticity model. Applied Mathematics Research eXpress 2013 (2), 297–344.

Frederick, C., Armstrong, P., 1966. Convergent internal stresses and steady cyclic states of stress. Journal of Strain Analysis 1 (2), 154–159.

Gokhfeld, D. A., Charniavsky, O., 1980. Limit analysis of structures at thermal cycling. Vol. 4. Springer Science & Business Media.

Halphen, B., 2005. Elastic perfectly plastic structures with temperature dependent elastic coefficients. Comptes Rendus Mécanique 333 (8), 617–621.

Halphen, B., Nguyen, Q. S., 1975. Sur les matériaux standard généralisés. Journal de mécanique 14, 39–63.

Hassan, T., Taleb, L., Krishna, S., 2008. Influence of non-proportional loading on ratcheting responses and simulations by two recent cyclic plasticity models. International Journal of Plasticity 24 (10), 1863–1889.

Hubel, H., 1996. Basic conditions for material and structural ratcheting. Nuclear Engineering and Design 162, 55–65.

Iserles, A., 2009. A first course in the numerical analysis of differential equations. No. 44. Cambridge university press.

Jappy, A., Mackenzie, D., Chen, H., 2013a. A fully implicit, lower bound, multiaxial solution strategy for direct ratchet boundary evaluation: implementation and comparison. Journal of Pressure Vessel Technology, 136.

Jappy, A., Mackenzie, D., Chen, H., 2013b. A fully implicit, lower bound, multiaxial solution strategy for direct ratchet boundary evaluation: theoretical development. Journal of Pressure Vessel Technology, 135.

Jiang, Y., Sehitoglu, H., 1996. Modeling of cyclic ratchetting plasticity, part i: development of constitutive relations. Journal of Applied Mechanics 63 (3), 720–725.

Jirásek, M., Bazant, Z. P., 2002. Inelastic analysis of structures. John Wiley & Sons.

Kachanov, L. M., 2004. Foundations of the theory of plasticity, dover Edition. Dover Publications, New York.

Kalnins, A., Rudolph, J., 2011. Global Ratcheting by Elastic-Plastic FEA According to ASME Section VIII Rules. In: ASME 2011 Pressure Vessels and Piping Conference. American Society of Mechanical Engineers, pp. 599–606.

Khutia, N., Dey, P. P., Hassan, T., 2015. An improved nonproportional cyclic plasticity model for multiaxial low-cycle fatigue and ratcheting responses of 304 stainless steel. Mechanics of Materials 91, 12–25.

Koiter, W. T., 1956. A new general theorem on shakedown of elastic-plastic structures. In: Proceedings of the Koninklijke Nederlandse Akademie van Wetenschappen. Vol. B.59. pp. 24–34.

König, J. A., 1987. Shakedown of Elastic-Plastic Structures, 1st Edition. Elsevier, New York.

König, J. A., Maier, G., 1981. Shakedown analysis of elastoplastic structures: a review of recent developments. Nuclear engineering and design 66 (1), 81–95.

Krabbenhøft, K., Lyamin, A., Sloan, S., 2007a. Formulation and solution of some plasticity problems as conic programs. International Journal of Solids and Structures 44, 1533–1549.

Krabbenhøft, K., Lyamin, A., Sloan, S., Wriggers, P., 2007b. An interior-point algorithm for elastoplasticity. International Journal for Numerical Methods in Engineering 69 (3), 592–626.

Krishna, S., Hassan, T., Naceur, I. B., Saï, K., Cailletaud, G., 2009. Macro versus micro-scale constitutive models in simulating proportional and nonproportional cyclic and ratcheting responses of stainless steel 304. International Journal of Plasticity 25 (10), 1910–1949.

Lee, Y., Lee, J. I., 2014. Structural assessment of intermediate printed circuit heat exchanger for sodium-cooled fast reactor with supercritical co2 cycle. Annals of Nuclear Energy 73, 84–95.

Lemaitre, J., Chaboche, J.-L., 1994. Mechanics of solid materials. Cambridge university press.

Lubliner, J., 2008. Plasticity theory. Courier Corporation.

Lytwyn, M., Chen, H., Martin, M., 2015a. Comparison of the linear matching method to rolls-royce's hierarchical finite element framework for ratchet limit analysis. International Journal of Pressure Vessels and Piping 125, 13–22.

Lytwyn, M., Chen, H., Ponter, A. R. S., 2015b. A generalised method for ratchet analysis of structures undergoing arbitrary thermo-mechanical load histories. International Journal for Numerical Methods in Engineering 104 (2), 104–124.

Maier, G., 1970. A minimum principle for incremental elastoplasticity with non-associated flow laws. Journal of the Mechanics and Physics of Solids 18 (5), 319–330.

Maitournam, M. H., Pommier, B., Thomas, J.-J., 2002. Détermination de la réponse asymptotique d'une structure anélastique sous chargement thermomécanique cyclique. Comptes Rendus Mecanique 330 (10), 703–708.

Makrodimopoulos, A., Martin, C., 2007. Upper bound limit analysis using simplex strain elements and second-order cone programming. International journal for numerical and analytical methods in geomechanics 31 (6), 835–865.

Martin, M., 2008. Application of direct cyclic analysis to the prediction of plastic shakedown of nuclear power plant components. In: Pressure Vessels and Piping. Chicago, Illinois.

Martin, M., Rice, D., 2009. A hybrid procedure for ratchet boundary prediction. In: ASME Pressure Vessels and Piping Conference Volume 1: Codes and Standards. , Prague, Czech Republic, pp. 81–88.

Maugin, G., A., 1992. The thermomechanics of plasticity and fracture, 1st Edition. Cambridge University Press, Cambridge.

Melan, E., 1938. Der spannungszustand eines mises-henckychen kontinuums bei veraenderlicher. Sitzber, Ak. Wiss. Wien IIa 147, 73–78.

Natesan, K., Moisseytsev, A., Majumdar, S., 2009. Preliminary issues associated with the next generation nuclear plant intermediate heat exchanger design. Journal of Nuclear Materials 392 (2), 307–315.

Natesan, K., Moisseytsev, A., Majumdar, S., Shankar, P. S., 2006. Preliminary issues associated with the next generation nuclear plant intermediate heat

exchanger design. Tech. Rep. ANL/EXT-06/46, Nuclear Engineering Division, Argonne National Laboratory for U.S. Department of Energy Office of Nuclear Energy, Science, and Technology.

Ng, H., Moreton, D., 1986. Ratchetting rates for a bree cylinder subjected to in-phase and out-of-phase loading. Journal of Strain Analysis for Engineering Design 21, 1–7.

Ohno, N., Wang, J.-D., 1993. Kinematic hardening rules with critical state of dynamic recovery, part I: formulation and basic features for ratchetting behavior. International Journal of Plasticity 9 (3), 375–390.

Panagiotou, K., Spiliopoulos, K., 2016. Assessment of the cyclic behavior of structural components using novel approaches. Journal of Pressure Vessel Technology 138 (4), 041201.

Peigney, M., 2014. Shakedown of elastic-perfectly plastic materials with temperature-dependent elastic moduli. Journal of the Mechanics and Physics of Solids 71, 112–131.

Peigney, M., Stolz, C., 2003. An optimal control approach to the analysis of inelastic structures under cyclic loading. Journal of the Mechanics and Physics of Solids 51 (4), 575–605.

Polizzotto, C., 1993a. A study on plastic shakedown of structures: Part I - Basic Properties. Journal of Applied Mechanics 60, 318–323.

Polizzotto, C., 1993b. A study on plastic shakedown of structures: Part II - Theorems. Journal of Applied Mechanics 60, 324–330.

Polizzotto, C., 1994a. On elastic plastic structures under cyclic loads. European Journal of Mechanics A/Solids 13 (4), 146–173.

Polizzotto, C., 1994b. Steady states and sensitivity analysis in elastic-plastic structures subjected to cyclic loads. International journal of solids and structures 31 (7), 953–970.

Polizzotto, C., 2003. Variational methods for the steady state response of elastic–plastic solids subjected to cyclic loads. International journal of solids and structures 40 (11), 2673–2697.

Polizzotto, C., Borino, G., 1996. Shakedown and steady-state responses of elastic-plastic solids in large displacements. International journal of solids and structures 33 (23), 3415–3437.

Ponter, A. R., Chen, H., 2001. A minimum theorem for cyclic load in excess of shakedown, with application to the evaluation of a ratchet limit. European Journal of Mechanics-A/Solids 20 (4), 539–553.

Pycko, S., 1997. A cycle-oriented incremental analysis of shakedown problems. International journal for numerical methods in engineering 40 (17), 3163–3179.

Rahman, S. M., Hassan, T., Corona, E., 2008. Evaluation of cyclic plasticity models in ratcheting simulation of straight pipes under cyclic bending and steady internal pressure. International Journal of Plasticity 24 (10), 1756–1791.

Reinhardt, W., 2003. Distinguishing ratcheting and shakedown conditions in pressure vessels. In: ASME 2003 Pressure Vessels and Piping Conference. American Society of Mechanical Engineers, pp. 13–26.

Reinhardt, W., 2008a. A non-cyclic method for plastic shakedown analysis. Journal of Pressure Vessel Technology 130 (3), 031209.

Reinhardt, W., 2008b. On the interaction of thermal membrane and thermal bending stress in shakedown analysis. In: ASME 2008 Pressure Vessels and Piping Conference. American Society of Mechanical Engineers, pp. 811–822.

Rohart, P., Panier, S., Simonet, Y., Hariri, S., Afzali, M., 2015. A review of state-of-the-art methods for pressure vessels design against progressive deformation. Journal of Pressure Vessel Technology 137 (5), 051202.

Rudolph, J., Kalnins, A., Gotz, A., Hilpert, R., 2011. Local ratcheting by elastic-plastic FEA: Criteria and Code Based Approaches. In: ASME 2011 Pressure Vessels and Piping Conference. American Society of Mechanical Engineers, pp. 617–627.

SantAnna, R., Zouain, N., 2018. A direct method for ratchet boundary determination, Submitted.

Schenk, O., Gärtner, K., 2004. Solving unsymmetric sparse systems of linear equations with pardiso. Future Generation Computer Systems 20 (3), 475–487.

Shen, J., Chen, H., Liu, Y., 2018. A new four-dimensional ratcheting boundary: Derivation and numerical validation. European Journal of Mechanics - A/Solids 71, 101–112.

Simo, J. C., Hughes, T. J., 2006. Computational inelasticity. Vol. 7. Springer Science & Business Media.

Simon, J.-W., Weichert, D., 2012. Shakedown analysis with multidimensional loading spaces. Comput. Mech. 49 (4), 477–485.

Spiliopoulos, K. V., Panagiotou, K. D., 2012. A direct method to predict cyclic steady states of elastoplastic structures. Computer Methods in Applied Mechanics and Engineering 223, 186–198.

Tereshin, D. A., Cherniavsky, O. F., 2015. Theoretical basis and a finite element formula for the direct calculation of steady plastic states. In: Direct Methods for Limit and Shakedown Analysis of Structures. Springer, pp. 81–103.

Ure, J., Chen, H. F., Li, T., Chen, W., Tipping, D., Mackenzie, D., 2011. A direct method for the evaluation of lower and upper bound ratchet limits. Procedia Engineering 10, 356–361.

Varvani-Farahani, A., Nayebi, A., 2018. Ratcheting in pressurized pipes and equipment: A review on affecting parameters, modelling, safety codes, and challenges. Fatigue & Fracture of Engineering Materials & Structures 41 (3), 503–538.

Zheng, X., Peng, H., Yu, J., Wang, W., Lin, W., Xu, J., 2017. Analytical ratchet limit for pressurized pipeline under cyclic nonproportional loadings. Journal of Pipeline Systems Engineering and Practice 8 (3), 04017002.

Zheng, X. T., Peng, H. Y., Yu, J. Y., Wang, G. G., Lin, W., Xu, J., 2015. Ratcheting limit for pressurized pipes under biaxial loadings. Procedia Engineering 130, 1215–1223.

Zouain, N., 2018. Shakedown and safety assessment. In: Encyclopedia of Computational Mechanics, 2nd Edition. John Wiley & Sons.

Zouain, N., Borges, L., Silveira, J. L., 2014. Quadratic velocity-linear stress interpolations in limit analysis. International Journal for Numerical Methods in Engineering 98 (7), 469–491.

Zouain, N., Borges, L. A., Silveira, J. L., 2002. An algorithm for shakedown analysis with nonlinear yield functions. Computer Methods in Applied Mechanics and Engineering 191, 2463–2481.

Zouain, N., SantAnna, R., 2017. Computational formulation for the asymptotic response of elastoplastic solids under cyclic loads. European Journal of Mechanics-A/Solids 61, 267–278.

Zouain, N., SantAnna, R., 2018. Computing the asymptotic cyclic response of elastoplastic solids with nonlinear kinematic hardening. European Journal of Mechanics - A/Solids 72, 120–134.

Zouain, N., Silveira, J. L., 2001. Bounds to shakedown loads. International Journal of Solids and Structures 38 (10-13), 2249–2266.

Appendix A

Residual operator and shakedown

A.1 Elastic-ideally plastic model

Due to virtual power principle, the following stress decomposition applies

$$\boldsymbol{\sigma}(t) = \boldsymbol{\sigma}^E(t) + \boldsymbol{\sigma}^r(t). \tag{A.1}$$

The flow law is associated, so the plastic strain rate follows

$$\boldsymbol{d}^p(t) \ \in \ \mathcal{N}_p. \tag{A.2}$$

In addition, the residual operator maps plastic strains to residual stress through

$$\boldsymbol{\sigma}^r(t) = \boldsymbol{\mathcal{Z}}\boldsymbol{\varepsilon}^p(t). \tag{A.3}$$

Shakedown occurs if

$$\int_0^{t^*} \int_{\mathcal{B}} \mathsf{d}_{\text{int}}(\boldsymbol{d}^p(t)) \; d\mathbf{x} \; dt = c \quad \forall \; t^* \geq \bar{t}, \tag{A.4}$$

that means

$$\boldsymbol{d}^p = \mathbf{0} \quad \forall \; t^* \geq \bar{t}. \tag{A.5}$$

Thus,

$$\boldsymbol{\varepsilon}_p = \mathbb{C} \quad \forall \; t^* \geq \bar{t}, \tag{A.6}$$

however, using equation (A.3)

$$\boldsymbol{\sigma}^r = \boldsymbol{\mathcal{Z}}\mathbb{C} \quad \forall \; t^* \geq \bar{t} \tag{A.7}$$

That is, the shakedown condition results in the time independent residual stress $\boldsymbol{\sigma}^r$.

A.2 Armstrong Frederick model

The stress field is decomposed by,

$$\boldsymbol{\sigma}(t) = \boldsymbol{\sigma}^E(t) + \boldsymbol{\sigma}^r(t). \tag{A.8}$$

Taking only the deviatoric components,

$$\boldsymbol{S}(t) = \boldsymbol{S}^E(t) + \boldsymbol{S}^r(t). \tag{A.9}$$

The residual operator applies

$$\boldsymbol{\sigma}^r(t) = \boldsymbol{\mathcal{Z}}\boldsymbol{\varepsilon}^p(t) \qquad \dot{\boldsymbol{\sigma}}^r(t) = \boldsymbol{\mathcal{Z}}\boldsymbol{d}^p(t). \tag{A.10}$$

The flow law is non-associated, but the plastic strain rate follows

$$\boldsymbol{d}^p(t) = \sqrt{\tfrac{3}{2}}\dot{\lambda}(t)\boldsymbol{n}(t). \tag{A.11}$$

The backstress evolution is

$$\dot{\boldsymbol{A}} = \dot{\lambda}\left[\sqrt{\tfrac{2}{3}}H_{ki}\boldsymbol{n}(t) - H_{nl}\boldsymbol{A}\right]. \tag{A.12}$$

The yield surface is

$$f\left[\boldsymbol{S}(t), \boldsymbol{A}(t)\right] = \sqrt{\tfrac{3}{2}}\|\boldsymbol{S}(t) - \boldsymbol{A}(t)\| - \sigma_Y^0 \leq 0, \tag{A.13}$$

and the complementary conditions are

$$\dot{\lambda}(t) \geq 0 \qquad f\left[\boldsymbol{S}(t), \boldsymbol{A}(t)\right]\dot{\lambda}(t) = 0. \tag{A.14}$$

The shakedown condition reads

$$\boldsymbol{\varepsilon}^p(t > \bar{t}) = \boldsymbol{\varepsilon}^p(\bar{t}) = \bar{\boldsymbol{\varepsilon}^p} \tag{A.15}$$

Once $\boldsymbol{d}^p(t) = \dot{\boldsymbol{\varepsilon}^p}(t)$, thus, for all $t > \bar{t}$, $\boldsymbol{d}^p(t) = \boldsymbol{0}$. So, substituting in (A.10b)

$$\dot{\boldsymbol{\sigma}}^r(t) = \boldsymbol{0} \quad \forall \quad t > \bar{t} \tag{A.16}$$

Thus,

$$\boldsymbol{\sigma}^r(t) = \boldsymbol{\sigma}^r(\bar{t}) = \bar{\boldsymbol{\sigma}^r} \quad \forall \quad t > \bar{t} \tag{A.17}$$

Using $\boldsymbol{d}^p(t) = \mathbf{0}$ in (A.11),

$$\mathbf{0} = \sqrt{\tfrac{3}{2}}\dot{\lambda}\boldsymbol{n}(t) \quad \forall \quad t > \bar{t} \tag{A.18}$$

Assuming $\boldsymbol{n}(t) \neq \mathbf{0}$, so $\dot{\lambda}(t) = 0$, for all $t > \bar{t}$. Using it in backstress evolution equation (A.12),

$$\boldsymbol{A}(t) = \boldsymbol{A}(\bar{t}) = \bar{\boldsymbol{A}} \quad \forall \quad t > \bar{t} \tag{A.19}$$

Using (A.9) in (A.13),

$$f\left[\boldsymbol{S}(t), \boldsymbol{A}(t)\right] = \sqrt{\tfrac{3}{2}}\|\boldsymbol{S}^E(t) + \boldsymbol{S}^r(t) - \boldsymbol{A}(t)\| - \sigma_Y^0 \leq 0. \tag{A.20}$$

Considering the post transient phase,

$$f\left[\boldsymbol{S}(t), \boldsymbol{A}(t)\right] = \sqrt{\tfrac{3}{2}}\|\boldsymbol{S}^E(t) + (\bar{\boldsymbol{S}}^r - \bar{\boldsymbol{A}})\| - \sigma_Y^0 \leq 0 \quad \forall \quad t > \bar{t} \tag{A.21}$$

Defining $\bar{\boldsymbol{S}} = \bar{\boldsymbol{S}}^r - \bar{\boldsymbol{A}}$,

$$f\left[\boldsymbol{S}(t), \boldsymbol{A}(t)\right] = \sqrt{\tfrac{3}{2}}\|\boldsymbol{S}^E(t) + \bar{\boldsymbol{S}}\| - \sigma_Y^0 \leq 0 \quad \forall \quad t > \bar{t} \tag{A.22}$$

In summary, if shakedown occurs with the AF model, there exists a time independent $\bar{\boldsymbol{S}}$ that when superposed with $\boldsymbol{S}^E(t)$ renders an admissible stress for all time after the transient phase ($t > \bar{t}$).

Appendix B

Triangular kinematical element

The examples developed in the thesis adopted elements with stress-displacement mixed formulation. Systematic research already showed that such kind of formulation is well suited to deal with elastoplastic problems (Krabbenhøft et al., 2007a,b; Zouain et al., 2014).

In turn, the author recognizes that the kinematical formulation is the standard choice of commercial codes, such as Ansys, when dealing with incremental analysis. Moreover, the incremental path does not require a structural (global) deformation operator $\boldsymbol{B}$, but only a structural stiffness matrix $\boldsymbol{K}$, mounted by elemental stiffness matrices contributions.

This fact could minimize the potential implementation of the methods described in this project, due to a cultural barrier, which, clearly, is not scientific at all. To overcome this potential risk, the author developed a conventional element using kinematical formulation, triangular shape with straight edges and second order interpolation functions, shown in figure B.1.

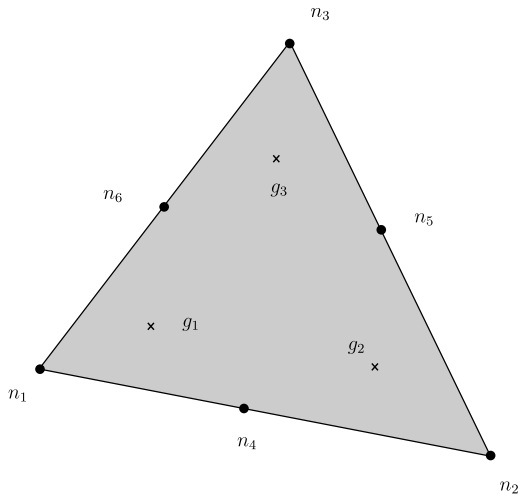

Figure B.1: Second order kinematical triangle. Nodes $(n_1, n_2, ..., n_6)$ and interior Gauss points (g_1, g_2, g_3)

The implementation applies for plane strain. Enhanced versions of such basic element are present in most of the commercial codes. The development includes the determination of the structural deformation operator $\boldsymbol{B}$ and residual matrix $\boldsymbol{Z}$.

Embracing alternatives for implementation of second order triangles can be found in Felippa (2004).

B.1 Natural coordinates

The second order kinematic triangle is formulated considering natural coordinates $(\zeta_1, \zeta_2, \zeta_3)$. See figure B.2.

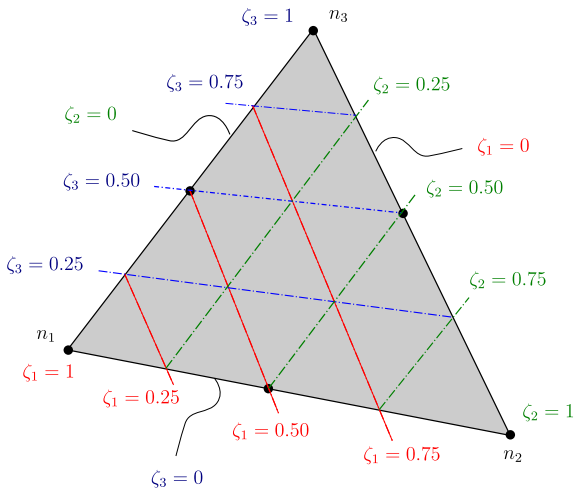

Figure B.2: Triangle natural coordinates $(\zeta_1, \zeta_2, \zeta_3)$.

Equation (B.1) lists the coordinates of the triangle vertexes.

$$[n_1, n_2, n_3]^T = [(x_1, y_1), (x_2, y_2), (x_3, y_3)]^T \tag{B.1}$$

The natural coordinates $(\zeta_1, \zeta_2, \zeta_3)$ relate to the Cartesian coordinates (x, y) by the linear mapping present in equation (B.2).

$$\begin{bmatrix} 1 \\ x \\ y \end{bmatrix} = \begin{bmatrix} 1 & 1 & 1 \\ x_1 & x_2 & x_3 \\ y_1 & y_2 & y_3 \end{bmatrix} \begin{bmatrix} \zeta_1 \\ \zeta_2 \\ \zeta_3 \end{bmatrix} \tag{B.2}$$

B.2 Interpolation operators

The kinematical finite element is a triangle with quadratic displacements, continuous through elements. The nodes (n_4, n_5, n_6) positions are in the middle of the straight edge triangle, as show in figure B.1.

The vector collecting the twelve displacements components $\boldsymbol{u}^i$, when considering the six element nodes $(n_1, n_2, ..., n_6)$ is

$$\boldsymbol{u}^i = \begin{bmatrix} u_x^1 & u_y^1 & u_x^2 & u_y^2 & \dots & u_x^6 & u_y^6 \end{bmatrix}^T \tag{B.3}$$

The interpolation functions N_i $(i = 1, 2, ..., 6)$, shown in equations (B.4)-(B.9), build the interpolation operator $\boldsymbol{N}$ though equation (B.10).

$$N_1(\zeta_1, \zeta_2, \zeta_3) = 4\zeta_1 \left(\zeta_2 - \frac{1}{2}\right)\left(\zeta_3 - \frac{1}{2}\right) \tag{B.4}$$

$$N_2(\zeta_1, \zeta_2, \zeta_3) = 4\zeta_2 \left(\zeta_1 - \frac{1}{2}\right)\left(\zeta_3 - \frac{1}{2}\right) \tag{B.5}$$

$$N_3(\zeta_1, \zeta_2, \zeta_3) = 4\zeta_3 \left(\zeta_1 - \frac{1}{2}\right)\left(\zeta_2 - \frac{1}{2}\right) \tag{B.6}$$

$$N_4(\zeta_1, \zeta_2, \zeta_3) = 4\zeta_1\zeta_2 \tag{B.7}$$

$$N_5(\zeta_1, \zeta_2, \zeta_3) = 4\zeta_2\zeta_3 \tag{B.8}$$

$$N_6(\zeta_1, \zeta_2, \zeta_3) = 4\zeta_1\zeta_3 \tag{B.9}$$

$$\boldsymbol{N} = \begin{bmatrix} N_1\boldsymbol{1}_2 & N_2\boldsymbol{1}_2 & \dots & N_6\boldsymbol{1}_2 \end{bmatrix} \qquad \boldsymbol{1}_2 = \begin{bmatrix} 1 & 0 \\ 0 & 1 \end{bmatrix} \tag{B.10}$$

The interpolation operator $\boldsymbol{N}$ applied to elemental displacement vector $\boldsymbol{u}^i$ gives the interpolated displacements field inside the element.

B.3 Stress and strain vectors

The strain list, calculated at a Gauss point g, is

$$\boldsymbol{\varepsilon}_g := \begin{bmatrix} \varepsilon_x^g & \varepsilon_y^g & 0 & \sqrt{2}\varepsilon_{xy}^g \end{bmatrix}. \tag{B.11}$$

The element strain vector collecting the twelve strain components, comprising three Gauss points, is

$$\boldsymbol{\varepsilon}^e := \begin{bmatrix} \boldsymbol{\varepsilon}_1 & \boldsymbol{\varepsilon}_2 & \boldsymbol{\varepsilon}_3 \end{bmatrix}^T. \tag{B.12}$$

The stress list, calculated at a Gauss point g, is

$$\boldsymbol{\sigma}_g := \begin{bmatrix} \sigma_x^g & \sigma_y^g & \sigma_z^g & \sqrt{2}\sigma_{xy}^g. \end{bmatrix} \tag{B.13}$$

The elemental stress vector collecting the twelve stress components, considering all three Gauss points, is

$$\boldsymbol{\sigma}^e := \begin{bmatrix} \boldsymbol{\sigma}_1 & \boldsymbol{\sigma}_2 & \boldsymbol{\sigma}_3 \end{bmatrix}^T \tag{B.14}$$

The $\sqrt{2}$ factor placed in the fourth position of stress list $\boldsymbol{\sigma}_g$ and strain list $\boldsymbol{\varepsilon}_g$ simplifies internal work computation, using dot product between $\boldsymbol{\sigma}^e$ and $\boldsymbol{\varepsilon}^e$.

B.4 Elemental deformation operator

Applying the symmetric gradient operator $\mathcal{D}$ on interpolation mapping $\boldsymbol{N}$, the nodal displacements to point strains mapping $\mathcal{B}_p$ is generated. This operator applies to calculate strain list in a point $p = (x, y)$ inside the element.

$$\mathcal{B}_p = \mathcal{D}\boldsymbol{N} = \begin{bmatrix} \mathsf{B}^1 & \mathsf{B}^2 & \dots & \mathsf{B}^6 \end{bmatrix} \qquad \mathsf{B}^k = \begin{bmatrix} N_{k,x}(p) & 0 \\ 0 & N_{k,y}(p) \\ 0 & 0 \\ \frac{1}{\sqrt{2}} N_{k,y}(p) & \frac{1}{\sqrt{2}} N_{k,x}(p) \end{bmatrix} \tag{B.15}$$

Where $N_{k,x} := \partial N_k / \partial x$ and $N_{k,y} := \partial N_y / \partial y$.

The three interior Gauss points (g_1, g_2, g_3) are of particular interest. By evaluation and stacking, the elemental deformation operator $\bar{\boldsymbol{B}}^e$ is generated.

$$\bar{\boldsymbol{B}}^e = \begin{bmatrix} \mathcal{B}_{g_1} \\ \mathcal{B}_{g_2} \\ \mathcal{B}_{g_3} \end{bmatrix} \tag{B.16}$$

Such operator maps the nodal displacements $\boldsymbol{u}^e$ to Gauss points strain vector $\bar{\boldsymbol{\varepsilon}}^e$ inside an element e.

$$\bar{\boldsymbol{\varepsilon}}^e = \bar{\boldsymbol{B}}^e \boldsymbol{u}^e \tag{B.17}$$

For future convenience in the stiffness matrix $\boldsymbol{K}^e$ calculation, one third of the element area J^e is included in the definition of the operator $\boldsymbol{B}^e$. The motivation for such inclusion comes from the numerical integration in the parent domain Ω (J^e) and the weights of the numerical integration (one third).

$$\boldsymbol{B}^e = \frac{J^e}{3} \bar{\boldsymbol{B}}^e \tag{B.18}$$

The strain vector $\boldsymbol{\varepsilon}^e$ is calculated with the equation

$$\boldsymbol{\varepsilon}^e = \boldsymbol{B}^e \boldsymbol{u}^e. \tag{B.19}$$

Intentionally, the vector $\boldsymbol{\varepsilon}^e$ incorporates one third of the element area due to $\boldsymbol{B}^e$ definition.

B.5 Local elasticity operator

The Gauss point elastic operator $\mathbb{E}_g$ maps Gauss point strain vector $\bar{\boldsymbol{\varepsilon}}_e$ to Gauss point stress vector $\boldsymbol{\sigma}_g$.

$$\mathbb{E}_g = \frac{E}{(1+\nu)(1-2\nu)} \begin{bmatrix} 1-\nu & \nu & \nu & 0 \\ \nu & 1-\nu & \nu & 0 \\ \nu & \nu & 1-\nu & 0 \\ 0 & 0 & 0 & 1-2\nu \end{bmatrix} \tag{B.20}$$

$$\boldsymbol{\sigma}_g = \mathbb{E}_g \bar{\boldsymbol{\varepsilon}}_g \tag{B.21}$$

The elemental (local) elastic operator $\bar{\mathbb{E}}^e$ maps the element strain vector $\bar{\boldsymbol{\varepsilon}}^e$ to element stress vector $\boldsymbol{\sigma}^e$.

$$\bar{\mathbb{E}}^e = \begin{bmatrix} \mathbb{E}_g & \mathbf{0} & \mathbf{0} \\ \mathbf{0} & \mathbb{E}_g & \mathbf{0} \\ \mathbf{0} & \mathbf{0} & \mathbb{E}_g \end{bmatrix} \tag{B.22}$$

$$\boldsymbol{\sigma}^e = \bar{\mathbb{E}}^e \bar{\boldsymbol{\varepsilon}}^e \tag{B.23}$$

Again, to simplify future calculation of $\boldsymbol{K}^e$, a slight modification is proposed to compute $\mathbb{E}^e$.

$$\mathbb{E}^e = \frac{3}{J^e} \bar{\mathbb{E}}^e \tag{B.24}$$

Thus, alternatively to (B.23),

$$\boldsymbol{\sigma}^e = \mathbb{E}^e \boldsymbol{\varepsilon}^e. \tag{B.25}$$

B.6 Global deformation operator

The procedure to mount the global deformation matrix $\boldsymbol{B}$ is similar to the conventional one applied to mount stiffness matrix $\boldsymbol{K}$. The assembly of the operator $\boldsymbol{B}$ is required to apply the operations that define the residual operator $\boldsymbol{Z}$.

To build $\boldsymbol{B}$, two connectivity matrices are necessary, $\boldsymbol{C}^u$ and $\boldsymbol{C}^s$. The matrix $\boldsymbol{C}^u$ connects the labels of the degrees of freedom (displacements) for the global mesh with the labels of the local degrees of freedom. Each line of $\boldsymbol{C}^u$ corresponds to an element e. The line has twelve positions, filled by the labels of the element degrees of freedom corresponding to the twelve local labels $1, 2, .., 12$ (six nodes, with two displacements in each). The use of the matrix $\boldsymbol{C}^u$ is a standard practice for the assembly of the matrix $\boldsymbol{K}$.

Additionally, the matrix $\boldsymbol{C}^s$ stacks the global labels of the elemental strain components. Each row corresponds to an element e. The row has twelve positions, corresponding to the three Gauss points times the four strain components per point. The construction of $\boldsymbol{C}^s$ is straightforward, stacking sequential integers. That is, the first line has the sequence $1, 2, ...12$, the second $13, 14, ..., 24$ and so on.

Thus, the assembly of the global deformation operator follows the procedure described by algorithm 6

Procedure: $\boldsymbol{B}$ Assembly

for $e = 1$: number of elements of the mesh

  for $i = 1$: number of total strain components of the mesh

    for $j = 1$: number of degrees of freedom of the mesh

      $l := \boldsymbol{C}^s_{e,i} \qquad m := \boldsymbol{C}^u_{e,j}$

      $\boldsymbol{B}_{l,m} := \boldsymbol{B}_{l,m} + \boldsymbol{B}^e_{i,j}$

    end for

  end for

end for

end procedure $\boldsymbol{B}$ Assembly

Algorithm 6: Global Deformation Operator Assembly

The global deformation operator $\boldsymbol{B}$ maps the global mesh displacement vector $\boldsymbol{u}$ into the global mesh strain components vector $\boldsymbol{\varepsilon}$.

$$\boldsymbol{\varepsilon} = \boldsymbol{B}\boldsymbol{u} \tag{B.26}$$

B.7 Global elasticity operator

The global elasticity matrix $\mathbb{E}$ stacks n elemental elasticity operators $\mathbb{E}^e$ (with $e = 1, 2, ..., n$) through equation B.27.

$$\mathbb{E} = \begin{bmatrix} \mathbb{E}^1 & \mathbf{0} & \mathbf{0} & \dots & \mathbf{0} \\ \mathbf{0} & \mathbb{E}^2 & \mathbf{0} & \dots & \mathbf{0} \\ \mathbf{0} & \mathbf{0} & \mathbb{E}^3 & \dots & \mathbf{0} \\ \vdots & \vdots & \vdots & \ddots & \vdots \\ \mathbf{0} & \mathbf{0} & \mathbf{0} & \dots & \mathbb{E}^n \end{bmatrix} \tag{B.27}$$

It maps the global mesh strain components $\boldsymbol{\varepsilon}$ into global mesh stress components $\boldsymbol{\sigma}$, by the equation

$$\boldsymbol{\sigma} = \mathbb{E}\boldsymbol{\varepsilon}. \tag{B.28}$$

B.8 Elemental stiffness matrix

The computation of the elemental stiffness matrix is

$$\boldsymbol{K}^e = \int_A \bar{\boldsymbol{B}}^{eT} \bar{\mathbb{E}}^e \bar{\boldsymbol{B}}^e dA \tag{B.29}$$

Modifying coordinates to natural coordinates,

$$\boldsymbol{K}^e = \int_\Omega \bar{\boldsymbol{B}}^{eT} \bar{\mathbb{E}}^e \bar{\boldsymbol{B}}^e J^e d\Omega, \tag{B.30}$$

where $d\Omega$ is the infinitesimal area element in natural coordinates and Ω represents its integration limits.

Taking in consideration that at the Gauss points, the value of the evaluated interpolation functions multiplied by the element area and weighted by $1/3$ approximates the integral result,

$$\boldsymbol{K}^e = \frac{J^e}{3} \bar{\boldsymbol{B}}^{eT} \bar{\mathbb{E}}^e \bar{\boldsymbol{B}}^e. \tag{B.31}$$

Considering previous definitions,

$$\boldsymbol{K}^e = \boldsymbol{B}^{eT} \mathbb{E}^e \boldsymbol{B}^e \tag{B.32}$$

B.9 Global stiffness matrix

Using the elemental stiffness matrices $\boldsymbol{K}^e$, algorithm 7 applies as the conventional route to assembly the global stiffness matrix $\boldsymbol{K}$.

Procedure: $\boldsymbol{K}$ **Assembly**

for $e = 1$: number of elements of the mesh

  for $i = 1$: Number of degrees of freedom of the mesh

    for $j = 1$: Number of degrees of freedom of the mesh

      $l := \boldsymbol{C}^u_{e,i} \qquad m := \boldsymbol{C}^u_{e,j}$

      $\boldsymbol{K}_{l,m} := \boldsymbol{K}_{l,m} + \boldsymbol{K}^e_{i,j}$

    end for

  end for

end for

end procedure $\boldsymbol{K}$ **Assembly**

Algorithm 7: Global Stiffness Operator Assembly

Alternatively, if the global deformation operator $\boldsymbol{B}$ is computed with algorithm 6 and global elasticity operator $\mathbb{E}$ with the equation (B.27), the global stiffness matrix $\boldsymbol{K}$ can be directly computed by

$$\boldsymbol{K} = \boldsymbol{B}^T \mathbb{E} \boldsymbol{B} \tag{B.33}$$

B.10 Residual matrix

Once $\boldsymbol{B}$ and $\boldsymbol{K}$ are assembled, the operations to mount the residual matrix are

$$\boldsymbol{Z} = \mathbb{E}\boldsymbol{B}\boldsymbol{K}^{-1}\boldsymbol{B}^T\mathbb{E} - \mathbb{E}. \tag{B.34}$$

Remarkably, $\boldsymbol{Z}$ tends to become a big matrix, so the algorithm applies the sequential operations that form $\boldsymbol{Z}$ in order to perform.

B.11 Example of application - PCHE

Figure B.3 shows the norm of the ratchet strain $\|\Delta\boldsymbol{\varepsilon}\|$ using different element formulations. The model is the same reported in section 5.4.7.

Concerning direct results, the Figure shows two mixed stress-displacement and the kinematical formulation. The mixed formulations are $\boldsymbol{S}3$–σ_m–$\boldsymbol{v}6$ and $\boldsymbol{\sigma}3$–$\boldsymbol{v}6$. Whereas $\boldsymbol{v}6$ is the kinematical formulation introduced in this annex. In sequence the incremental result generated with Ansys and PLANE183 kinematical formulation appears in the same figure.

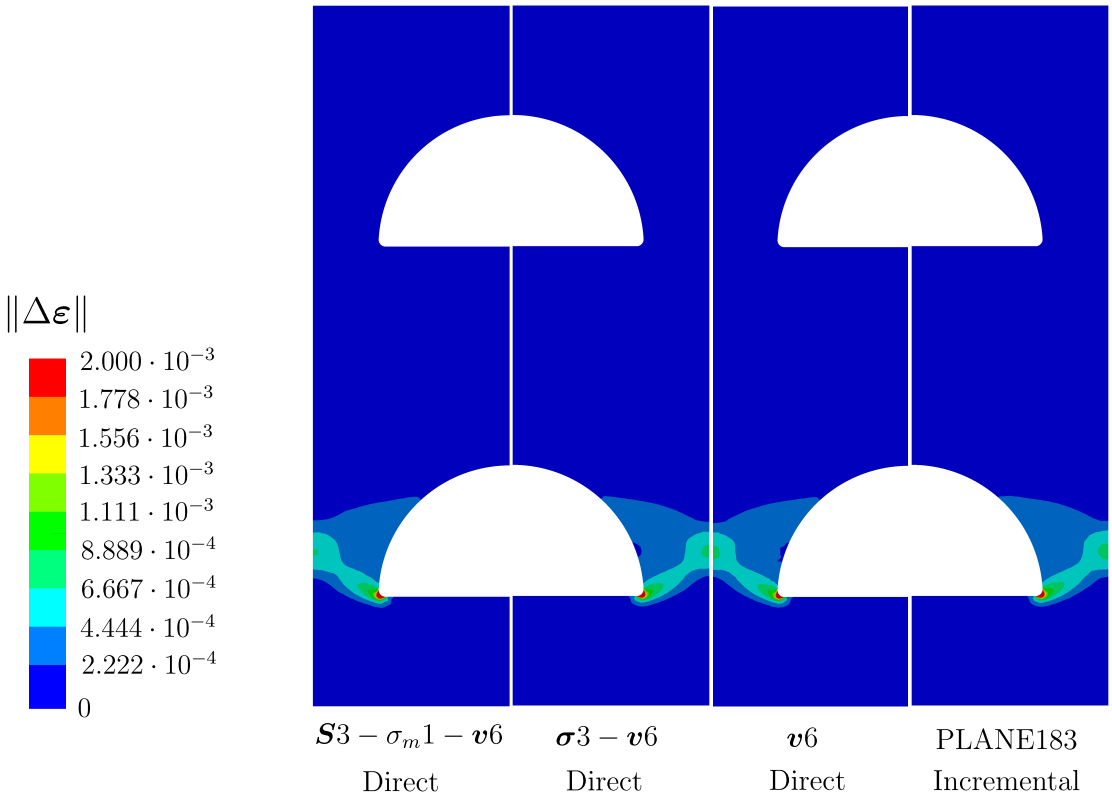

Figure B.3: Norm of the ratchet strain $\|\Delta\boldsymbol{\varepsilon}\|$ with different elements.

Appendix C

Integrating with a generalized midpoint approximation

Artioli et al. (2007) and de Souza Neto et al. (2008, p. 202)

Given $\boldsymbol{\sigma}^E(t) = \boldsymbol{S}^E(t) + \sigma_m^E(t)\boldsymbol{1}$, find $\boldsymbol{\sigma}^r(t)$, $\boldsymbol{A}(t)$, and $\boldsymbol{d}^p(t)$ such that

$$\boldsymbol{\sigma}^r(t) = \boldsymbol{S}^r(t) + \sigma_m^r(t)\boldsymbol{1} \tag{C.1}$$

$$\boldsymbol{d}^p = \sqrt{\tfrac{3}{2}}\dot{\lambda}\boldsymbol{n} \tag{C.2}$$

$$\dot{\boldsymbol{A}} = \dot{\lambda}\left(\sqrt{\tfrac{2}{3}}H_{ki}\boldsymbol{n} - H_{nl}\boldsymbol{A}\right) \tag{C.3}$$

$$\boldsymbol{n} = \frac{\boldsymbol{S}-\boldsymbol{A}}{\|\boldsymbol{S}-\boldsymbol{A}\|} \tag{C.4}$$

$$f = \sqrt{\tfrac{3}{2}}\|\boldsymbol{S}-\boldsymbol{A}\| - \sigma_Y^0 \leqslant 0 \qquad \dot{\lambda} \geqslant 0 \qquad f\dot{\lambda} = 0 \tag{C.5}$$

Generalized midpoint approximation

Consider the generalized midpoint approximation of the constitutive evolutive equations (C.1-C.5), where $\vartheta \in [0,1]$ and $\vartheta = 1$ gives purely implicit Euler approximation (Artioli et al., 2007, p. 1829).

$$\boldsymbol{S}^j - \boldsymbol{S}^{j-1} = 2G(\delta\boldsymbol{\varepsilon}^{\mathrm{dev},j} - \delta\boldsymbol{\varepsilon}^{p,j}) \tag{C.6}$$

$$\delta\boldsymbol{\varepsilon}^{p,j} = \sqrt{\tfrac{3}{2}}\delta\lambda\boldsymbol{n}^{\vartheta} \tag{C.7}$$

$$\boldsymbol{A}^j - \boldsymbol{A}^{j-1} = \delta\lambda\left(H_{ki}\boldsymbol{n}^{\vartheta} - H_{nl}\boldsymbol{A}^{\vartheta}\right) \tag{C.8}$$

$$\boldsymbol{\kappa}^j = \boldsymbol{S}^j - \boldsymbol{A}^j \tag{C.9}$$

$$f^j = \sqrt{\tfrac{3}{2}}\|\boldsymbol{\kappa}^j\| - \sigma_Y^0 \leqslant 0 \qquad \delta\lambda \geqslant 0 \qquad f^j\delta\lambda = 0 \tag{C.10}$$

where

$$\boldsymbol{n}^{\vartheta} = \frac{\boldsymbol{\kappa}^{\vartheta}}{\|\boldsymbol{\kappa}^{\vartheta}\|} \tag{C.11}$$

$$\boldsymbol{\kappa}^{\vartheta} = \boldsymbol{S}^{\vartheta} - \boldsymbol{A}^{\vartheta} \tag{C.12}$$

$$\boldsymbol{S}^{\vartheta} := \vartheta \boldsymbol{S}^{j} + (1-\vartheta)\boldsymbol{S}^{j-1} \tag{C.13}$$

$$\boldsymbol{A}^{\vartheta} := \vartheta \boldsymbol{A}^{j} + (1-\vartheta)\boldsymbol{A}^{j-1} \tag{C.14}$$

Given the current approximations $\boldsymbol{S}^{r,j}$, $\delta\boldsymbol{\varepsilon}^{p,j}$ and $\boldsymbol{A}^{j-1}$, the definition of the driving parameters is

$$\boldsymbol{S}^{\text{trial}} := \boldsymbol{S}^{E,j} + \boldsymbol{S}^{r,j} + 2G\delta\boldsymbol{\varepsilon}^{p,j} \qquad \boldsymbol{A}^{\text{trial}} := \boldsymbol{A}^{j-1} \tag{C.15}$$

$$\boldsymbol{\kappa}^{\text{trial}} := \boldsymbol{S}^{\text{trial}} - \boldsymbol{A}^{\text{trial}} \tag{C.16}$$

The new approximations $\delta\boldsymbol{\varepsilon}^{p,j}$ and $\boldsymbol{A} := \boldsymbol{A}^{j}$ are found by solving the generalized midpoint equations, with additional unknowns $\boldsymbol{S}$, $\delta\lambda$ and $\boldsymbol{n}^{\vartheta}$.

If $\sqrt{\frac{3}{2}}\|\boldsymbol{\kappa}^{\text{trial}}\| \leqslant \sigma_Y^0$ the response is the trial state. Otherwise, proceed to solve

$$\boldsymbol{S}^{\text{trial}} = \boldsymbol{S} + 2G\delta\boldsymbol{\varepsilon}^{p,j} \tag{C.17}$$

$$\delta\boldsymbol{\varepsilon}^{p,j} = \sqrt{\tfrac{3}{2}}\delta\lambda\boldsymbol{n}^{\vartheta} \tag{C.18}$$

$$\boldsymbol{A} - \boldsymbol{A}^{\text{trial}} = \delta\lambda\left(\sqrt{\tfrac{2}{3}}H_{ki}\boldsymbol{n}^{\vartheta} - H_{nl}\boldsymbol{A}^{\vartheta}\right) \tag{C.19}$$

$$\boldsymbol{n}^{\vartheta} = \frac{\boldsymbol{\kappa}^{\vartheta}}{\|\boldsymbol{\kappa}^{\vartheta}\|} \tag{C.20}$$

$$\boldsymbol{\kappa}^{\vartheta} = \boldsymbol{S}^{\vartheta} - \boldsymbol{A}^{\vartheta} \tag{C.21}$$

$$\boldsymbol{A}^{\vartheta} := \vartheta \boldsymbol{A} + (1-\vartheta)\boldsymbol{A}^{\text{trial}} \tag{C.22}$$

$$\boldsymbol{S}^{\vartheta} := \vartheta \boldsymbol{S} + (1-\vartheta)\boldsymbol{S}^{j-1} \tag{C.23}$$

$$\boldsymbol{\kappa} = \boldsymbol{S} - \boldsymbol{A} \tag{C.24}$$

$$\sqrt{\tfrac{3}{2}}\|\boldsymbol{\kappa}\| = \sigma_Y^0 \tag{C.25}$$

Note that with

$$\boldsymbol{\kappa}^{j-1} := \boldsymbol{S}^{j-1} - \boldsymbol{A}^{\text{trial}} \tag{C.26}$$

Thus,

$$\boldsymbol{\kappa}^{\vartheta} = \vartheta\boldsymbol{\kappa} + (1-\vartheta)\boldsymbol{\kappa}^{j-1} \tag{C.27}$$

Eliminating the unknown $\delta\boldsymbol{\varepsilon}^{p,j}$ from the system of equations (C.17-C.25), one

obtains a system to be solved for the main unknowns $\delta\lambda$, $\boldsymbol{S}$ and $\boldsymbol{A}$.

$$\boldsymbol{S}^{\text{trial}} = \boldsymbol{S} + \sqrt{6}G\delta\lambda\boldsymbol{n}^{\vartheta} \tag{C.28}$$

$$\boldsymbol{A} - \boldsymbol{A}^{\text{trial}} = \delta\lambda\left(\sqrt{\tfrac{2}{3}}H_{ki}\boldsymbol{n}^{\vartheta} - H_{nl}\boldsymbol{A}^{\vartheta}\right) \tag{C.29}$$

$$\boldsymbol{n}^{\vartheta} = \frac{\boldsymbol{\kappa}^{\vartheta}}{\|\boldsymbol{\kappa}^{\vartheta}\|} \tag{C.30}$$

$$\boldsymbol{\kappa}^{\vartheta} = \boldsymbol{S}^{\vartheta} - \boldsymbol{A}^{\vartheta} \tag{C.31}$$

$$\boldsymbol{A}^{\vartheta} := \vartheta\boldsymbol{A} + (1-\vartheta)\boldsymbol{A}^{\text{trial}} \tag{C.32}$$

$$\boldsymbol{S}^{\vartheta} := \vartheta\boldsymbol{S} + (1-\vartheta)\boldsymbol{S}^{j-1} \tag{C.33}$$

$$\boldsymbol{\kappa} = \boldsymbol{S} - \boldsymbol{A} \tag{C.34}$$

$$\sqrt{\tfrac{3}{2}}\|\boldsymbol{\kappa}\| = \sigma_{\text{Y}}^{0} \tag{C.35}$$

It is proved in the following sections that this system can be solved by firstly computing $\delta\lambda$ as the least positive root of a tenth degree polynomial. Then, the other unknowns are computed by sequentially applying the following equalities.

1. Basic solution.

   Here, sequentially apply the following equalities.

$$\boldsymbol{S}^{\vartheta,\text{trial}} := \vartheta\boldsymbol{S}^{\text{trial}} + (1-\vartheta)\boldsymbol{S}^{j-1} \tag{C.36}$$

$$V_{\lambda} := (1 + \vartheta H_{nl}\delta\lambda)^{-1} \tag{C.37}$$

$$\boldsymbol{\kappa}^{\lambda} := \boldsymbol{S}^{\vartheta,\text{trial}} - V_{\lambda}\boldsymbol{A}^{\text{trial}} \tag{C.38}$$

$$\boldsymbol{n}^{\vartheta} := \frac{\boldsymbol{\kappa}^{\lambda}}{\|\boldsymbol{\kappa}^{\lambda}\|} \tag{C.39}$$

$$\boldsymbol{S}^{\vartheta} = \boldsymbol{S}^{\vartheta,\text{trial}} - \sqrt{6}\vartheta G\delta\lambda\boldsymbol{n}^{\vartheta} \tag{C.40}$$

$$\boldsymbol{S} = \tfrac{1}{\vartheta}\left[\boldsymbol{S}^{\vartheta} - (1-\vartheta)\boldsymbol{S}^{j-1}\right] \tag{C.41}$$

$$\boldsymbol{A}^{\vartheta} = V_{\lambda}\boldsymbol{A}^{\text{trial}} + \sqrt{\tfrac{2}{3}}\vartheta H_{ki}\delta\lambda V_{\lambda}\boldsymbol{n}^{\vartheta} \tag{C.42}$$

$$\boldsymbol{A} = \tfrac{1}{\vartheta}\left[\boldsymbol{A}^{\vartheta} - (1-\vartheta)\boldsymbol{A}^{\text{trial}}\right] \tag{C.43}$$

$$\boldsymbol{\kappa} = \boldsymbol{S} - \boldsymbol{A} \tag{C.44}$$

$$\boldsymbol{n} = \frac{\boldsymbol{\kappa}}{\|\boldsymbol{\kappa}\|} \tag{C.45}$$

2. Updating equations

$$\boldsymbol{A}^{j} = \boldsymbol{A} \tag{C.46}$$

$$\delta\boldsymbol{\beta}^{j} = \tfrac{3}{2H_{ki}}(\boldsymbol{A}^{j} - \boldsymbol{A}^{j-1}) \tag{C.47}$$

Finally, the alternative updates are

$$\delta\boldsymbol{\varepsilon}^{p,j} = \sqrt{\tfrac{3}{2}}\delta\lambda\boldsymbol{n}^{\vartheta} \tag{C.48}$$

or

$$\delta\boldsymbol{\varepsilon}^{p,j} = \sqrt{\tfrac{3}{2}}\delta\lambda\boldsymbol{n} \tag{C.49}$$

where the first one is the only consistent with the proposed approximate integration given by (C.17-C.25).

C.1 The equation in $\delta\lambda$ for midpoint integration

$$\boldsymbol{S}^{\text{trial}} = \boldsymbol{S} + \sqrt{6}\mathsf{G}\delta\lambda\boldsymbol{n}^{\vartheta} \tag{C.50}$$

$$\boldsymbol{S}^{\vartheta} := \vartheta\boldsymbol{S} + (1-\vartheta)\boldsymbol{S}^{j-1} \tag{C.51}$$

$$\vartheta\boldsymbol{S}^{\text{trial}} = \vartheta\boldsymbol{S} + \sqrt{6}\vartheta\mathsf{G}\delta\lambda\boldsymbol{n}^{\vartheta} \tag{C.52}$$

$$\vartheta\boldsymbol{S}^{\text{trial}} = \boldsymbol{S}^{\vartheta} - (1-\vartheta)\boldsymbol{S}^{j-1} + \sqrt{6}\vartheta\mathsf{G}\delta\lambda\boldsymbol{n}^{\vartheta} \tag{C.53}$$

$$\boldsymbol{S}^{\vartheta,\text{trial}} := \vartheta\boldsymbol{S}^{\text{trial}} + (1-\vartheta)\boldsymbol{S}^{j-1} \tag{C.54}$$

$$\boldsymbol{S}^{\vartheta} = \boldsymbol{S}^{\vartheta,\text{trial}} - \sqrt{6}\vartheta\mathsf{G}\delta\lambda\boldsymbol{n}^{\vartheta} \tag{C.55}$$

$$\vartheta\boldsymbol{A} - \vartheta\boldsymbol{A}^{\text{trial}} = \vartheta\delta\lambda\left(\sqrt{\tfrac{2}{3}}H_{ki}\boldsymbol{n}^{\vartheta} - H_{nl}\boldsymbol{A}^{\vartheta}\right) \tag{C.56}$$

$$\boldsymbol{A}^{\vartheta} = \vartheta\boldsymbol{A} + (1-\vartheta)\boldsymbol{A}^{\text{trial}} \tag{C.57}$$

$$\boldsymbol{A}^{\vartheta} - (1-\vartheta)\boldsymbol{A}^{\text{trial}} - \vartheta\boldsymbol{A}^{\text{trial}} = \vartheta\delta\lambda\left(\sqrt{\tfrac{2}{3}}H_{ki}\boldsymbol{n}^{\vartheta} - H_{nl}\boldsymbol{A}^{\vartheta}\right) \tag{C.58}$$

$$\boldsymbol{A}^{\vartheta} - \boldsymbol{A}^{\text{trial}} = \vartheta\delta\lambda\left(\sqrt{\tfrac{2}{3}}H_{ki}\boldsymbol{n}^{\vartheta} - H_{nl}\boldsymbol{A}^{\vartheta}\right) \tag{C.59}$$

$$(1 + \vartheta H_{nl}\delta\lambda)\boldsymbol{A}^{\vartheta} = \boldsymbol{A}^{\text{trial}} + \sqrt{\tfrac{2}{3}}\vartheta H_{ki}\delta\lambda\boldsymbol{n}^{\vartheta} \tag{C.60}$$

$$V_{\lambda} := (1 + \vartheta H_{nl}\delta\lambda)^{-1} \tag{C.61}$$

$$\boldsymbol{A}^{\vartheta} = V_{\lambda}\boldsymbol{A}^{\text{trial}} + \sqrt{\tfrac{2}{3}}\vartheta H_{ki}\delta\lambda V_{\lambda}\boldsymbol{n}^{\vartheta} \tag{C.62}$$

$$\boldsymbol{\kappa}^{\vartheta} = \boldsymbol{S}^{\vartheta,\text{trial}} - \sqrt{6}\vartheta\mathsf{G}\delta\lambda\boldsymbol{n}^{\vartheta} - V_{\lambda}\boldsymbol{A}^{\text{trial}} - \sqrt{\tfrac{2}{3}}\vartheta H_{ki}\delta\lambda V_{\lambda}\boldsymbol{n}^{\vartheta} \tag{C.63}$$

$$\boldsymbol{\kappa}^{\vartheta} = \boldsymbol{S}^{\vartheta,\text{trial}} - V_{\lambda}\boldsymbol{A}^{\text{trial}} - \sqrt{6}\vartheta\mathsf{G}\delta\lambda\boldsymbol{n}^{\vartheta} - \sqrt{\tfrac{2}{3}}\vartheta H_{ki}\delta\lambda V_{\lambda}\boldsymbol{n}^{\vartheta} \tag{C.64}$$

$$\boldsymbol{\kappa}^{\vartheta} = \boldsymbol{S}^{\vartheta,\text{trial}} - V_\lambda \boldsymbol{A}^{\text{trial}} - (\sqrt{6}\vartheta G \delta\lambda + \sqrt{\tfrac{2}{3}}\vartheta H_{ki}\delta\lambda V_\lambda)\boldsymbol{n}^{\vartheta} \tag{C.65}$$

Defining

$$\boldsymbol{\kappa}^{\lambda} := \boldsymbol{S}^{\vartheta,\text{trial}} - V_\lambda \boldsymbol{A}^{\text{trial}} \tag{C.66}$$

$$Y_\lambda := \vartheta\delta\lambda\left(\sqrt{6}G + \sqrt{\tfrac{2}{3}}H_{ki}V_\lambda\right) \tag{C.67}$$

So that (C.65) becomes

$$\boldsymbol{\kappa}^{\lambda} = \boldsymbol{\kappa}^{\vartheta} + Y_\lambda \boldsymbol{n}^{\vartheta} \tag{C.68}$$

Now, a crucial step: Since $\boldsymbol{\kappa}^{\vartheta} = \|\boldsymbol{\kappa}^{\vartheta}\|\boldsymbol{n}^{\vartheta}$ and $Y_\lambda > 0$ (for $\delta\lambda > 0$, thus, $V_\lambda > 0$), it is deduced from (C.68) that

$$\boldsymbol{n}^{\vartheta} = \frac{\boldsymbol{\kappa}^{\lambda}}{\|\boldsymbol{\kappa}^{\lambda}\|} \tag{C.69}$$

and

$$\|\boldsymbol{\kappa}^{\lambda}\| = \|\boldsymbol{\kappa}^{\vartheta}\| + Y_\lambda \tag{C.70}$$

Then

$$\boldsymbol{\kappa}^{\vartheta} = \boldsymbol{\kappa}^{\lambda} - Y_\lambda \boldsymbol{n}^{\vartheta} = \boldsymbol{\kappa}^{\lambda} - \frac{Y_\lambda}{\|\boldsymbol{\kappa}^{\lambda}\|}\boldsymbol{\kappa}^{\lambda} \tag{C.71}$$

or

$$\boldsymbol{\kappa}^{\vartheta} = \left(1 - \frac{Y_\lambda}{\|\boldsymbol{\kappa}^{\lambda}\|}\right)\boldsymbol{\kappa}^{\lambda} \tag{C.72}$$

Recalling that, if $\vartheta > 0$,

$$\boldsymbol{\kappa} = \tfrac{1}{\vartheta}\boldsymbol{\kappa}^{\vartheta} - \tfrac{1-\vartheta}{\vartheta}\boldsymbol{\kappa}^{j-1} \tag{C.73}$$

Substituting $\boldsymbol{\kappa}^{\vartheta}$, from (C.72), in the above equation,

$$\vartheta\boldsymbol{\kappa} = \left(1 - \frac{Y_\lambda}{\|\boldsymbol{\kappa}^{\lambda}\|}\right)\boldsymbol{\kappa}^{\lambda} - (1-\vartheta)\boldsymbol{\kappa}^{j-1} \tag{C.74}$$

$$\vartheta^2\|\boldsymbol{\kappa}\|^2 = \left(1 - \frac{Y_\lambda}{\|\boldsymbol{\kappa}^{\lambda}\|}\right)^2 \|\boldsymbol{\kappa}^{\lambda}\|^2 + (1-\vartheta)^2\|\boldsymbol{\kappa}^{j-1}\|^2 - 2(1-\vartheta)\left(1 - \frac{Y_\lambda}{\|\boldsymbol{\kappa}^{\lambda}\|}\right)\boldsymbol{\kappa}^{j-1}\cdot\boldsymbol{\kappa}^{\lambda} \tag{C.75}$$

$$\left(1 - \frac{Y_\lambda}{\|\boldsymbol{\kappa}^{\lambda}\|}\right)^2 \|\boldsymbol{\kappa}^{\lambda}\|^2 + (1-\vartheta)^2\|\boldsymbol{\kappa}^{j-1}\|^2 - 2(1-\vartheta)\left(1 - \frac{Y_\lambda}{\|\boldsymbol{\kappa}^{\lambda}\|}\right)\boldsymbol{\kappa}^{j-1}\cdot\boldsymbol{\kappa}^{\lambda} - \tfrac{2}{3}\vartheta^2{\sigma_Y^0}^2 = 0 \tag{C.76}$$

Defining w

$$w := \tfrac{2}{3}\vartheta^2 {\sigma_Y^0}^2 - (1-\vartheta)^2 \|\boldsymbol{\kappa}^{j-1}\|^2 \tag{C.77}$$

$$\left(1 - \frac{Y_\lambda}{\|\boldsymbol{\kappa}^\lambda\|}\right)^2 \|\boldsymbol{\kappa}^\lambda\|^2 - 2(1-\vartheta)\left(1 - \frac{Y_\lambda}{\|\boldsymbol{\kappa}^\lambda\|}\right)\boldsymbol{\kappa}^{j-1}\cdot\boldsymbol{\kappa}^\lambda - w = 0 \tag{C.78}$$

$$\|\boldsymbol{\kappa}^\lambda\|^2 + Y_\lambda^2 - 2Y_\lambda\|\boldsymbol{\kappa}^\lambda\| - 2(1-\vartheta)\boldsymbol{\kappa}^{j-1}\cdot\boldsymbol{\kappa}^\lambda + \frac{2(1-\vartheta)Y_\lambda}{\|\boldsymbol{\kappa}^\lambda\|}\boldsymbol{\kappa}^{j-1}\cdot\boldsymbol{\kappa}^\lambda - w = 0 \tag{C.79}$$

$$\|\boldsymbol{\kappa}^\lambda\|^2 + Y_\lambda^2 - 2(1-\vartheta)\boldsymbol{\kappa}^{j-1}\cdot\boldsymbol{\kappa}^\lambda - w = 2Y_\lambda\|\boldsymbol{\kappa}^\lambda\| - \frac{2(1-\vartheta)Y_\lambda}{\|\boldsymbol{\kappa}^\lambda\|}\boldsymbol{\kappa}^{j-1}\cdot\boldsymbol{\kappa}^\lambda \tag{C.80}$$

$$\left(\|\boldsymbol{\kappa}^\lambda\|^2 + Y_\lambda^2 - 2(1-\vartheta)\boldsymbol{\kappa}^{j-1}\cdot\boldsymbol{\kappa}^\lambda - w\right)^2 = \left(2Y_\lambda\|\boldsymbol{\kappa}^\lambda\| - \frac{2(1-\vartheta)Y_\lambda}{\|\boldsymbol{\kappa}^\lambda\|}\boldsymbol{\kappa}^{j-1}\cdot\boldsymbol{\kappa}^\lambda\right)^2 \tag{C.81}$$

$$\begin{aligned}
&\|\boldsymbol{\kappa}^\lambda\|^4 + Y_\lambda^4 + 4(1-\vartheta)^2(\boldsymbol{\kappa}^{j-1}\cdot\boldsymbol{\kappa}^\lambda)^2 + w^2 \\
&\qquad + 2Y_\lambda^2\|\boldsymbol{\kappa}^\lambda\|^2 - 4(1-\vartheta)\|\boldsymbol{\kappa}^\lambda\|^2(\boldsymbol{\kappa}^{j-1}\cdot\boldsymbol{\kappa}^\lambda) - 2w\|\boldsymbol{\kappa}^\lambda\|^2 \\
&\qquad - 4(1-\vartheta)Y_\lambda^2(\boldsymbol{\kappa}^{j-1}\cdot\boldsymbol{\kappa}^\lambda) - 2wY_\lambda^2 + 4w(1-\vartheta)(\boldsymbol{\kappa}^{j-1}\cdot\boldsymbol{\kappa}^\lambda) \\
&\quad = 4Y_\lambda^2\|\boldsymbol{\kappa}^\lambda\|^2 + \frac{4(1-\vartheta)^2Y_\lambda^2}{\|\boldsymbol{\kappa}^\lambda\|^2}(\boldsymbol{\kappa}^{j-1}\cdot\boldsymbol{\kappa}^\lambda)^2 - 8(1-\vartheta)Y_\lambda^2(\boldsymbol{\kappa}^{j-1}\cdot\boldsymbol{\kappa}^\lambda)
\end{aligned} \tag{C.82}$$

Multiplying by $\|\boldsymbol{\kappa}^\lambda\|^2$

$$\begin{aligned}
&\|\boldsymbol{\kappa}^\lambda\|^6 + Y_\lambda^4\|\boldsymbol{\kappa}^\lambda\|^2 + 4(1-\vartheta)^2\|\boldsymbol{\kappa}^\lambda\|^2(\boldsymbol{\kappa}^{j-1}\cdot\boldsymbol{\kappa}^\lambda)^2 + w^2\|\boldsymbol{\kappa}^\lambda\|^2 \\
&\qquad + 2Y_\lambda^2\|\boldsymbol{\kappa}^\lambda\|^4 - 4(1-\vartheta)\|\boldsymbol{\kappa}^\lambda\|^4(\boldsymbol{\kappa}^{j-1}\cdot\boldsymbol{\kappa}^\lambda) - 2w\|\boldsymbol{\kappa}^\lambda\|^4 \\
&\quad - 4(1-\vartheta)Y_\lambda^2\|\boldsymbol{\kappa}^\lambda\|^2(\boldsymbol{\kappa}^{j-1}\cdot\boldsymbol{\kappa}^\lambda) - 2wY_\lambda^2\|\boldsymbol{\kappa}^\lambda\|^2 + 4w(1-\vartheta)\|\boldsymbol{\kappa}^\lambda\|^2(\boldsymbol{\kappa}^{j-1}\cdot\boldsymbol{\kappa}^\lambda) \\
&\quad = 4Y_\lambda^2\|\boldsymbol{\kappa}^\lambda\|^4 + 4(1-\vartheta)^2Y_\lambda^2(\boldsymbol{\kappa}^{j-1}\cdot\boldsymbol{\kappa}^\lambda)^2 - 8(1-\vartheta)Y_\lambda^2\|\boldsymbol{\kappa}^\lambda\|^2(\boldsymbol{\kappa}^{j-1}\cdot\boldsymbol{\kappa}^\lambda)
\end{aligned} \tag{C.83}$$

Let

$$Z_\lambda := V_\lambda^{-1} = 1 + \vartheta H_{nl}\delta\lambda \tag{C.84}$$

Then, recalling the definition (C.66) of $\boldsymbol{\kappa}^\lambda$

$$Z_\lambda \boldsymbol{\kappa}^\lambda = \bar{\boldsymbol{\kappa}}^\lambda := Z_\lambda \boldsymbol{S}^{\vartheta,\text{trial}} - \boldsymbol{A}^{\text{trial}} = (1 + \vartheta H_{nl}\delta\lambda)\boldsymbol{S}^{\vartheta,\text{trial}} - \boldsymbol{A}^{\text{trial}} \tag{C.85}$$

Analogously, using the previous definition

$$Y_\lambda := \vartheta\delta\lambda \left(\sqrt{6}\mathsf{G} + \sqrt{\tfrac{2}{3}} H_{ki} V_\lambda\right) \tag{C.86}$$

and introducing

$$\begin{aligned} Q_\lambda := Z_\lambda Y_\lambda &= \vartheta\delta\lambda \left(\sqrt{6}\mathsf{G} Z_\lambda + \sqrt{\tfrac{2}{3}} H_{ki}\right) \\ &= \vartheta\delta\lambda \left[\sqrt{6}\mathsf{G}(1 + \vartheta H_{nl}\delta\lambda) + \sqrt{\tfrac{2}{3}} H_{ki}\right] \\ &= \sqrt{6}\vartheta^2 \mathsf{G} H_{nl}\delta\lambda^2 + \vartheta \left(\sqrt{6}\mathsf{G} + \sqrt{\tfrac{2}{3}} H_{ki}\right)\delta\lambda \end{aligned} \tag{C.87}$$

$$\begin{aligned} &\|\boldsymbol{\kappa}^\lambda\|^6 + Y_\lambda^4 \|\boldsymbol{\kappa}^\lambda\|^2 + 4(1-\vartheta)^2 \|\boldsymbol{\kappa}^\lambda\|^2 (\boldsymbol{\kappa}^{j-1} \cdot \boldsymbol{\kappa}^\lambda)^2 + w^2 \|\boldsymbol{\kappa}^\lambda\|^2 \\ &\qquad + 2Y_\lambda^2 \|\boldsymbol{\kappa}^\lambda\|^4 - 4(1-\vartheta)\|\boldsymbol{\kappa}^\lambda\|^4 (\boldsymbol{\kappa}^{j-1} \cdot \boldsymbol{\kappa}^\lambda) - 2w\|\boldsymbol{\kappa}^\lambda\|^4 \\ &\quad - 4(1-\vartheta) Y_\lambda^2 \|\boldsymbol{\kappa}^\lambda\|^2 (\boldsymbol{\kappa}^{j-1} \cdot \boldsymbol{\kappa}^\lambda) - 2w Y_\lambda^2 \|\boldsymbol{\kappa}^\lambda\|^2 + 4w(1-\vartheta)\|\boldsymbol{\kappa}^\lambda\|^2 (\boldsymbol{\kappa}^{j-1} \cdot \boldsymbol{\kappa}^\lambda) \\ &\quad = 4Y_\lambda^2 \|\boldsymbol{\kappa}^\lambda\|^4 + 4(1-\vartheta)^2 Y_\lambda^2 (\boldsymbol{\kappa}^{j-1} \cdot \boldsymbol{\kappa}^\lambda)^2 - 8(1-\vartheta) Y_\lambda^2 \|\boldsymbol{\kappa}^\lambda\|^2 (\boldsymbol{\kappa}^{j-1} \cdot \boldsymbol{\kappa}^\lambda) \end{aligned} \tag{C.88}$$

C.2 The polynomial equation

Let

$$Q_\lambda := Z_\lambda Y_\lambda \qquad \bar{\boldsymbol{\kappa}}^\lambda := Z_\lambda \boldsymbol{\kappa}^\lambda$$

Multiplying now by Z_λ^6 to obtain

$$\begin{aligned} &\|\bar{\boldsymbol{\kappa}}^\lambda\|^6 + Q_\lambda^4 \|\bar{\boldsymbol{\kappa}}^\lambda\|^2 + 4(1-\vartheta)^2 Z_\lambda^2 \|\bar{\boldsymbol{\kappa}}^\lambda\|^2 (\boldsymbol{\kappa}^{j-1} \cdot \bar{\boldsymbol{\kappa}}^\lambda)^2 + w^2 Z_\lambda^4 \|\bar{\boldsymbol{\kappa}}^\lambda\|^2 \\ &\qquad + 2Q_\lambda^2 \|\bar{\boldsymbol{\kappa}}^\lambda\|^4 - 4(1-\vartheta) Z_\lambda \|\bar{\boldsymbol{\kappa}}^\lambda\|^4 (\boldsymbol{\kappa}^{j-1} \cdot \bar{\boldsymbol{\kappa}}^\lambda) - 2w Z_\lambda^2 \|\bar{\boldsymbol{\kappa}}^\lambda\|^4 \\ &\quad - 4(1-\vartheta) Z_\lambda Q_\lambda^2 \|\bar{\boldsymbol{\kappa}}^\lambda\|^2 (\boldsymbol{\kappa}^{j-1} \cdot \bar{\boldsymbol{\kappa}}^\lambda) - 2w Z_\lambda^2 Q_\lambda^2 \|\bar{\boldsymbol{\kappa}}^\lambda\|^2 + 4w(1-\vartheta) Z_\lambda^3 \|\bar{\boldsymbol{\kappa}}^\lambda\|^2 (\boldsymbol{\kappa}^{j-1} \cdot \bar{\boldsymbol{\kappa}}^\lambda) \\ &\quad - 4Q_\lambda^2 \|\bar{\boldsymbol{\kappa}}^\lambda\|^4 - 4(1-\vartheta)^2 Z_\lambda^2 Q_\lambda^2 (\boldsymbol{\kappa}^{j-1} \cdot \bar{\boldsymbol{\kappa}}^\lambda)^2 + 8(1-\vartheta) Z_\lambda Q_\lambda^2 \|\bar{\boldsymbol{\kappa}}^\lambda\|^2 (\boldsymbol{\kappa}^{j-1} \cdot \bar{\boldsymbol{\kappa}}^\lambda) = 0 \end{aligned} \tag{C.89}$$

or, simplifying terms,

$$\begin{aligned}\|\bar{\boldsymbol{\kappa}}^\lambda\|^6 + Q_\lambda^4\|\bar{\boldsymbol{\kappa}}^\lambda\|^2 + 4(1-\vartheta)^2 Z_\lambda^2\|\bar{\boldsymbol{\kappa}}^\lambda\|^2(\boldsymbol{\kappa}^{j-1}\cdot\bar{\boldsymbol{\kappa}}^\lambda)^2 + w^2 Z_\lambda^4\|\bar{\boldsymbol{\kappa}}^\lambda\|^2 \\ - 2Q_\lambda^2\|\bar{\boldsymbol{\kappa}}^\lambda\|^4 - 4(1-\vartheta)Z_\lambda\|\bar{\boldsymbol{\kappa}}^\lambda\|^4(\boldsymbol{\kappa}^{j-1}\cdot\bar{\boldsymbol{\kappa}}^\lambda) - 2wZ_\lambda^2\|\bar{\boldsymbol{\kappa}}^\lambda\|^4 \\ - 2wZ_\lambda^2 Q_\lambda^2\|\bar{\boldsymbol{\kappa}}^\lambda\|^2 + 4w(1-\vartheta)Z_\lambda^3\|\bar{\boldsymbol{\kappa}}^\lambda\|^2(\boldsymbol{\kappa}^{j-1}\cdot\bar{\boldsymbol{\kappa}}^\lambda) \\ - 4(1-\vartheta)^2 Z_\lambda^2 Q_\lambda^2(\boldsymbol{\kappa}^{j-1}\cdot\bar{\boldsymbol{\kappa}}^\lambda)^2 + 4(1-\vartheta)Z_\lambda Q_\lambda^2\|\bar{\boldsymbol{\kappa}}^\lambda\|^2(\boldsymbol{\kappa}^{j-1}\cdot\bar{\boldsymbol{\kappa}}^\lambda) = 0 \quad \text{(C.90)}\end{aligned}$$

which is a 10th-degree polynomial in $\delta\lambda$.

Rearranging to put higher degrees first,

$$\begin{aligned}Q_\lambda^4\|\bar{\boldsymbol{\kappa}}^\lambda\|^2 - 2Q_\lambda^2\|\bar{\boldsymbol{\kappa}}^\lambda\|^4 + 4(1-\vartheta)Z_\lambda Q_\lambda^2\|\bar{\boldsymbol{\kappa}}^\lambda\|^2(\boldsymbol{\kappa}^{j-1}\cdot\bar{\boldsymbol{\kappa}}^\lambda) - 2wZ_\lambda^2 Q_\lambda^2\|\bar{\boldsymbol{\kappa}}^\lambda\|^2 \\ - 4(1-\vartheta)^2 Z_\lambda^2 Q_\lambda^2(\boldsymbol{\kappa}^{j-1}\cdot\bar{\boldsymbol{\kappa}}^\lambda)^2 + \|\bar{\boldsymbol{\kappa}}^\lambda\|^6 \\ + 4(1-\vartheta)^2 Z_\lambda^2\|\bar{\boldsymbol{\kappa}}^\lambda\|^2(\boldsymbol{\kappa}^{j-1}\cdot\bar{\boldsymbol{\kappa}}^\lambda)^2 + w^2 Z_\lambda^4\|\bar{\boldsymbol{\kappa}}^\lambda\|^2 - 4(1-\vartheta)Z_\lambda\|\bar{\boldsymbol{\kappa}}^\lambda\|^4(\boldsymbol{\kappa}^{j-1}\cdot\bar{\boldsymbol{\kappa}}^\lambda) \\ - 2wZ_\lambda^2\|\bar{\boldsymbol{\kappa}}^\lambda\|^4 + 4w(1-\vartheta)Z_\lambda^3\|\bar{\boldsymbol{\kappa}}^\lambda\|^2(\boldsymbol{\kappa}^{j-1}\cdot\bar{\boldsymbol{\kappa}}^\lambda) = 0 \quad \text{(C.91)}\end{aligned}$$

Equivalently, denoting $\eta_\lambda := (1-\vartheta)\left(\boldsymbol{\kappa}^{j-1}\cdot\bar{\boldsymbol{\kappa}}^\lambda\right)$,

$$\begin{aligned}Q_\lambda^4\|\bar{\boldsymbol{\kappa}}^\lambda\|^2 - 2Q_\lambda^2\|\bar{\boldsymbol{\kappa}}^\lambda\|^4 + 4Z_\lambda\eta_\lambda Q_\lambda^2\|\bar{\boldsymbol{\kappa}}^\lambda\|^2 - 2wZ_\lambda^2 Q_\lambda^2\|\bar{\boldsymbol{\kappa}}^\lambda\|^2 - 4Z_\lambda^2\eta_\lambda^2 Q_\lambda^2 \\ + \|\bar{\boldsymbol{\kappa}}^\lambda\|^6 + 4Z_\lambda^2\eta_\lambda^2\|\bar{\boldsymbol{\kappa}}^\lambda\|^2 + w^2 Z_\lambda^4\|\bar{\boldsymbol{\kappa}}^\lambda\|^2 - 4Z_\lambda\eta_\lambda\|\bar{\boldsymbol{\kappa}}^\lambda\|^4 - 2wZ_\lambda^2\|\bar{\boldsymbol{\kappa}}^\lambda\|^4 \\ + 4wZ_\lambda^3\eta_\lambda\|\bar{\boldsymbol{\kappa}}^\lambda\|^2 = 0 \quad \text{(C.92)}\end{aligned}$$

or

$$\begin{aligned}Q_\lambda^4\|\bar{\boldsymbol{\kappa}}^\lambda\|^2 - 2Q_\lambda^2\|\bar{\boldsymbol{\kappa}}^\lambda\|^4 + 2Z_\lambda\left(2\eta_\lambda - wZ_\lambda\right)Q_\lambda^2\|\bar{\boldsymbol{\kappa}}^\lambda\|^2 - 4Z_\lambda^2\eta_\lambda^2 Q_\lambda^2 \\ + \|\bar{\boldsymbol{\kappa}}^\lambda\|^6 + 4Z_\lambda^2\eta_\lambda^2\|\bar{\boldsymbol{\kappa}}^\lambda\|^2 + w^2 Z_\lambda^4\|\bar{\boldsymbol{\kappa}}^\lambda\|^2 - 2Z_\lambda\left(2\eta_\lambda + wZ_\lambda\right)\|\bar{\boldsymbol{\kappa}}^\lambda\|^4 \\ + 4wZ_\lambda^3\eta_\lambda\|\bar{\boldsymbol{\kappa}}^\lambda\|^2 = 0 \quad \text{(C.93)}\end{aligned}$$

For the sake of simplicity it is defined

$$h := \vartheta H_{nl} \tag{C.94}$$

$$g := \sqrt{6}\vartheta G \tag{C.95}$$

$$w := \tfrac{2}{3}\vartheta^2 {\sigma_Y^0}^2 - (1-\vartheta)^2 \|\boldsymbol{\kappa}^{j-1}\|^2 \tag{C.96}$$

$$c_{gh} := \vartheta \left(\sqrt{6} G + \sqrt{\tfrac{2}{3}} H_{ki} \right) \tag{C.97}$$

$$Z_\lambda := V_\lambda^{-1} = h\delta\lambda + 1 \tag{C.98}$$

$$Y_\lambda := \vartheta\delta\lambda \left(\sqrt{6} G + \sqrt{\tfrac{2}{3}} H_{ki} V_\lambda \right) \tag{C.99}$$

$$\begin{aligned} Q_\lambda &:= Z_\lambda Y_\lambda = \vartheta\delta\lambda \left(\sqrt{6} G Z_\lambda + \sqrt{\tfrac{2}{3}} H_{ki} \right) \\ &= \delta\lambda \, (> h\delta\lambda + c_{gh}) \end{aligned} \tag{C.100}$$

$$\boldsymbol{S}^{\vartheta,\mathrm{trial}} := \vartheta \boldsymbol{S}^{\mathrm{trial}} + (1-\vartheta)\boldsymbol{S}^{j-1} \tag{C.101}$$

$$\bar{s}_{SS} := \|\boldsymbol{S}^{\vartheta,\mathrm{trial}}\|^2 \tag{C.102}$$

$$s_{AA} := \|\boldsymbol{A}^{\mathrm{trial}}\|^2 \tag{C.103}$$

$$\bar{s}_{SA} := \boldsymbol{S}^{\vartheta,\mathrm{trial}} \cdot \boldsymbol{A}^{\mathrm{trial}} \tag{C.104}$$

$$\bar{s}_\kappa := \|\boldsymbol{S}^{\vartheta,\mathrm{trial}} - \boldsymbol{A}^{\mathrm{trial}}\|^2 = \bar{s}_{SS} - 2\bar{s}_{SA} + s_{AA} \tag{C.105}$$

$$s_0 := \|\boldsymbol{\kappa}^{j-1}\|^4 = \|\boldsymbol{S}^{j-1} - \boldsymbol{A}^{\mathrm{trial}}\|^4 \tag{C.106}$$

$$t_S := \boldsymbol{\kappa}^{j-1} \cdot \boldsymbol{S}^{\mathrm{trial}} \tag{C.107}$$

$$t_A := \boldsymbol{\kappa}^{j-1} \cdot \boldsymbol{A}^{\mathrm{trial}} \tag{C.108}$$

$$r_S := \boldsymbol{\kappa}^{j-1} \cdot \boldsymbol{S}^{j-1} \tag{C.109}$$

$$c_{\kappa 0} := (1-\vartheta) \left\{ [\vartheta t_S + (1-\vartheta) r_S] - t_A \right\} \tag{C.110}$$

$$c_{\kappa 1} := h(1-\vartheta) \left[\vartheta t_S + (1-\vartheta) r_S \right] \tag{C.111}$$

$$\boldsymbol{\kappa}^\lambda := \boldsymbol{S}^{\vartheta,\mathrm{trial}} - V_\lambda \boldsymbol{A}^{\mathrm{trial}} \tag{C.112}$$

$$\bar{\boldsymbol{\kappa}}^\lambda := Z_\lambda \boldsymbol{\kappa}^\lambda = Z_\lambda \boldsymbol{S}^{\vartheta,\mathrm{trial}} - \boldsymbol{A}^{\mathrm{trial}} \tag{C.113}$$

$$\eta_\lambda := (1-\vartheta) \left(\boldsymbol{\kappa}^{j-1} \cdot \bar{\boldsymbol{\kappa}}^\lambda \right) = c_{\kappa 1}\delta\lambda + c_{\kappa 0} \tag{C.114}$$

Intermediate expressions

Expressions in $\eta_\lambda := (1-\vartheta)\left(\boldsymbol{\kappa}^{j-1}\cdot\bar{\boldsymbol{\kappa}}^{\lambda}\right)$

$$\begin{aligned}
\eta_\lambda &:= (1-\vartheta)\left(\boldsymbol{\kappa}^{j-1}\cdot\bar{\boldsymbol{\kappa}}^{\lambda}\right) && \text{(C.115)}\\
&= (1-\vartheta)\left[\boldsymbol{\kappa}^{j-1}\cdot(Z_\lambda \boldsymbol{S}^{\vartheta,\mathrm{trial}} - \boldsymbol{A}^{\mathrm{trial}})\right]\\
&= (1-\vartheta)\Big\{\boldsymbol{\kappa}^{j-1}\cdot\left\{(h\delta\lambda+1)\left[\vartheta\boldsymbol{S}^{\mathrm{trial}} + (1-\vartheta)\boldsymbol{S}^{j-1}\right] - \boldsymbol{A}^{\mathrm{trial}}\right\}\Big\}\\
&= (1-\vartheta)\{(h\delta\lambda+1)\left[\vartheta t_S + (1-\vartheta)r_S\right] - t_A\}\\
&= (1-\vartheta)\{h\left[\vartheta t_S + (1-\vartheta)r_S\right]\delta\lambda + \left[\vartheta t_S + (1-\vartheta)r_S\right] - t_A\} && \text{(C.116)}
\end{aligned}$$

$$\eta_\lambda = c_{\kappa 1}\delta\lambda + c_{\kappa 0} \qquad \text{(C.117)}$$

Expressions in Z_λ

$$\begin{aligned}
Z_\lambda &= h\delta\lambda + 1 && \text{(C.118)}\\
Z_\lambda^2 &= h^2\delta\lambda^2 + 2h\delta\lambda + 1 && \text{(C.119)}\\
Z_\lambda^3 &= h^3\delta\lambda^3 + 3h^2\delta\lambda^2 + 3h\delta\lambda + 1 && \text{(C.120)}\\
Z_\lambda^4 &= h^4\delta\lambda^4 + 4h^3\delta\lambda^3 + 6h^2\delta\lambda^2 + 4h\delta\lambda + 1 && \text{(C.121)}\\
4wZ_\lambda^3 &= z_{33}\delta\lambda^3 + z_{32}\delta\lambda^2 + z_{31}\delta\lambda + z_{30} && \text{(C.122)}\\
w^2Z_\lambda^4 &= z_{44}\delta\lambda^4 + z_{43}\delta\lambda^3 + z_{42}\delta\lambda^2 + z_{41}\delta\lambda + z_{40} && \text{(C.123)}
\end{aligned}$$

Expressions in $Z_\lambda\eta_\lambda$

$$\begin{aligned}
Z_\lambda^2\eta_\lambda^2 &= \left(h^2\delta\lambda^2 + 2h\delta\lambda + 1\right)\left(c_{\kappa 1}^2\delta\lambda^2 + 2c_{\kappa 1}c_{\kappa 0}\delta\lambda + c_{\kappa 0}^2\right) && \text{(C.124)}\\
&= h^2c_{\kappa 1}^2\delta\lambda^4 + 2h\left(hc_{\kappa 1}c_{\kappa 0} + c_{\kappa 1}^2\right)\delta\lambda^3 && \text{(C.125)}\\
&\quad + \left(h^2c_{\kappa 0}^2 + c_{\kappa 1}^2 + 4hc_{\kappa 1}c_{\kappa 0}\right)\delta\lambda^2 + 2\left(hc_{\kappa 0}^2 + c_{\kappa 1}c_{\kappa 0}\right)\delta\lambda + c_{\kappa 0}^2 && \text{(C.126)}
\end{aligned}$$

$$4Z_\lambda^2\eta_\lambda^2 = p_4\delta\lambda^4 + p_3\delta\lambda^3 + p_2\delta\lambda^2 + p_1\delta\lambda + p_0 \qquad \text{(C.127)}$$

$$\begin{aligned}
p_0 &= 4c_{\kappa 0}^2 && \text{(C.128)}\\
p_1 &= 8\left(hc_{\kappa 0}^2 + c_{\kappa 1}c_{\kappa 0}\right) && \text{(C.129)}\\
p_2 &= 4\left(h^2c_{\kappa 0}^2 + c_{\kappa 1}^2\right) + 16hc_{\kappa 1}c_{\kappa 0} && \text{(C.130)}\\
p_3 &= 8h\left(hc_{\kappa 1}c_{\kappa 0} + c_{\kappa 1}^2\right) && \text{(C.131)}\\
p_4 &= 4h^2c_{\kappa 1}^2 && \text{(C.132)}
\end{aligned}$$

Expressions in Q_λ

$$Q_\lambda => h\delta\lambda^2 + c_{gh}\delta\lambda \tag{C.133}$$

$$Q_\lambda^2 =>^2 h^2\delta\lambda^4 + 2 > hc_{gh}\delta\lambda^3 + c_{gh}^2\delta\lambda^2 \tag{C.134}$$

$$\begin{aligned} Q_\lambda^4 =>^4 & h^4\delta\lambda^8 + 4 >^2 h^2c_{gh}^2\delta\lambda^6 + c_{gh}^4\delta\lambda^4 \\ & + 4 >^3 h^3c_{gh}\delta\lambda^7 + 2 >^2 h^2c_{gh}^2\delta\lambda^6 + 4 > hc_{gh}^3\delta\lambda^5 \end{aligned} \tag{C.135}$$

$$Q_\lambda^4 =>^4 h^4\delta\lambda^8 + 4 >^3 h^3c_{gh}\delta\lambda^7 + 6 >^2 h^2c_{gh}^2\delta\lambda^6 + 4 > hc_{gh}^3\delta\lambda^5 + c_{gh}^4\delta\lambda^4 \tag{C.136}$$

$$Q_\lambda^2 = \delta\lambda^2\left(q_{22}\delta\lambda^2 + q_{21}\delta\lambda + q_{20}\right) \tag{C.137}$$

$$Q_\lambda^4 = \delta\lambda^4\left(q_{44}\delta\lambda^4 + q_{43}\delta\lambda^3 + q_{42}\delta\lambda^2 + q_{41}\delta\lambda + q_{40}\right) \tag{C.138}$$

$$q_{20} = c_{gh}^2 \tag{C.139}$$

$$q_{21} = 2 > hc_{gh} \tag{C.140}$$

$$q_{22} =>^2 h^2 \tag{C.141}$$

$$q_{40} = q_{20}^2 \tag{C.142}$$

$$q_{41} = 2q_{21}q_{20} \tag{C.143}$$

$$q_{42} = q_{21}^2 + 2q_{22}q_{20} = 6q_{22}q_{20} \tag{C.144}$$

$$q_{43} = 2q_{22}q_{21} \tag{C.145}$$

$$q_{44} = q_{22}^2 \tag{C.146}$$

Expressions in $\bar{\boldsymbol{\kappa}}^\lambda$

$$\bar{\boldsymbol{\kappa}}^\lambda := Z_\lambda \boldsymbol{S}^{\vartheta,\mathrm{trial}} - \boldsymbol{A}^{\mathrm{trial}} \tag{C.147}$$

$$\|\bar{\boldsymbol{\kappa}}^\lambda\|^2 = Z_\lambda^2\bar{s}_{SS} - 2Z_\lambda\bar{s}_{SA} + s_{AA} \tag{C.148}$$

$$\|\bar{\boldsymbol{\kappa}}^\lambda\|^2 = (h^2\delta\lambda^2 + 2h\delta\lambda + 1)\bar{s}_{SS} - 2(h\delta\lambda + 1)\bar{s}_{SA} + s_{AA} \tag{C.149}$$

$$\|\bar{\boldsymbol{\kappa}}^\lambda\|^2 = h^2\bar{s}_{SS}\delta\lambda^2 + 2h(\bar{s}_{SS} - \bar{s}_{SA})\delta\lambda + \bar{s}_{SS} - 2\bar{s}_{SA} + s_{AA} \tag{C.150}$$

$$\|\bar{\boldsymbol{\kappa}}^\lambda\|^2 = h^2\bar{s}_{SS}\delta\lambda^2 + 2h(\bar{s}_{SS} - \bar{s}_{SA})\delta\lambda + \bar{s}_\kappa \tag{C.151}$$

$$\|\bar{\boldsymbol{\kappa}}^\lambda\|^2 = k_{22}\delta\lambda^2 + k_{21}\delta\lambda + k_{20} \tag{C.152}$$

$$\|\bar{\boldsymbol{\kappa}}^\lambda\|^4 = k_{44}\delta\lambda^4 + k_{43}\delta\lambda^3 + k_{42}\delta\lambda^2 + k_{41}\delta\lambda + k_{40} \tag{C.153}$$

$$\|\bar{\boldsymbol{\kappa}}^\lambda\|^6 = k_{66}\delta\lambda^6 + k_{65}\delta\lambda^5 + k_{64}\delta\lambda^4 + k_{63}\delta\lambda^3 + k_{62}\delta\lambda^2 + k_{61}\delta\lambda + k_{60} \tag{C.154}$$

$$k_{20} = \bar{s}_{\kappa} \tag{C.155}$$
$$k_{21} = 2h(\bar{s}_{SS} - \bar{s}_{SA}) \tag{C.156}$$
$$k_{22} = h^2 \bar{s}_{SS} \tag{C.157}$$
$$k_{40} = k_{20}^2 \tag{C.158}$$
$$k_{41} = 2k_{21}k_{20} \tag{C.159}$$
$$k_{42} = k_{21}^2 + 2k_{22}k_{20} \tag{C.160}$$
$$k_{43} = 2k_{22}k_{21} \tag{C.161}$$
$$k_{44} = k_{22}^2 \tag{C.162}$$
$$k_{60} = k_{40}k_{20} \tag{C.163}$$
$$k_{61} = k_{41}k_{20} + k_{40}k_{21} \tag{C.164}$$
$$k_{62} = k_{42}k_{20} + k_{41}k_{21} + k_{40}k_{22} \tag{C.165}$$
$$k_{63} = k_{43}k_{20} + k_{42}k_{21} + k_{41}k_{22} \tag{C.166}$$
$$k_{64} = k_{44}k_{20} + k_{43}k_{21} + k_{42}k_{22} \tag{C.167}$$
$$k_{65} = k_{44}k_{21} + k_{43}k_{22} \tag{C.168}$$
$$k_{66} = k_{44}k_{22} \tag{C.169}$$

Expressions in $Q_\lambda^2 \|\bar{\boldsymbol{\kappa}}^\lambda\|^2$

$$Q_\lambda^2 \|\bar{\boldsymbol{\kappa}}^\lambda\|^2 = \delta\lambda^2 \left(q_{22}\delta\lambda^2 + q_{21}\delta\lambda + q_{20}\right)\left(k_{22}\delta\lambda^2 + k_{21}\delta\lambda + k_{20}\right) \tag{C.170}$$

$$\begin{aligned} Q_\lambda^2 \|\bar{\boldsymbol{\kappa}}^\lambda\|^2 = {} & q_{22}k_{22}\delta\lambda^6 && \text{(C.171)}\\ & + \left(q_{22}k_{21} + q_{21}k_{22}\right)\delta\lambda^5 && \text{(C.172)}\\ & + \left(q_{22}k_{20} + q_{21}k_{21} + q_{20}k_{22}\right)\delta\lambda^4 && \text{(C.173)}\\ & + \left(q_{21}k_{20} + q_{20}k_{21}\right)\delta\lambda^3 && \text{(C.174)}\\ & + q_{20}k_{20}\delta\lambda^2 && \text{(C.175)} \end{aligned}$$

$$Q_\lambda^2 \|\bar{\boldsymbol{\kappa}}^\lambda\|^2 = m_6\delta\lambda^6 + m_5\delta\lambda^5 + m_4\delta\lambda^4 + m_3\delta\lambda^3 + m_2\delta\lambda^2 \tag{C.176}$$

$$m_2 := q_{20}k_{20} \tag{C.177}$$
$$m_3 := q_{21}k_{20} + q_{20}k_{21} \tag{C.178}$$
$$m_4 := q_{22}k_{20} + q_{21}k_{21} + q_{20}k_{22} \tag{C.179}$$
$$m_5 := q_{22}k_{21} + q_{21}k_{22} \tag{C.180}$$
$$m_6 := q_{22}k_{22} \tag{C.181}$$

Expanding the polynomial expression

$$\begin{aligned} Q_\lambda^4\|\bar{\boldsymbol{\kappa}}^\lambda\|^2 - 2Q_\lambda^2\|\bar{\boldsymbol{\kappa}}^\lambda\|^4 + 2Z_\lambda\left(2\eta_\lambda - wZ_\lambda\right)Q_\lambda^2\|\bar{\boldsymbol{\kappa}}^\lambda\|^2 - 4Z_\lambda^2\eta_\lambda^2 Q_\lambda^2 \\ + \|\bar{\boldsymbol{\kappa}}^\lambda\|^6 + 4Z_\lambda^2\eta_\lambda^2\|\bar{\boldsymbol{\kappa}}^\lambda\|^2 + w^2Z_\lambda^4\|\bar{\boldsymbol{\kappa}}^\lambda\|^2 - 2Z_\lambda\left(2\eta_\lambda + wZ_\lambda\right)\|\bar{\boldsymbol{\kappa}}^\lambda\|^4 \\ + 4wZ_\lambda^3\eta_\lambda\|\bar{\boldsymbol{\kappa}}^\lambda\|^2 = 0 \end{aligned} \tag{C.182}$$

Term 1

$$Q_\lambda^4\|\bar{\boldsymbol{\kappa}}^\lambda\|^2 = \delta\lambda^4\left(q_{44}\delta\lambda^4 + q_{43}\delta\lambda^3 + q_{42}\delta\lambda^2 + q_{41}\delta\lambda + q_{40}\right)\left(k_{22}\delta\lambda^2 + k_{21}\delta\lambda + k_{20}\right) \tag{C.183}$$

$$\begin{aligned} Q_\lambda^4\|\bar{\boldsymbol{\kappa}}^\lambda\|^2 = {} & q_{44}k_{22}\delta\lambda^{10} \\ & + \left(q_{44}k_{21} + q_{43}k_{22}\right)\delta\lambda^9 \\ & + \left(q_{44}k_{20} + q_{43}k_{21} + q_{42}k_{22}\right)\delta\lambda^8 \\ & + \left(q_{43}k_{20} + q_{42}k_{21} + q_{41}k_{22}\right)\delta\lambda^7 \\ & + \left(q_{42}k_{20} + q_{41}k_{21} + q_{40}k_{22}\right)\delta\lambda^6 \\ & + \left(q_{41}k_{20} + q_{40}k_{21}\right)\delta\lambda^5 \\ & + q_{40}k_{20}\delta\lambda^4 \end{aligned} \tag{C.184}$$

Term 2

$$\begin{aligned} -2Q_\lambda^2\|\bar{\boldsymbol{\kappa}}^\lambda\|^4 = {} & -2\delta\lambda^2\left(q_{22}\delta\lambda^2 + q_{21}\delta\lambda + q_{20}\right) \\ & \left(k_{44}\delta\lambda^4 + k_{43}\delta\lambda^3 + k_{42}\delta\lambda^2 + k_{41}\delta\lambda + k_{40}\right) \end{aligned} \tag{C.185}$$

$$
\begin{aligned}
-2Q_\lambda^2\|\bar{\boldsymbol{\kappa}}^\lambda\|^4 = & -2q_{22}k_{44}\delta\lambda^8 \\
& -\left(2q_{22}k_{43}+2q_{21}k_{44}\right)\delta\lambda^7 \\
& -\left(2q_{22}k_{42}+2q_{21}k_{43}+2q_{20}k_{44}\right)\delta\lambda^6 \\
& -\left(2q_{22}k_{41}+2q_{21}k_{42}+2q_{20}k_{43}\right)\delta\lambda^5 \\
& -\left(2q_{22}k_{40}+2q_{21}k_{41}+2q_{20}k_{42}\right)\delta\lambda^4 \\
& -\left(2q_{21}k_{40}+2q_{20}k_{41}\right)\delta\lambda^3 \\
& -2q_{20}k_{40}\delta\lambda^2 \qquad \text{(C.186)}
\end{aligned}
$$

Term 3

$$
\begin{aligned}
&2Z_\lambda\left(2\eta_\lambda - wZ_\lambda\right)Q_\lambda^2\|\bar{\boldsymbol{\kappa}}^\lambda\|^2 = \\
&\quad\left(m_6\delta\lambda^6+m_5\delta\lambda^5+m_4\delta\lambda^4+m_3\delta\lambda^3+m_2\delta\lambda^2\right)\left(n_2\delta\lambda^2+n_1\delta\lambda+n_0\right) \qquad \text{(C.187)}
\end{aligned}
$$

$$
\begin{aligned}
2Z_\lambda\left(2\eta_\lambda - wZ_\lambda\right) &= 2\left(h\delta\lambda+1\right)\left\{2\left(c_{\kappa 1}\delta\lambda+c_{\kappa 0}\right)-w\left(h\delta\lambda+1\right)\right\} && \text{(C.188)}\\
&= 2\left(h\delta\lambda+1\right)\left\{\left(2c_{\kappa 1}\delta\lambda+2c_{\kappa 0}\right)-\left(hw\delta\lambda+w\right)\right\} && \text{(C.189)}\\
&= 2\left(h\delta\lambda+1\right)\left[\left(2c_{\kappa 1}-hw\right)\delta\lambda+\left(2c_{\kappa 0}-w\right)\right] && \text{(C.190)}\\
&= 2\Big\{h\left(2c_{\kappa 1}-hw\right)\delta\lambda^2 \\
&\quad +\left[h(2c_{\kappa 0}-w)+\left(2c_{\kappa 1}-hw\right)\right]\delta\lambda+\left(2c_{\kappa 0}-w\right)\Big\} && \text{(C.191)}\\
&= n_2\delta\lambda^2+n_1\delta\lambda+n_0 && \text{(C.192)}
\end{aligned}
$$

$$
\begin{aligned}
n_0 &:= 2(2c_{\kappa 0}-w) && \text{(C.193)}\\
n_1 &:= 2\left[h(2c_{\kappa 0}-w)+\left(2c_{\kappa 1}-hw\right)\right] \\
&\quad = 4\left(c_{\kappa 1}+hc_{\kappa 0}-hw\right) && \text{(C.194)}\\
n_2 &:= 2h\left(2c_{\kappa 1}-hw\right) && \text{(C.195)}
\end{aligned}
$$

$$
\begin{aligned}
2Z_\lambda\left(4\eta_\lambda - 2wZ_\lambda\right)Q_\lambda^2\|\bar{\boldsymbol{\kappa}}^\lambda\|^2 &= m_6n_2\delta\lambda^8 && \text{(C.196)}\\
&\quad +\left(m_6n_1+m_5n_2\right)\delta\lambda^7 && \text{(C.197)}\\
&\quad +\left(m_6n_0+m_5n_1+m_4n_2\right)\delta\lambda^6 && \text{(C.198)}\\
&\quad +\left(m_5n_0+m_4n_1+m_3n_2\right)\delta\lambda^5 && \text{(C.199)}\\
&\quad +\left(m_4n_0+m_3n_1+m_2n_2\right)\delta\lambda^4 && \text{(C.200)}\\
&\quad +\left(m_3n_0+m_2n_1\right)\delta\lambda^3 && \text{(C.201)}\\
&\quad +m_2n_0\delta\lambda^2 && \text{(C.202)}
\end{aligned}
$$

Term 4

$$-4Z_\lambda^2\eta_\lambda^2 Q_\lambda^2 = -\delta\lambda^2\left(p_4\delta\lambda^4+p_3\delta\lambda^3+p_2\delta\lambda^2+p_1\delta\lambda+p_0\right)\left(q_{22}\delta\lambda^2+q_{21}\delta\lambda+q_{20}\right) \quad \text{(C.203)}$$

$$\begin{aligned}
-4Z_\lambda^2\eta_\lambda^2 Q_\lambda^2 = &-p_4q_{22}\delta\lambda^8 && \text{(C.204)}\\
&-\left(p_4q_{21}+p_3q_{22}\right)\delta\lambda^7 && \text{(C.205)}\\
&-\left(p_4q_{20}+p_3q_{21}+p_2q_{22}\right)\delta\lambda^6 && \text{(C.206)}\\
&-\left(p_3q_{20}+p_2q_{21}+p_1q_{22}\right)\delta\lambda^5 && \text{(C.207)}\\
&-\left(p_2q_{20}+p_1q_{21}+p_0q_{22}\right)\delta\lambda^4 && \text{(C.208)}\\
&-\left(p_1q_{20}+p_0q_{21}\right)\delta\lambda^3 && \text{(C.209)}\\
&-p_0q_{20}\delta\lambda^2 && \text{(C.210)}\\
& && \text{(C.211)}
\end{aligned}$$

Term 5

$$\|\bar{\boldsymbol{\kappa}}^\lambda\|^6 = k_{66}\delta\lambda^6+k_{65}\delta\lambda^5+k_{64}\delta\lambda^4+k_{63}\delta\lambda^3+k_{62}\delta\lambda^2+k_{61}\delta\lambda+k_{60} \quad \text{(C.212)}$$

Term 6

$$4Z_\lambda^2\eta_\lambda^2\|\bar{\boldsymbol{\kappa}}^\lambda\|^2 = \left(p_4\delta\lambda^4+p_3\delta\lambda^3+p_2\delta\lambda^2+p_1\delta\lambda+p_0\right)\left(k_{22}\delta\lambda^2+k_{21}\delta\lambda+k_{20}\right) \quad \text{(C.213)}$$

$$\begin{aligned}
4Z_\lambda^2\eta_\lambda^2\|\bar{\boldsymbol{\kappa}}^\lambda\|^2 = &\,p_4k_{22}\delta\lambda^6 && \text{(C.214)}\\
&+\left(p_4k_{21}+p_3k_{22}\right)\delta\lambda^5 && \text{(C.215)}\\
&+\left(p_4k_{20}+p_3k_{21}+p_2k_{22}\right)\delta\lambda^4 && \text{(C.216)}\\
&+\left(p_3k_{20}+p_2k_{21}+p_1k_{22}\right)\delta\lambda^3 && \text{(C.217)}\\
&+\left(p_2k_{20}+p_1k_{21}+p_0k_{22}\right)\delta\lambda^2 && \text{(C.218)}\\
&+\left(p_1k_{20}+p_0k_{21}\right)\delta\lambda && \text{(C.219)}\\
&+p_0k_{20} && \text{(C.220)}
\end{aligned}$$

Term 7

$$w^2Z_\lambda^4\|\bar{\boldsymbol{\kappa}}^\lambda\|^2 = \left(z_{44}\delta\lambda^4+z_{43}\delta\lambda^3+z_{42}\delta\lambda^2+z_{41}\delta\lambda+z_{40}\right)\left(k_{22}\delta\lambda^2+k_{21}\delta\lambda+k_{20}\right) \quad \text{(C.221)}$$

$$w^2 Z_\lambda^4 \|\bar{\boldsymbol{\kappa}}^\lambda\|^2 = z_{44}k_{22}\delta\lambda^6 \tag{C.222}$$
$$+ \left(z_{44}k_{21} + z_{43}k_{22}\right)\delta\lambda^5 \tag{C.223}$$
$$+ \left(z_{44}k_{20} + z_{43}k_{21} + z_{42}k_{22}\right)\delta\lambda^4 \tag{C.224}$$
$$+ \left(z_{43}k_{20} + z_{42}k_{21} + z_{41}k_{22}\right)\delta\lambda^3 \tag{C.225}$$
$$+ \left(z_{42}k_{20} + z_{41}k_{21} + z_{40}k_{22}\right)\delta\lambda^2 \tag{C.226}$$
$$+ \left(z_{41}k_{20} + z_{40}k_{21}\right)\delta\lambda \tag{C.227}$$
$$+ z_{40}k_{20} \tag{C.228}$$

Term 8

$$-2Z_\lambda\left(2\eta_\lambda + wZ_\lambda\right)\|\bar{\boldsymbol{\kappa}}^\lambda\|^4 = \left(k_{44}\delta\lambda^4 + k_{43}\delta\lambda^3 + k_{42}\delta\lambda^2 + k_{41}\delta\lambda + k_{40}\right)\left(u_2\delta\lambda^2 + u_1\delta\lambda + u_0\right) \tag{C.229}$$

$$2Z_\lambda\left(2\eta_\lambda + wZ_\lambda\right) = 2\left(h\delta\lambda + 1\right)\left\{2\left(c_{\kappa 1}\delta\lambda + c_{\kappa 0}\right) + w\left(h\delta\lambda + 1\right)\right\} \tag{C.230}$$
$$= 2\left(h\delta\lambda + 1\right)\left\{\left(2c_{\kappa 1}\delta\lambda + 2c_{\kappa 0}\right) + \left(hw\delta\lambda + w\right)\right\} \tag{C.231}$$
$$= 2\left(h\delta\lambda + 1\right)\left[\left(2c_{\kappa 1} + hw\right)\delta\lambda + \left(2c_{\kappa 0} + w\right)\right] \tag{C.232}$$
$$= 2\Big\{h\left(2c_{\kappa 1} + hw\right)\delta\lambda^2 + \left[h(2c_{\kappa 0} + w) + (2c_{\kappa 1} + hw)\right]\delta\lambda + \left(2c_{\kappa 0} + w\right)\Big\} \tag{C.233}$$
$$= u_2\delta\lambda^2 + u_1\delta\lambda + u_0 \tag{C.234}$$

$$-2Z_\lambda\left(2\eta_\lambda + wZ_\lambda\right)\|\bar{\boldsymbol{\kappa}}^\lambda\|^4 = -k_{44}u_2\delta\lambda^6 \tag{C.235}$$
$$- \left(k_{44}u_1 + k_{43}u_2\right)\delta\lambda^5 \tag{C.236}$$
$$- \left(k_{44}u_0 + k_{43}u_1 + k_{42}u_2\right)\delta\lambda^4 \tag{C.237}$$
$$- \left(k_{43}u_0 + k_{42}u_1 + k_{41}u_2\right)\delta\lambda^3 \tag{C.238}$$
$$- \left(k_{42}u_0 + k_{41}u_1 + k_{40}u_2\right)\delta\lambda^2 \tag{C.239}$$
$$- \left(k_{41}u_0 + k_{40}u_1\right)\delta\lambda \tag{C.240}$$
$$- k_{40}u_0 \tag{C.241}$$

Term 9

$$4wZ_\lambda^3\eta_\lambda\|\bar{\boldsymbol{\kappa}}^\lambda\|^2 = \left(t_4\delta\lambda^4 + t_3\delta\lambda^3 + t_2\delta\lambda^2 + t_1\delta\lambda + t_0\right)\left(k_{22}\delta\lambda^2 + k_{21}\delta\lambda + k_{20}\right) \tag{C.242}$$

$$\begin{aligned}
4wZ_\lambda^3\eta_\lambda\|\bar{\boldsymbol{\kappa}}^\lambda\|^2 &= t_4k_{22}\delta\lambda^6 && \text{(C.243)}\\
&\quad + \left(t_4k_{21} + t_3k_{22}\right)\delta\lambda^5 && \text{(C.244)}\\
&\quad + \left(t_4k_{20} + t_3k_{21} + t_2k_{22}\right)\delta\lambda^4 && \text{(C.245)}\\
&\quad + \left(t_3k_{20} + t_2k_{21} + t_1k_{22}\right)\delta\lambda^3 && \text{(C.246)}\\
&\quad + \left(t_2k_{20} + t_1k_{21} + t_0k_{22}\right)\delta\lambda^2 && \text{(C.247)}\\
&\quad + \left(t_1k_{20} + t_0k_{21}\right)\delta\lambda && \text{(C.248)}\\
&\quad + t_0k_{20} && \text{(C.249)}
\end{aligned}$$

$$\begin{aligned}
4wZ_\lambda^3\eta_\lambda &= \left(z_{33}\delta\lambda^3 + z_{32}\delta\lambda^2 + z_{31}\delta\lambda + z_{30}\right)\left(c_{\kappa1}\delta\lambda + c_{\kappa0}\right) && \text{(C.250)}\\
&= t_4\delta\lambda^4 + t_3\delta\lambda^3 + t_2\delta\lambda^2 + t_1\delta\lambda + t_0 && \text{(C.251)}
\end{aligned}$$

$$\begin{aligned}
t_4 &:= z_{33}c_{\kappa1} && \text{(C.252)}\\
t_3 &:= z_{33}c_{\kappa0} + z_{32}c_{\kappa1} && \text{(C.253)}\\
t_2 &:= z_{32}c_{\kappa0} + z_{31}c_{\kappa1} && \text{(C.254)}\\
t_1 &:= z_{31}c_{\kappa0} + z_{30}c_{\kappa1} && \text{(C.255)}\\
t_0 &:= z_{30}c_{\kappa0} && \text{(C.256)}
\end{aligned}$$

C.3 Computing the coefficients

$$h := \vartheta H_{nl} \tag{C.257}$$

$$g := \sqrt{6}\vartheta \mathsf{G} \tag{C.258}$$

$$w := \tfrac{2}{3}\vartheta^2 {\sigma_Y^0}^2 - (1-\vartheta)^2 \|\boldsymbol{\kappa}^{j-1}\|^2 \tag{C.259}$$

$$c_{gh} := \vartheta \left(\sqrt{6}\mathsf{G} + \sqrt{\tfrac{2}{3}} H_{ki} \right) \tag{C.260}$$

$$\boldsymbol{S}^{\vartheta,\text{trial}} := \vartheta \boldsymbol{S}^{\text{trial}} + (1-\vartheta)\boldsymbol{S}^{j-1} \tag{C.261}$$

$$\bar{s}_{SS} := \|\boldsymbol{S}^{\vartheta,\text{trial}}\|^2 \tag{C.262}$$

$$s_{AA} := \|\boldsymbol{A}^{\text{trial}}\|^2 \tag{C.263}$$

$$\bar{s}_{SA} := \boldsymbol{S}^{\vartheta,\text{trial}} \cdot \boldsymbol{A}^{\text{trial}} \tag{C.264}$$

$$\bar{s}_{\kappa} := \|\boldsymbol{S}^{\vartheta,\text{trial}} - \boldsymbol{A}^{\text{trial}}\|^2 = \bar{s}_{SS} - 2\bar{s}_{SA} + s_{AA} \tag{C.265}$$

$$s_0 := \|\boldsymbol{\kappa}^{j-1}\|^4 = \|\boldsymbol{S}^{j-1} - \boldsymbol{A}^{\text{trial}}\|^4 \tag{C.266}$$

$$t_S := \boldsymbol{\kappa}^{j-1} \cdot \boldsymbol{S}^{\text{trial}} \tag{C.267}$$

$$t_A := \boldsymbol{\kappa}^{j-1} \cdot \boldsymbol{A}^{\text{trial}} \tag{C.268}$$

$$r_S := \boldsymbol{\kappa}^{j-1} \cdot \boldsymbol{S}^{j-1} \tag{C.269}$$

$$c_{\kappa 0} := (1-\vartheta)\left\{ [\vartheta t_S + (1-\vartheta) r_S] - t_A \right\} \tag{C.270}$$

$$c_{\kappa 1} := h(1-\vartheta)\left[\vartheta t_S + (1-\vartheta) r_S\right] \tag{C.271}$$

$$q_{20} = c_{gh}^2 \tag{C.272}$$

$$q_{21} = 2 > h c_{gh} \tag{C.273}$$

$$q_{22} =>^2 h^2 \tag{C.274}$$

$$q_{40} = q_{20}^2 \tag{C.275}$$

$$q_{41} = 2 q_{21} q_{20} \tag{C.276}$$

$$q_{42} = q_{21}^2 + 2 q_{22} q_{20} \tag{C.277}$$

$$q_{43} = 2 q_{22} q_{21} \tag{C.278}$$

$$q_{44} = q_{22}^2 \tag{C.279}$$

$$k_{20} = \bar{s}_\kappa \tag{C.280}$$
$$k_{21} = 2h(\bar{s}_{SS} - \bar{s}_{SA}) \tag{C.281}$$
$$k_{22} = h^2 \bar{s}_{SS} \tag{C.282}$$
$$k_{40} = k_{20}^2 \tag{C.283}$$
$$k_{41} = 2k_{21}k_{20} \tag{C.284}$$
$$k_{42} = k_{21}^2 + 2k_{22}k_{20} \tag{C.285}$$
$$k_{43} = 2k_{22}k_{21} \tag{C.286}$$
$$k_{44} = k_{22}^2 \tag{C.287}$$
$$k_{60} = k_{40}k_{20} \tag{C.288}$$
$$k_{61} = k_{41}k_{20} + k_{40}k_{21} \tag{C.289}$$
$$k_{62} = k_{42}k_{20} + k_{41}k_{21} + k_{40}k_{22} \tag{C.290}$$
$$k_{63} = k_{43}k_{20} + k_{42}k_{21} + k_{41}k_{22} \tag{C.291}$$
$$k_{64} = k_{44}k_{20} + k_{43}k_{21} + k_{42}k_{22} \tag{C.292}$$
$$k_{65} = k_{44}k_{21} + k_{43}k_{22} \tag{C.293}$$
$$k_{66} = k_{44}k_{22} \tag{C.294}$$

$$m_2 := q_{20}k_{20} \tag{C.295}$$
$$m_3 := q_{21}k_{20} + q_{20}k_{21} \tag{C.296}$$
$$m_4 := q_{22}k_{20} + q_{21}k_{21} + q_{20}k_{22} \tag{C.297}$$
$$m_5 := q_{22}k_{21} + q_{21}k_{22} \tag{C.298}$$
$$m_6 := q_{22}k_{22} \tag{C.299}$$

$$n_0 := 2(2c_{\kappa 0} - w) \tag{C.300}$$
$$\begin{aligned} n_1 &:= 2\left[h(2c_{\kappa 0} - w) + (2c_{\kappa 1} - hw)\right] \\ &= 4\left(c_{\kappa 1} + hc_{\kappa 0} - hw\right) \end{aligned} \tag{C.301}$$
$$n_2 := 2h\left(2c_{\kappa 1} - hw\right) \tag{C.302}$$

$$u_0 := 2(2c_{\kappa 0} + w) \tag{C.303}$$
$$u_1 := 2\left[h(2c_{\kappa 0} + w) + (2c_{\kappa 1} + hw)\right] \tag{C.304}$$
$$u_2 := 2h\left(2c_{\kappa 1} + hw\right) \tag{C.305}$$

$$p_0 = 4c_{\kappa 0}^2 \tag{C.306}$$
$$p_1 = 8\left(hc_{\kappa 0}^2 + c_{\kappa 1}c_{\kappa 0}\right) \tag{C.307}$$
$$p_2 = 4\left(h^2c_{\kappa 0}^2 + c_{\kappa 1}^2\right) + 16hc_{\kappa 1}c_{\kappa 0} \tag{C.308}$$
$$p_3 = 8h\left(hc_{\kappa 1}c_{\kappa 0} + c_{\kappa 1}^2\right) \tag{C.309}$$
$$p_4 = 4h^2c_{\kappa 1}^2 \tag{C.310}$$

$$z_{40} = w^2 \tag{C.311}$$
$$z_{41} = 4w^2h \tag{C.312}$$
$$z_{42} = 6w^2h^2 \tag{C.313}$$
$$z_{43} = 4w^2h^3 \tag{C.314}$$
$$z_{44} = w^2h^4 \tag{C.315}$$

$$z_{30} := 4w \tag{C.316}$$
$$z_{31} := 12wh \tag{C.317}$$
$$z_{32} := 12wh^2 \tag{C.318}$$
$$z_{33} := 4wh^3 \tag{C.319}$$

$$t_4 := z_{33}c_{\kappa 1} \tag{C.320}$$
$$t_3 := z_{33}c_{\kappa 0} + z_{32}c_{\kappa 1} \tag{C.321}$$
$$t_2 := z_{32}c_{\kappa 0} + z_{31}c_{\kappa 1} \tag{C.322}$$
$$t_1 := z_{31}c_{\kappa 0} + z_{30}c_{\kappa 1} \tag{C.323}$$
$$t_0 := z_{30}c_{\kappa 0} \tag{C.324}$$

The coefficients

$$a_{10} = q_{44}k_{22} \tag{C.325}$$

$$a_9 = q_{44}k_{21} + q_{43}k_{22} \tag{C.326}$$

$$a_8 = (q_{44}k_{20} + q_{43}k_{21} + q_{42}k_{22}) - 2q_{22}k_{44} + m_6n_2 - p_4q_{22} \tag{C.327}$$

$$\begin{aligned} a_7 = {} & (q_{43}k_{20} + q_{42}k_{21} + q_{41}k_{22}) - (2q_{22}k_{43} + 2q_{21}k_{44}) \\ & + (m_6n_1 + m_5n_2) - (p_4q_{21} + p_3q_{22}) \end{aligned} \tag{C.328}$$

$$\begin{aligned} a_6 = {} & (q_{42}k_{20} + q_{41}k_{21} + q_{40}k_{22}) - (2q_{22}k_{42} + 2q_{21}k_{43} + 2q_{20}k_{44}) \\ & + (m_6n_0 + m_5n_1 + m_4n_2) - (p_4q_{20} + p_3q_{21} + p_2q_{22}) + k_{66} \\ & + p_4k_{22} + z_{44}k_{22} - k_{44}u_2 + t_4k_{22} \end{aligned} \tag{C.329}$$

$$\begin{aligned} a_5 = {} & (q_{41}k_{20} + q_{40}k_{21}) - (2q_{22}k_{41} + 2q_{21}k_{42} + 2q_{20}k_{43}) \\ & + (m_5n_0 + m_4n_1 + m_3n_2) - (p_3q_{20} + p_2q_{21} + p_1q_{22}) + k_{65} \\ & + (p_4k_{21} + p_3k_{22}) + (z_{44}k_{21} + z_{43}k_{22}) - (k_{44}u_1 + k_{43}u_2) \\ & + (t_4k_{21} + t_3k_{22}) \end{aligned} \tag{C.330}$$

$$\begin{aligned} a_4 = {} & q_{40}k_{20} - (2q_{22}k_{40} + 2q_{21}k_{41} + 2q_{20}k_{42}) \\ & + (m_4n_0 + m_3n_1 + m_2n_2) - (p_2q_{20} + p_1q_{21} + p_0q_{22}) + k_{64} \\ & + (p_4k_{20} + p_3k_{21} + p_2k_{22}) + (z_{44}k_{20} + z_{43}k_{21} + z_{42}k_{22}) \\ & - (k_{44}u_0 + k_{43}u_1 + k_{42}u_2) + (t_4k_{20} + t_3k_{21} + t_2k_{22}) \end{aligned} \tag{C.331}$$

$$\begin{aligned} a_3 = {} & -(2q_{21}k_{40} + 2q_{20}k_{41}) + (m_3n_0 + m_2n_1) - (p_1q_{20} + p_0q_{21}) + k_{63} \\ & + (p_3k_{20} + p_2k_{21} + p_1k_{22}) + (z_{43}k_{20} + z_{42}k_{21} + z_{41}k_{22}) \\ & - (k_{43}u_0 + k_{42}u_1 + k_{41}u_2) + (t_3k_{20} + t_2k_{21} + t_1k_{22}) \end{aligned} \tag{C.332}$$

$$a_2 = -2q_{20}k_{40} + m_2n_0 - p_0q_{20} + k_{62} + (p_2k_{20} + p_1k_{21} + p_0k_{22})$$
$$+ (z_{42}k_{20} + z_{41}k_{21} + z_{40}k_{22}) - (k_{42}u_0 + k_{41}u_1 + k_{40}u_2)$$
$$+ (t_2k_{20} + t_1k_{21} + t_0k_{22}) \tag{C.333}$$

$$a_1 = k_{61} + (p_1k_{20} + p_0k_{21}) + (z_{41}k_{20} + z_{40}k_{21}) - (k_{41}u_0 + k_{40}u_1)$$
$$+ (t_1k_{20} + t_0k_{21}) \tag{C.334}$$

$$a_0 = k_{60} + p_0k_{20} + z_{40}k_{20} - k_{40}u_0 + t_0k_{20} \tag{C.335}$$